Advances in Optics and Photonics

Recent progress in semiconductor excitable lasers for photonic spike processing

PAUL R. PRUCNAL,[1,2,†] BHAVIN J. SHASTRI,[1,*,†] THOMAS FERREIRA DE LIMA,[1] MITCHELL A. NAHMIAS,[1] AND ALEXANDER N. TAIT[1]

[1]Department of Electrical Engineering, Princeton University, Princeton, New Jersey 08544, USA
[2]e-mail: prucnal@princeton.edu
*Corresponding author: shastri@ieee.org

Received October 28, 2015; revised February 11, 2016; accepted February 12, 2016; published May 20, 2016 (Doc. ID 252097)

Recently, there has been tremendous interest in *excitable* optoelectronic devices and in particular excitable semiconductor lasers that could potentially enable unconventional processing approaches beyond conventional binary-logic-based approaches. In parallel, there has been renewed investigation of non-von Neumann architectures driven in part by incipient limitations in aspects of Moore's law. These *neuromorphic* architectures attempt to decentralize processing by interweaving interconnection with computing while simultaneously incorporating time-resolved dynamics, loosely classified as *spiking* (a.k.a. excitability). The rapid and efficient advances in CMOS-compatible photonic interconnect technologies have led to opportunities in optics and photonics for unconventional circuits and systems. Effort in the budding research field of *photonic spike processing* aims to synergistically integrate the underlying physics of photonics with bio-inspired processing. Lasers operating in the excitable regime are dynamically analogous with the spiking dynamics observed in neuron biophysics but roughly 8 orders of magnitude faster. The field is reaching a critical juncture at which there is a shift from studying single devices to studying an interconnected network of lasers. In this paper, we review the recent research in the information processing abilities of such lasers, dubbed "photonic neurons," "laser neurons," or "optical neurons." An integrated network of such lasers on a chip could potentially grant the capacity for complex, ultrafast categorization and decision making to provide a range of computing and signal processing applications, such as sensing and manipulating the radio frequency spectrum and for hypersonic aircraft control.

OCIS codes: (200.0200) Optics in computing; (200.4700) Optical neural systems; (250.0250) Optoelectronics; (250.5300) Photonic integrated circuits; (250.5960) Semiconductor lasers; (320.7085) Ultrafast information processing
http://dx.doi.org/10.1364/AOP.8.000228

Recent progress in semiconductor excitable lasers for photonic spike processing

PAUL R. PRUCNAL, BHAVIN J. SHASTRI, THOMAS FERREIRA DE LIMA, MITCHELL A. NAHMIAS, AND ALEXANDER N. TAIT

1. INTRODUCTION

Photonics has revolutionized information transmission (communication), while electronics, in parallel, has dominated information transformation (computations). This leads naturally to the following question [1,2]: "How can the unifying of the boundaries between the two be made as effective as possible?" Opportunities in optics for unconventional circuits and systems have inadvertently been created with expeditious advances in CMOS-compatible photonic interconnect technologies. Driven in part by incipient limitations in aspects of Moore's law, there has recently been a renewed investigation [1,3,4–17] of non-von Neumann architectures. In what is considered the third generation of *neuromorphic* architectures, most approaches attempt to decentralize processing—a move that intimately intertwines interconnection with computing—in addition to incorporating time-resolved dynamics, loosely classified as *spiking* [18–20]. Research in photonics has followed suit for neuro-inspired optical information processing [9,21–31] with a recent bloom of proposed forms of spiking dynamics [22,27,29–38]—a move that could potentially help combine computation and communication in the same substrate.

In this paper, we review the recent surge of interest [22,27,29–31,33–48] in the information processing abilities of semiconductor lasers that exploit the dynamical analogy between semiconductor photocarriers and neuron biophysics. Many of these proposals for "photonic neurons," "laser neurons," or "optical neurons" for spike processing are based on lasers operating in an *excitable* regime. Excitability [49–51] is a dynamical system property underlying all-or-none responses. The difference in physical time scales allows these laser systems to exhibit these properties many orders of magnitude faster than their biological counterparts [35]; the temporal resolution (i.e., spike widths) and processing speed (i.e., refractory period) are accelerated by factors nearing 100 million (Fig. 1). Excitable systems possess unique regenerative properties with strong ties to the underlying physics of devices.

Information representation has a profound effect on information processing. Spiking is a sparse coding scheme recently recognized by the neuroscience community as a neural encoding strategy for information processing [20,52,53,54], and it has firm code-theoretic justifications [55–57] (Section 2.3). Digital in amplitude but temporally analog, spike codes exhibit the expressiveness and efficiency of analog processing with the robustness of digital communication. This distributed, asynchronous model processes information using both space and time [56,57]. Spiking approaches promise extreme improvements in computational power efficiency [4] because they directly exploit the underlying physics of biology [3,55,58,59], analog electronics, or, in the present case, optoelectronics.

Spiking primitives have been built in CMOS analog circuits, digital *neurosynaptic cores*, and non-CMOS devices. Various technologies have demonstrated large-scale spiking neural networks (SNNs) in electronics, including, notably: Neurogrid as part

of Stanford University's Brains in Silicon program [10], IBM's TrueNorth as part of DARPA's SyNAPSE program [5], HICANN as part of University of Heidelberg's FACETS/BrainScaleS project [60], and University of Manchester's neuromorphic chip as part of the SpiNNaker project [12]; the latter two are under the flagship of the European Commission's Human Brain Project [61]. These spiking platforms better interact with natural environments by applying the circuit and system principles of neuronal computation, including robust analog signaling, physics-based dynamics, distributed complexity, and learning. They promise potent advantages in efficiency, fault tolerance, and adaptability over von Neumann architectures for tasks involving machine vision and speech processing.

Whereas von Neumann processors rely on point-to-point memory processor communication, a neuromorphic processor typically requires a large number of interconnects (i.e., hundreds of many-to-one fan-in per processor) [4]. This requires a significant amount of multicasting, which creates a communication burden. This, in turn, introduces fundamental performance challenges that result from RC constants and radiative physics in electronic links, in addition to the typical bandwidth-distance-energy limits of point-to-point connections [62]. While some incorporate a dense mesh of wires overlaying the semiconductor substrate as crossbar arrays, large-scale systems are ultimately forced to adopt some form of time-division multiplexing (TDM) or packet switching, notably, address-event representation (AER), which introduces the overhead of representing spikes as digital codes instead of physical pulses. This abstraction at the architectural level allows virtual interconnectivity to exceed wire density by a factor related to the sacrificed bandwidth, which can be orders of magnitude [63]. SNNs based on AER are thus effective at targeting biological time scales and the associated application space: real-time applications (object recognition) in the kilohertz regime [5,12] and accelerated simulation in the low megahertz regime [60]. However, neuromorphic processing for high-bandwidth applications in the gigahertz regime (such as sensing and manipulating the radio spectrum and for hypersonic aircraft control) must take a fundamentally different approach to interconnection.

Mapping a processing paradigm to its underlying dynamics (Fig. 2), rather than abstracting the physics away entirely, can significantly streamline efficiency and performance. Just as optics and photonics are being employed for interconnection in conventional CPU systems, optical networking principles can be applied to the neuromorphic domain. Mapping the model of computation onto a physical substrate for computing can greatly benefit from discovering strong analogies among the underlying physics. Many of the physical processes underlying photonic devices have shown to have a strong analogy with biological processing models, which can both be described within the framework of nonlinear dynamics. Integrated photonic platforms offer an alternative approach to microelectronics. The high switching speeds, high communication bandwidth, and low crosstalk achievable in photonics are very

Figure 1

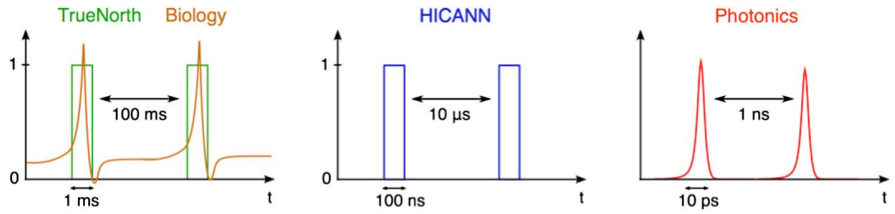

Difference in time scales among biological neurons, current electronic spiking neuron implementations, and photonic neurons.

well suited for an ultrafast spike-based information scheme with high interconnection densities [17,28].

The efforts in this budding research field aim to synergistically integrate the underlying physics of photonics with bio-inspired spike-based processing. This novel processing domain that we call *ultrafast cognitive computing* or *photonic spike processing* represents a broad domain of applications where quick, temporally precise, and robust systems are necessary, including: adaptive control, learning, perception, motion control, sensory processing, autonomous robotics, and cognitive processing of the radio frequency (RF) spectrum.

The paper is organized as follows: In Section 2, we introduce the concept of neural networks (Section 2.1), highlight advantages of spiking neural networks for spike processing (Section 2.2), and discuss properties of dynamical systems possessing spike mechanisms and excitability behavior (Section 2.3). In Section 3, we review recent proposals on excitable semiconductor lasers with neuro-inspired spiking behavior. In Section 4, we survey the general characteristics and challenges of a photonic implementation of a *spiking neuron*. This is followed by a summary and discussion in Section 5. We conclude in Section 6.

2. SPIKE PROCESSING

2.1. Introduction to Neural Networks

Long after psychologists and philosophers deliberated about the source of human thinking and perceiving, Ramón y cajal discovered the cellular nature of the brain: a large network consisting of interconnected neuronal and glial cells—the high-functional part of the *nervous system*. While the biology and biochemistry of brain function are not yet fully understood, it became consensus that neurons play the biggest role in information processing in our brains.

In 1928, Adrian had observed that neural cells emitted electrical pulses [64]. Individual sensory neurons, after undergoing stimuli, produce a series of stereotyped *action potentials*, also referred to as *spikes*. Incoming stimuli either trigger a spike that propagates through the neuron's axon, or not. This is known as the all-or-none law. As a result, the information is represented in the timing of the arrival of these spikes—this

Figure 2

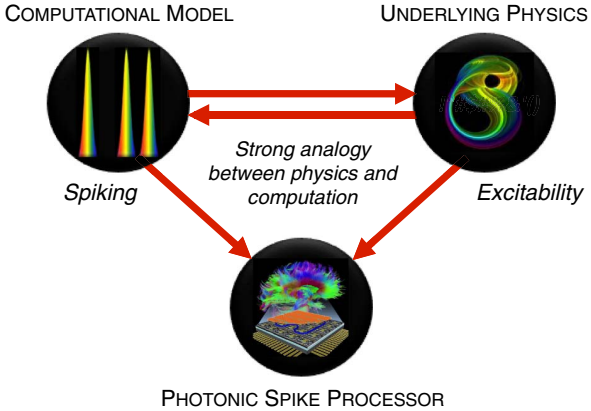

Analogies between spike processing and photonics can be exploited to create a computational paradigm that performs beyond the sum of its parts. By reducing the abstraction between process (spiking) and physics (excitability), there could be a significant advantage in speed, energy usage, scalability.

is known as temporal coding. He also observed that, in response to a static stimulus, the neuron repeatedly "fires" spikes of equal magnitude. In addition, the *spike rate* increases as the stimulus becomes more intense. Thus, the information about the strength of the stimulus is contained in this rate quantity—this is known as rate coding. Rieke present a comprehensive discussion on how to quantify the information conveyed by spike trains [65].

Inspired by these developments, engineers began to attribute some of the complexity, robustness, and efficiency of biological processors to neural network principles, and have endeavored to build artificial systems that exhibit some of these advantages. In 1990, Mead estimated the energy efficiency of a biological neural network about 7 orders of magnitude better than the best physically imaginable digital processor [66]. Modern efficiency comparisons still obtain a very similar result, even after those imagined digital circuits have indeed been built [4]. Today, terminologies such as *neuron*, *synapses*, and *neural network* are shared between these fields. While neuroscientists infer the mechanisms of processes in the brain, the challenge for engineers is to find the minimum ensemble of behaviors necessary to harness similar processing advantages.

Three key elements are present in artificial neural networks: a nonlinear node (neuron), interconnection (network), and information representation (coding scheme). The most elementary illustration of a neuron is shown in Fig. 3. Neurons are networked in a weighted directed graph, in which the connections are called synapses. The input into a particular neuron is a linear combination—also referred to as weighted addition—of the output of other neurons. This particular neuron integrates the weighted signals over time and produces a nonlinear response. This nonlinear response is represented by an *activation function*, and it is usually bounded and monotonic (Fig. 4). The neuron's output is then broadcast to all succeeding nodes in the network. These connections can be "weighted" with negative and positive values, respectively called inhibitory and excitatory synapses. The weight is therefore represented as a real number, and the entire interconnection network expressed as a matrix. The coding scheme is a mapping of how real-valued variables are represented by these spiking signals.

Maass described the evolution of three generations of neural networks studied in computational neuroscience [58]. The first is based on the McCulloch–Pitts neuron model, often referred to as a *perceptron*, which consists of a linear combiner followed by a step-like activation function [67]: the synaptic weighted sum is compared to a threshold and, accordingly, the neuron produces a binary output [Fig. 4(a)]. Artificial

Figure 3

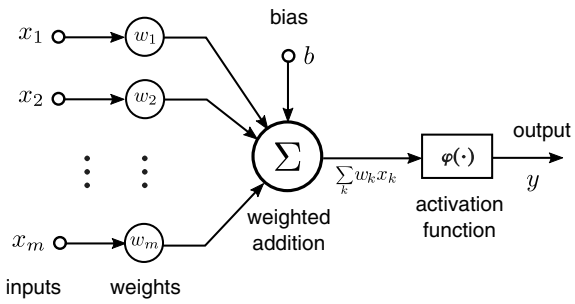

Nonlinear model of a neuron. Note the three parts: (i) a set of *synapses*, or *connecting links*; (ii) an *adder*, or *linear combiner*, performing weighted addition; and (iii) a nonlinear *activation function*.

neural networks based on perceptrons are Boolean-complete—i.e., they have the ability of simulating any Boolean circuit and are said to be universal for digital computations. The second generation of neuron models introduces a continuous monotonic activation function in place of the hard limiter, and therefore it represents inputs and outputs as analog quantities [Fig. 4(b)]. Neural networks from the second generation are universal for analog computations in the sense they can approximate arbitrarily well any continuous function with a compact domain [58].

First and second generation neural networks are powerful constructs present in state-of-the-art machine intelligence [68]. The second generation neural nets, when augmented with the notion of "time" and recurrent connections, can explain certain neural circuits present in the brain; however, they cannot provide explanations for how fast analog computations are performed by neurons in the cortex [58]. For example, neuroscientists demonstrated in the 1990s that a single cortical area in macaque monkey is capable of analyzing and classifying visual patterns in just 30 ms, in spite of the fact that these neurons' firing rates are usually below 100 Hz—i.e., less than three spikes in 30 ms [69], which directly challenges the assumptions of rate coding. In parallel, more evidence was found that biological neurons use the precise timing of these spikes to encode information, which led to the investigation of a third generation of neural networks based on a *spiking neuron*.

2.2. Spiking Neural Networks

Spiking neural models replace the nonlinear activation *function* with a nonlinear *dynamical system*. A formal mathematical formulation of a spiking neuron model is introduced in Ref. [70] (Chap. 1). The most common instance of a spiking neuron is the threshold-fire model. It can be summarized with the following five properties:

Figure 4

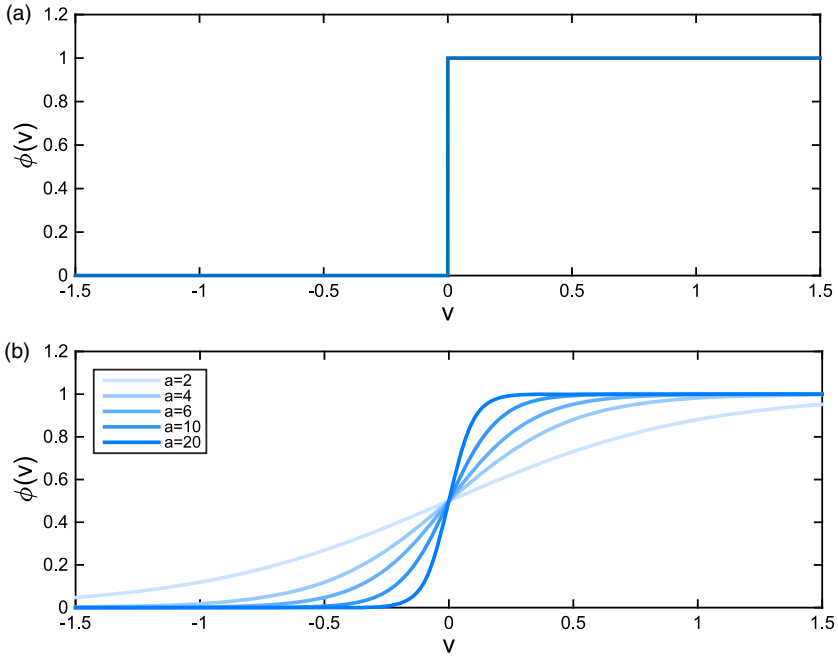

Examples of activation function (Fig. 3). (a) Hard limiter, also known as threshold function or *Heaviside function*: $\varphi(v) = H(v)$. (b) Logistic function (particular example of sigmoid functions) for varying slope parameter a: $\varphi(v) = [1 + \exp(-av)]^{-1}$. Note that the logistic function tends to the Heaviside function as $a \to \infty$.

- **weighted addition**, the ability to sum both positive and negative weighted inputs;
- **integration**, the ability to integrate the weighted sum over time;
- **thresholding**, the ability to make a decision whether or not to send a spike—i.e., the neuron is in a stable equilibrium below a certain *excitability threshold*;
- **reset**, the ability to have a refractory period during which no firing can occur immediately after a spike is released; and
- **pulse generation**, the ability to generate new pulses.

Desirably, though not essentially, the neuron also features **adaptability**, the ability to modify and regulate response properties on slow time scales based on supervised training and/or statistical properties of environmental inputs. Together, Properties 2–5 define the notion of *excitability*, which we will use throughout this paper. The most important example of the "threshold-fire" class of neurons is the leaky-integrate-and-fire neuron (Fig. 5), in which the neuron acts as an integrator with a short memory. In other words, its impulse response is a decaying exponential. Functionally, this allows a processor to correlate spikes that are closely spaced in time.

The information transformed by this neuron is often characterized by the firing rate of these spikes (rate coding) or the timing of individual spikes (temporal coding). Maass demonstrated [58] that this third generation is more than a **generalization of the first two** in terms of functionality and computational power; and for some computational tasks, it can replace large numbers of conventional neurons and still be robust to noise.

Simulating neural networks on a conventional computer is expensive because of the fundamentally serial nature of CPU architectures. Spiking neural networks present a particular challenge because of the need for fine-grained time discretization [71]. Modern machine learning algorithms (i.e., support vector machines) have largely emerged because of this discrepancy. An alternative is building an unconventional, distributed network of spiking nodes, which directly uses physics to carry out the processes of an SNN. We proceed to discuss how the energy dissipation and noise accumulation affect the engineering of physical SNNs.

In the nervous system, firing a spike costs a neuron an amount of energy proportional to how far the spike must travel down the axon, because the transmission medium is dispersive and lossy. There are clear advantages for representing information in spikes

Figure 5

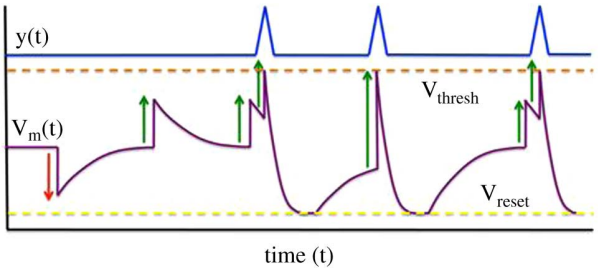

Illustration of spiking dynamics in an LIF neuron. Spikes arriving from inputs $x_j(t)$ that are inhibitory (red arrows) reduce the membrane voltage $V(t)$, while those that are excitatory (green arrows) increase $V(t)$. Enough excitatory activity pushes $V(t)$ above V_{thresh}, releasing a delta function spike in $y_k(t)$, followed by a refractory period during which $V(t)$ recovers to its resting potential V_L. Notations from Fig. 3. Copyright 2013 IEEE. Reprinted, with permission, from Nahmias *et al.*, IEEE J. Sel. Top. Quantum Electron. **19**, 1800212 (2013) [35].

traveling through lossy, dispersive passive media: the bit of information is not destroyed by pulse spreading or amplitude attenuation, since it is contained in the timing of the spike; therefore, it can be regenerated by intermediate neurons. Active mechanisms, such as intermediate neurons, restore the stereotypical shape and amplitude of the spike as it travels through a signaling pathway, mitigating noise accumulation at every stage of the network. Thus, so long as random processes do not interfere irreversibly with spike timings, information can travel indefinitely unaltered at the expense of energy consumed at each intermediate node. This **logic-level restoration** is akin to logic gates, in which each computational element regenerates signals to one of two voltage levels at the expense of drain currents. As a result, spike-timing-based representation schemes theoretically offer robustness to noisy elements.

As a consequence of the boundedness of the neuron's response and of the connection weight, the physical condition for **cascadability** of neurons is that one neuron's output has to be "strong" enough to excite a number of other neurons. This condition ensures that the spike train reaches the end of the network and also guarantees that the information encoded in these spike trains can be processed in parallel by groups of neurons.

In summary, a spike processing system is defined by a combination of nonlinear nodes that obey the all-or-nothing law, excitatory and inhibitory synapses, and a coding system that takes into account noise and inaccuracies in synaptic weights. The relative simplicity of these design specifications allows for the possibility of creating an artificial, physical SNN. However, The three essential elements—the neuron, the synapses, and the coding scheme—work in concert to make up an SNN, and they must therefore be designed together [72,73].

2.3. Excitability Mechanisms

This section is dedicated to explaining what kind of physical system can give rise to the leaky-integration and excitable dynamics discussed in Section 2.2. Hoppensteadt and Izhikevich devoted a book [74] to analyzing dynamical systems that emulate different classes of spiking neural behavior and connected neural networks.

The dynamical lasers that we consider in this paper can be modeled by partial differential equations; they, too, can be analyzed using the framework of a *dynamical system*, as defined in Ref. [75] (Chap. 2). Consider a dynamical system:

$$\frac{\mathrm{d}X}{\mathrm{d}t} = F(X;\Omega), \quad X \in A_X \subset \mathbb{R}^m, \quad \Omega \in A_\Omega \subset \mathbb{R}^l, \tag{1}$$

where $X(t)$ represents the physical quantities, for example, the inputs and outputs, that define the system's state, and Ω summarizes system parameters.

For a given parameter set Ω, the dynamics of a system governed by Eq. (1) can be visualized by analyzing the values of $F(X;\Omega)$ for all $X \in A_X$. These can be geometrically represented on a *phase plane*. If the dynamical system is prepared at an initial condition X_0, it is possible to trace the associated trajectory of the system's state on the phase plane. These trajectories may diverge to the boundary of A_X, or end up in a fixed point of the system, where $\frac{\mathrm{d}X}{\mathrm{d}t} = 0$ [76]. They can also lead back to the original point X_0 after an excursion and start over again repeatedly in a periodic orbit. A *phase portrait* can be constructed with the trajectories represented as lines with arrows, and fixed points with dots. The phase portrait is a useful tool because it reveals the *topological structure* of the dynamical system, indicating the presence and locations of orbits and fixed points, defining its qualitative behavior at different regions. Examples of phase portraits are shown in Figs. 6–8.

The parameter Ω determines the topology of the phase portrait, defining regions in the parameter space ($A_\Omega \subset \mathbb{R}^l$) with similar qualitative behavior of the dynamical system. For example, a classical laser will be quiescent or lasing depending on the applied pump current being below or above a lasing threshold. The boundaries between these qualitatively similar regions is called a bifurcation set ($\Gamma_b \subset A_\Omega$); in the case of the classical laser, the lasing threshold represents a bifurcation point in the pump current parameter.

Fixed points X^*, or resting states, are solutions of the equation $F(X, \Omega) = 0$, or $X^* \in \ker F(\cdot; \Omega)$, and therefore move as Ω is changed. Equation (1) can be linearized around a fixed point X^* via the *Jacobian matrix*:

$$J(X^*, \Omega) = \mathrm{D}_X F = \left(\frac{\partial F_i(X^*; \Omega)}{\partial X_j} \right)_{i,j=1,\ldots,m}. \tag{2}$$

If all eigenvalues of $(J(X^*, \Omega))$ have a negative real part, X^* is said to be a stable, or attractor, node. If all eigenvalues have a positive real part, then X^* is called an unstable, or repeller, node. If one eigenvalue has a positive real part and another a negative real part, X^* is said to be a saddle.

Some dynamical systems present *saddle-node bifurcation* points $(X_{\mathrm{SN}}, \Omega_{\mathrm{SN}})$, wherein upon continuous variation of Ω, a node meets a saddle and they annihilate each other (Fig. 6). In Ref. [74] (Sec. 2.5), Hoppensteadt and Izhikevich lay the mathematical conditions that F must satisfy so the dynamical system is at a saddle-node bifurcation point.

Some dynamical systems have periodic solutions $(X(t) = X(t + T)$, for a given $T > 0)$. This periodic orbit is called a *limit cycle* if the system is attracted back to

Figure 6

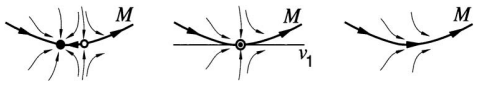

Phase portraits near a saddle-node bifurcation. The solid dot represents an attractor node, and the open dot, the saddle. A multidimensional dynamical system can be reduced by the center manifold procedure (Theorem 2.2 in Ref. [74]). There is a center manifold M tangent to the center subspace spanned by the eigenvector of the Jacobian matrix v_1 near a saddle-node bifurcation. After the reduction procedure, one can represent the dynamical system as a single variable equation $\dot{x} = f(x, \Omega)$, where f is the restriction of F to the manifold M. Reproduced from *Weakly Connected Neural Networks* (1997) by Hoppensteadt and Izhikevich [74] with permission of Springer.

Figure 7

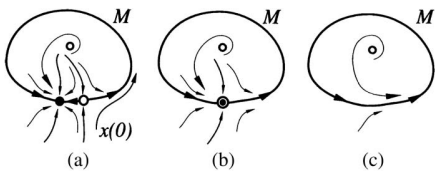

Saddle-node bifurcation on a limit cycle. In some cases, the manifold M (Fig. 6) forms a closed loop. A local bifurcation therefore has global impact on the system dynamics and is hence called a global bifurcation. Reproduced from *Weakly Connected Neural Networks* (1997) by Hoppensteadt and Izhikevich [74] with permission of Springer.

it upon small perturbation. We are interested in systems where these periodic excursions are fast and represent *action potentials*, or *spikes*. In these dynamical systems, a saddle-node bifurcation can occur on a *limit cycle*; they are referred to as *saddle-node on limit cycle* (SNLC) (Fig. 7). When this happens, such a local bifurcation has effect on the global behavior of the system: if the system is at the right side of a saddle point, the system travels along the path of the limit cycle and returns to the attractor node. The qualitative behavior of the system thus changes from *periodic* to *excitable* [74].

There are two phenomena intimately related to each other in a nontrivial way due to the type of bifurcation of state equilibria: neural excitability and transition from rest to periodic spiking activity. The first refers to the ability of using a small perturbation

Figure 8

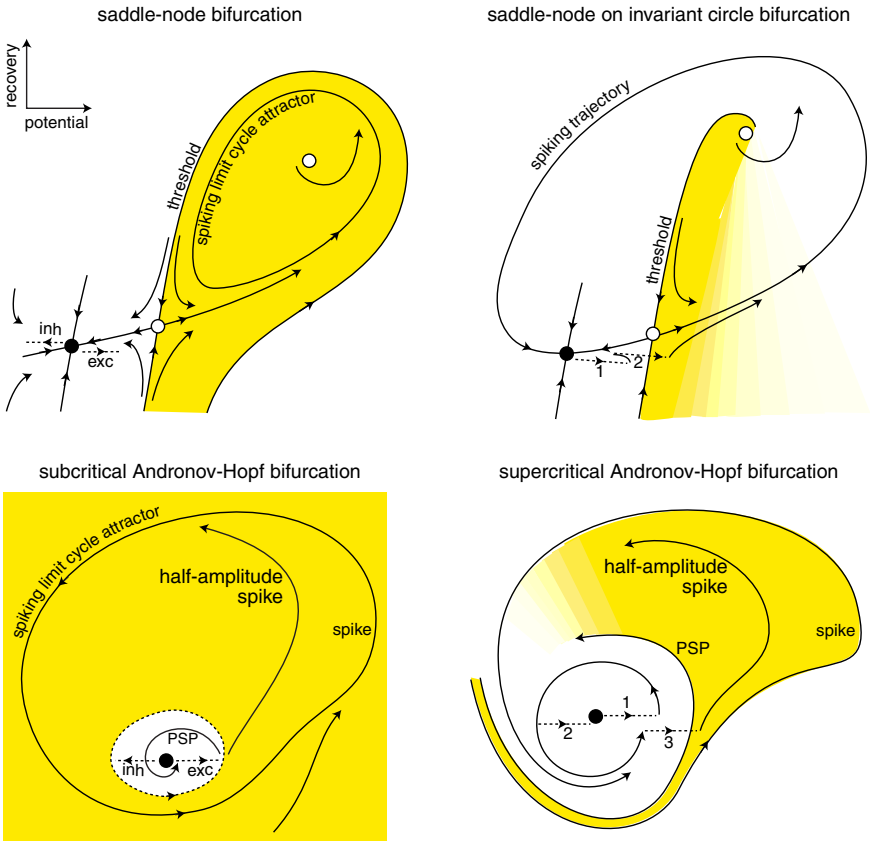

Phase portraits of dynamical systems near four different bifurcations that can exhibit transition between resting and spiking states. The portraits on the left-hand side are bistable: they show a coexistence of resting (attractor node) and spiking steady states (limit cycle), whereas the ones on the right-hand side are monostable. In this paper, we favor analyzing monostable cases because they release a unique spike as a result of a short perturbation of the system. The phase portrait on the top right showcases Class 1 excitable behavior, whereas the others showcase Class 2 excitable behavior. The distinction is explained in the text. One note about temporal integration: a neuron depicted on the top right is called an integrator neuron, because two excitatory pulses (represented as arrows 1 and 2) collaborate to overcome the threshold. However, the neuron shown on the bottom right is called a resonator neuron, because subsequent excitatory stimuli collaborate only if they are presented at specific periods of time. Reprinted with permission from Izhikevich, *Dynamical Systems in Neuroscience: The Geometry of Excitability and Bursting* (2006) [77], published by The MIT Press.

to excite a neuron, triggering a spike, and the second refers to increasing the static stimulus, causing the neuron to periodically fire spikes in succession (see observation by Adrian, Section 2.1). Biological neurons exhibit a wide range of spiking behaviors, the simplest of which can be divided into two classes, as first observed by Hodgkin [78]—refer to Ref. [71] for an extensive discussion of spiking dynamics. Izhikevich [75] showed that Hodgkin's behavioral classification is a reflection of only a few distinct mechanisms that can give rise to spiking. This classification is summarized in Fig. 8.

Classification of excitability mechanisms [75] (Fig. 8)

- Class 1 neural excitability can be observed in the vicinity of a *saddle-node on limit cycle* (SNLC) bifurcation (Fig. 8, top right). A variation in the stimulus causes the saddle to meet the attractor node, which annihilate each other, leaving a stable limit cycle of infinite period as result. As the stimulus pushes the system farther from the bifurcation point, the period of the emerging periodic spiking decreases; however, the amplitude of emerging spikes remains approximately constant.
- Class 2 neural excitability can be observed in the vicinity of a Poincaré–Andronov–Hopf [78] (Hopf, for short) or an *off-limit cycle saddle-node bifurcation* (Fig. 8). When the bifurcation occurs, a stable limit cycle with a finite period becomes the only stable state, causing the system to jump from rest to periodic spiking. As the stimulus gets closer to the bifurcation point, the frequency of the emerging periodic spiking remains nonzero; however, the amplitudes of emerging spikes become arbitrarily small.

We note that this classification above is not perfect. First, Class 1 behavior could also be observed on so-called *homoclinic bifurcation*, when a limit cycle collides with a saddle point, close to the phase portrait shown in Fig. 8, top left. However, we point out that the bistability and hysteresis present in this case complicate the definition of excitability (cf. [77] Sec. 7.1). Second, we described only *codimension one* bifurcations, i.e., those that occur by changing only one of the parameters of the system [Ω_i in Eq. (1)], because those are much more common to be constructed experimentally or observed in nature [75,79,80]. Third, we looked only at dynamical systems that can be reduced to the two-dimensional plane, where the phase portraits are much more well behaved than for 3D or higher dimensions.

In Class 1 excitable systems near a SNLC bifurcation, the limit cycle solution (Fig. 7) can be mapped into a one-dimensional invariant circle (Fig. 9). In one side of the bifurcation, the model has no stationary solution, which corresponds to a periodic

Figure 9

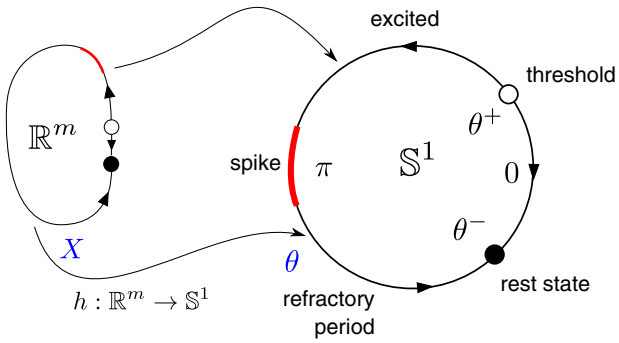

Ermentrout–Kopell theorem (Theorem 8.3 in Ref. [74]): The transformation h maps the limit cycle, solution of Eq. (1), into an ordinary differential equation (ODE) in an invariant circle. The invariant circle on the right represents each stage of the Class 1 neural excitability mechanism. Adapted from [75].

spiking regime. In the other side of the bifurcation, this model has two equilibria: a threshold and a rest state (corresponding to a saddle and a node in the phase portrait). When the system is next to the saddle-node bifurcation, the threshold and rest state are arbitrarily close; it becomes excitable to small perturbations. A subthreshold perturbation will cause the system to exponentially decay to the rest state, whereas a superthreshold will cause the system to follow a much larger trajectory, producing a spike in the process.

Let us consider a two-section laser with gain and saturable absorption sections, which can be created, for example, by pumping one section above the transparency threshold while the other is pumped below this threshold [50,81–84]. Increasing the current bias in the gain section brings the laser from an excitable regime to a passive Q-switching regime (Section 3.1). Elevated optical injection in microdisk lasers induces similar behavior (Section 3.2b).

Class 1 excitable systems are ideal for modeling an integrate-and-fire neuron, which is the most common ingredient in spiking neural networks. However, Class 2 excitable systems have also been scrutinized analytically and numerically by numerous researchers ([74] for a review). These neurons exhibit an important exotic behavior, known to neuroscientists as typical of resonate-and-fire: they respond to perturbations that are weak but resonant with the natural frequency of the subthreshold damped oscillations around the attractor node [85]. In other words, resonate-and-fire neurons' response can be sensitive to interspike interval (see Fig. 8, bottom right). We discuss one example of a Class 2 spiking laser in Section 3.2a. Class 2 neurons open other possibilities for defining spiking neural networks. In fact, there has been evidence of both kinds of neurons in the human brain.

3. RECENT SEMICONDUCTOR PHOTONIC DEVICES AS EXCITABLE PROCESSORS

Over the past decade there has been a bloom of optoelectronic devices whose dynamical properties exhibit key similarities with models of neuron biophysics, in particular, excitability. In Section 2.3, excitability was behaviorally defined by three main criteria: (i) an unperturbed system rests at a single stable equilibrium; (ii) an external perturbation above the excitability threshold triggers a large excursion from this equilibrium; (iii) the system then settles back to the attractor in what is called the refractory period, after which the system can be excited again [50]. These dynamical regimes involve variables with different time scales that manifest into important attributes of spike processing. The *fast* dynamics governs the width of the output pulse (spike); i.e., the fast variable is responsible for the firing of a pulse. This places a lower bound on the temporal resolution of information coding. The *slow* dynamics governs the output pulse firing rate; i.e., the slow variable determines the full recovery of the system to the quiescent state. This places an upper bound on how fast information can be processed.

Optical excitability in semiconductor devices is widely studied theoretically and experimentally. These include: two-section gain and saturable absorber (SA) lasers [31,35,37,47,81–84,86–90], semiconductor ring [33,43,91–93] and microdisk lasers [36,94], two-dimensional photonic crystal nanocavities [34,39,95], resonant tunneling diode photodetectors and laser diodes [45,46,96], semiconductor lasers based on optical injection [22,29,40,97–104], semiconductor lasers subjected to optical feedback [27,48,105–109], and polarization switching in VCSELs [38,41,44]. Generally speaking, all these lasers fall into one of the three categories—coherent optical injection electrical injection, noncoherent optical injection, and full electrical injection—as shown in Fig. 10 and can be pumped either optically or electrically. The rich body of work in this field has demonstrated that the complex dynamics of excitable lasers

could form a fundamental building block for spike information processing. Excitable lasers, for example, can simultaneously exhibit logic-level restoration, cascadability, and input–output isolation, which are key impediments to optical computing [1,7,8]. In addition to single-laser excitability, there have a been few demonstrations of key spike processing circuits including temporal pattern recognition [31] and stable recurrent memory [31,96,104]. The simple demonstration of temporal logic suggests that spiking neural networks of such excitable lasers are capable of categorization and decision making. Combined with learning algorithms such as spike timing-dependent plasticity (STDP) [110,111], networks could potentially perform more complex tasks such as spike-pattern cluster analysis [59]. The demonstration of bistable recurrent spiking circuits shows that processing networks of excitable lasers are capable of indefinite cascadability and information retention, a prerequisite for more complex types of temporal attractors in recurrent networks. In networks of more lasers, spiking attractors could be more numerous, complex, and even competitive in order to achieve different information processing goals.

Next, we review recent exciting developments on candidate excitable semiconductors lasers and devices proposed in literature for a photonic spike processor.

3.1. Two-Section Gain and SA Excitable Lasers

Prucnal and co-workers [28,31,35,47] and Barbay and co-workers [37,84,89] have recently advocated two-section gain and SA excitable lasers as a computational primitive for spike processing. This system has been shown, theoretically [35,90] and experimentally [31,37], to be analogous to the leaky integrate-and-fire (LIF) neuron model [71], which is commonly employed in computational neuroscience for modeling biological neural networks. There is a key difference, however—both dynamical systems operate on vastly different time scales. Whereas biological neurons have time constants of the order of milliseconds, carrier lifetimes of laser gain sections are typically in the nanosecond range and can go down to picoseconds. Although it is one of the simpler spike-based models, the LIF model is capable of universal computations [58] and the transmission of information through spike timings [112]. This two-section excitable laser has also been investigated in the context of a generalized optoelectronic networking model [28], which is further discussed in Section 4.

Figure 10

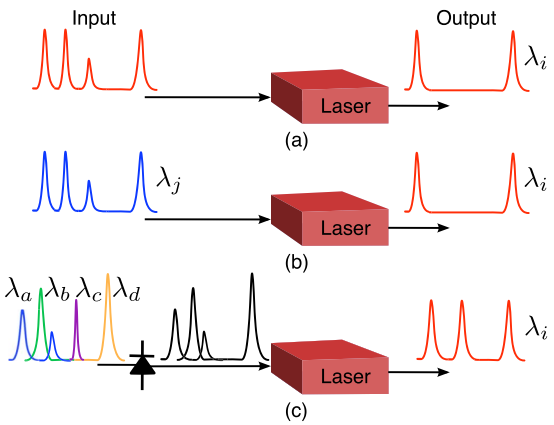

General classification of semiconductor excitable lasers based on: (a) coherent optical injection electrical injection, (b) noncoherent optical injection, and (c) full electrical injection. Note each of these lasers can be pumped either electrically or optically.

Principle of operation: The two-section excitable laser is composed of a gain section with a SA, and mirrors for cavity feedback [Fig. 11(a)]. The Yamada model [113] describes the behavior of lasers with independent gain and SA sections with an approximately constant intensity profile across the cavity. The inputs selectively perturb the gain. The gain medium acts as a temporal integrator with a time constant that is equal to the carrier recombination lifetime. A SA becomes transparent with increasing light intensity and thus acts as a threshold detector by gating the intensity built up in the cavity by the gain medium [Fig. 11(b)]. This 3D dynamical system, in its simplest form, can be described with the following nondimensionalized equations [35,84]:

$$\frac{\mathrm{d}G(t)}{\mathrm{d}t} = \gamma_G[A - G(t) - G(t)I(t)] + \theta(t), \tag{3a}$$

$$\frac{\mathrm{d}Q(t)}{\mathrm{d}t} = \gamma_Q[B - Q(t) - aQ(t)I(t)], \tag{3b}$$

$$\frac{\mathrm{d}I(t)}{\mathrm{d}t} = \gamma_I[G(t) - Q(t) - 1]I(t) + \varepsilon f(G), \tag{3c}$$

where $G(t)$ models the gain, $Q(t)$ is the absorption, $I(t)$ is the laser intensity, A is the bias current of the gain, B is the level of absorption, a describes the differential absorption relative to the differential gain, γ_G is the relaxation rate of the gain, γ_Q is the relaxation rate of the absorber, γ_I is the inverse photon lifetime, $\theta(t)$ is the time-dependent input perturbations, and $\varepsilon f(G)$ is the spontaneous noise contribution to intensity; ε is small.

The SA can be designed to have a very short relaxation time of the order of the cavity intensity, which can be implemented either through doping or quantum well (QW)

Figure 11

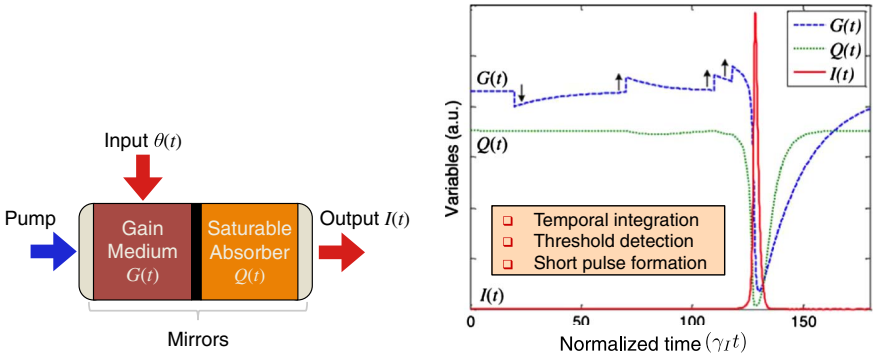

(a) Simple schematic of a two-section gain-SA excitable laser. The device is composed of (i) a gain section, (ii) a saturable absorber, and (iii) mirrors for cavity feedback. In the LIF excitable model, inputs selectively perturb the gain optically or electrically. (b) Simulation results of an SA laser [using Eqs. (3a)–(3c)] behaving as an LIF neuron. Arrows indicate inputs $\theta(t)$ (excitatory pulses and inhibitory pulses) that change the gain by some amount ΔG. Enough excitatory input causes the system to enter fast dynamics in which a spike is generated, followed by the fast recovery of the absorption $Q(t)$ and the slow recovery of the gain $G(t)$. Variables were rescaled to fit within the desired range. Values used: $A = 4.3$; $B = 3.52$; $a = 1.8$; $\gamma_G = 0.05$; γ_L, $\gamma_I \gg 0.05$. Copyright 2013 IEEE. Reprinted, with permission, from Nahmias *et al.*, IEEE J. Sel. Top. Quantum Electron. **19**, 1800212 (2013) [35].

design. In this system, the gain is considered to be much slower than both the intensity and absorption. With a high enough input signal, the laser behaves as an excitable system and reaches a firing threshold. This boundary is caused by an unstable manifold that originates from a saddle point, created when the system is close to a homoclinic bifurcation [82]. This is characteristic of Class 1 excitability (as delineated in Section 2.3), a key correlate of a spike processor, and one of the most critical properties of a spiking neuron. Dubbeldam and Krauskopf [82] provide a comprehensive bifurcation analysis describing all possible dynamics of the model. Furthermore, the gain-absorber system has been shown [31,47] to exhibit cascadability, logic-level restoration, and input–output isolation [1]. The internal dynamics can be compressed to obtain an instantaneous pulse-generation model [35]:

$$\frac{\mathrm{d}G(t)}{\mathrm{d}t} = -\gamma_G(G(t) - A) + \theta(t); \tag{4a}$$

$$\text{if } G(t) > G_{\text{thresh}} \text{ then}$$
$$\text{release a pulse, and set } \mathrm{G}(t) \rightarrow G_{\text{reset}}, \tag{4b}$$

where $\theta(t)$ is the input term, which can include spike inputs of the form $\theta(t) = \sum_i \delta(t - \tau_i)$ for spike firing times τ_i, G_{thresh} is the gain threshold, and $G_{\text{reset}} \sim 0$ is the gain at transparency. The conditional statements account for the fast dynamics of the system that occur on time scales of order $1/\gamma_I$, and assure that G_{thresh}, G_{reset}, and the pulse amplitude remain constant.

Results: The two-section excitable laser model with gain and an embedded SA is applicable to different physical manifestations. Nahmias *et al.* [35] proposed a compact VCSEL-SA exhibiting neuron-like behavior and more recently a two-section distributed feedback (DFB) excitable laser neuron in a hybrid III–V/silicon platform [47]. The structure of this laser is very similar to [114] where the semiconductor gain and absorber sections are isolated electrically with a proton implantation region [115], and a separate implant provides a smaller lifetime in the absorber section.

Shastri *et al.* theoretically [88] and experimentally [31] demonstrated a fiber-based graphene excitable laser and also proposed an integrated device that contains electrically pumped QWs (gain section), two sheets of graphene (SA section), and a DFB-grating (section). Since its emergence as a new type of SA, graphene has been rigorously studied in the context of passive mode locking and Q-switching [116–119] and has been preferred over the widely used semiconductor SAs [120] due to its high saturable-absorption-to-volume ratio [121]. Graphene possesses a number of other important advantages that are particularly useful in the context of processing, including a very fast response time, wideband frequency tunability (useful for WDM networks), and a tunable modulation depth. Furthermore, graphene also has a high thermal conductivity and damage threshold compared to semiconductor absorbers.

Figure 12 shows the integrated excitable laser in a hybrid InGaAsP–graphene–silicon platform. It comprises a III–V epitaxial structure with multiple quantum well (MQW) region bonded to a low-loss silicon rib waveguide that rests on a silicon-on-insulator (SOI) substrate. Sandwiched in between is a heterostructure of two monolayer graphene sheets and an hexagonal boron nitride (hBN) spacer. The cavity and waveguide are formed by the presence of a half-wavelength grating in the silicon. Silicon gratings provide feedback for the lasing cavity. The full cavity structure includes III–V layers bonded to silicon, and a quarter-shifted wavelength grating (quarter shift not shown). The silicon waveguide has height, width, and rib etch of 1.5 μm, 500 nm, and 300 nm, respectively. The length of the cavity is 120 μm. The laser emits light along the

waveguide structure into a passive silicon network. The hybrid III–V platform is highly scalable and amenable to both passive and active photonic integration [123].

Shastri *et al.* [31] compare the simulated (predicted) performance of the integrated device with those obtained experimentally with an analogous fiber-based prototype. The former is capable of exhibiting the same behaviors, but on a much faster time scale and with lower pulse energies. Some key behaviors associated with excitability are shown in Fig. 13. Figure 13(a) shows the output pulse width as a function of an input pulse for both the integrated and fiber lasers. Although the pulse profile stays the same, its amplitude may change depending on the value of the perturbation. The integrated device exhibits the same behavior on a much faster time scale, recovering in nanoseconds with pulse widths in picoseconds, a factor of about $\sim 10^3$ and $\sim 10^6$, respectively, than the fiber prototype. The width of the pulses—which puts a lower bound on the temporal resolution of the information encoded between spikes—is bounded by both the SA recovery time and the round-trip cavity time. Although graphene's incredibly fast response time (~2 ps) makes it effectively instantaneous in the fiber lasers, simulations suggest that graphene can shorten the pulse widths in an integrated device. The relative refractory period, on the other hand, is bounded by the speed of either the gain or the SA, although the gain recovery times tend to be larger.

Temporal pulse correlation is an important processing function that emerges from excitability. An integrating excitable system is able to sum together multiple inputs if they are close enough to one another in time. This allows for the detection of pulse clusters, or potentially, coincidence detection of pulses across channels through the use of incoherent optical summing [28]. Coincidence detection underlies a number of processing tasks, including associative memory [125] and STDP [110,111], a form of

Figure 12

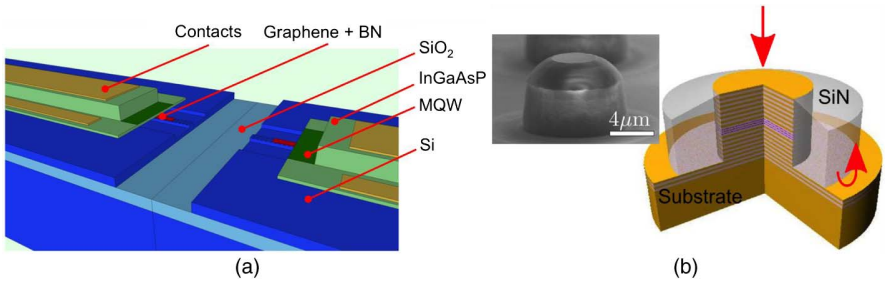

(a) Cutaway architecture (showing a terraced view of the center) of the hybrid InGaAsP–silicon evanescent laser neuron design with graphene layers sandwiched between the Si and III–V layers. This platform includes III–V materials that are bonded to underlying passive silicon photonic interconnection networks. In a typical device, optical modes are hybridized between the silicon and III–V layers simultaneously [122]. Nanostructures necessary for waveguides, resonators, and gratings are fabricated strictly in silicon, while the III–V layers provide optical gain [123,124]. The use of a DFB cavity guarantees a single longitudinal lasing mode, defined through the lithographic definition of lasing wavelength via SOI grating pitch. Reproduced from Shastri *et al.*, Sci. Rep. **6**, 19126 (2016) [31]. Licensed under CC BY. (b) Sketch and scanning electron microscope image of the micropillar laser with SA (see text). A vertical micropillar laser in a III–V material stack is surrounded by a SiN oxide. Pump light (red arrow) is incoming from the top and is partially reflected from the remaining part of the lower Bragg mirror. Reprinted with permission from Selmi *et al.*, Phys. Rev. Lett. **112**, 183902 (2014) [37]. Copyright 2014 by the American Physical Society. Figure 1 from http://link.aps.org/abstract/PRL/v112/p183902.

temporal learning. Temporal pulse correlation in the fiber laser experiment and simulation and in the integrated laser simulation are shown in Fig. 13(b). Reducing the time interval between input pulses (i.e., simultaneous arrival) results in an output pulse. Although the fiber laser can function at kilohertz speeds, the internal dynamics of the integrated device allows it to function much faster, putting it in the gigahertz regime.

Figures 14(a)–14(c) illustrate the typical transient excitable dynamics of a gain-SA laser. In this system, an excitatory pulse increases the carrier concentration within the gain region by an amount proportional to its energy (integrated power) through gain enhancement. Beyond some threshold excitation energy, the absorber is saturated, resulting in the release of a pulse. This is followed by a relative refractory period during which the arrival of a second excitatory pulse is unable to cause the laser to fire as the gain recovers. The system is also capable of emitting spike doublets or triplets [Fig. 14(d)] in which the interspike timing encodes information about the pulse width and amplitude, a useful encoding scheme for selective activation [126]. Since pulse generation results from internal dynamics in excitable systems, such systems exhibit important restorative properties. Different input perturbations often result in the same output, an important criteria for cascadability. Figures 14(e) and 14(f) illustrate the response of the device as a result of a variety of input pulses. The excitable system responds in a stereotyped and repeatable way; all emitted pulses having identical pulse profiles. Outputs trigger asynchronously from input pulses, preserving analog timing information.

Figure 13

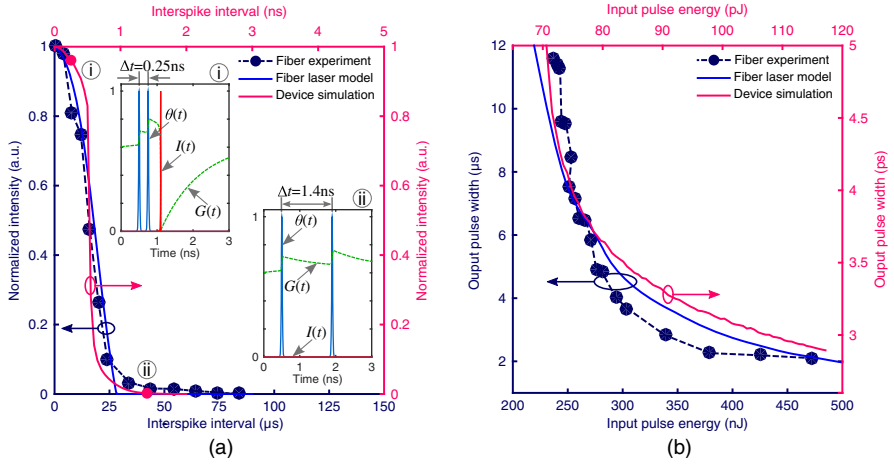

Second-order properties of excitability. (a) Excitable laser's output behavior in response to a single input pulse with different energies. The integrated excitable laser simulations also follow a similar relationship profile but with output pulse widths $\sim 10^6$ smaller (picoseconds compared to microseconds). The electrical power biasing the gain section was $I_g v_L = 88$ mW. (b) Response of the excitable laser when implemented as a coincidence detector: the excitable laser is biased such that it will not fire unless two excitatory pulses are temporally close together. Output response is strongly dependent on the temporal correlation of two inputs. Average input power is kept constant with changing pulse interval. Insets show the transient pulse dynamics of the integrated laser, i.e., the intensity $I(t)$ and recovery of gain carriers $G(t)$ as a result of input signal $\theta(t)$, for pulses that are (i) closer versus (ii) farther apart. Reproduced from Shastri *et al.*, Sci. Rep. **6**, 19126 (2016) [31]. Licensed under CC BY.

Selmi *et al.* [37,89] provided experimental evidence of neuron dynamics in a micropillar laser with SA [Fig. 12(b)]. This laser has a diameter of 4 μm with a typical height of up to 10 μm [127]. The operation of the laser relies on efficient optical pumping of the gain and absorber sections, which is obtained by precisely engineering the multilayer mirrors comprising the cavity of the laser [87]. The laser consists of active and unpumped regions that consist of two and one InGaAs/AlGaAs QWs, respectively. The goal is to have a high pumping efficiency of the gain medium, while having no pump at all at the SA QW. This is achieved by having the gain and SA QWs placed at the antinode of the field at cavity resonance (980 nm), with the SA QW simultaneously being at a node of the pump fields in the whole range of possible pump wavelengths (between 795 and 805 nm) [87].

A characteristic feature of a Class 1 excitable system is the presence of steplike behavior at the excitable threshold between the output pulse energy (amplitude response) and the input pulse energy (perturbation amplitude), and furthermore, a static control of the threshold with the bias pump intensity [37]. A decrease in the bias pump intensity results in an increase of the excitable threshold and a decrease in the amplitude response, until excitable behavior completely disappears with no well-defined threshold [Fig. 15(a)]. Here, the system enters a conventional laser regime, called gain switching. For bias pumps close to the self-pulsing (Q-switching) threshold, the excitable threshold has a linear dependence with the pump level; for lower pump values, the fluctuations in the amplitude response are roughly the same order as the response jump. This makes it difficult to identify the excitable threshold.

Figure 14

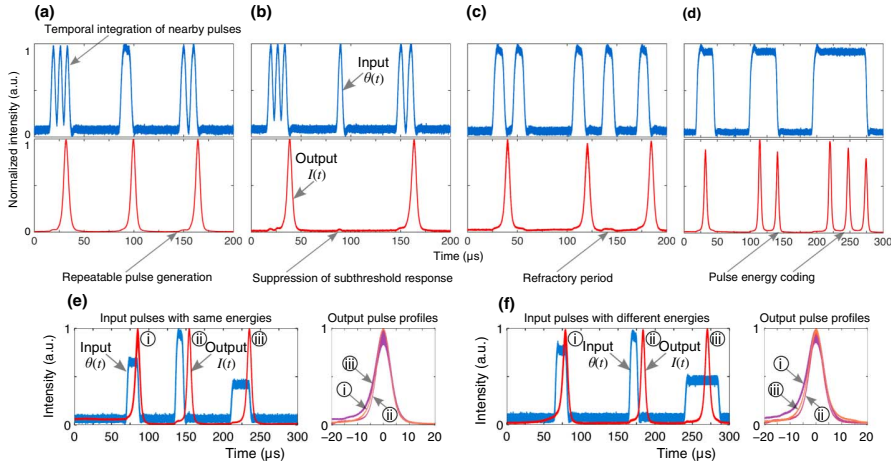

Excitable dynamics of the graphene fiber laser. Note the blue and red curves correspond to input and output pulses, respectively. Panels (a)–(c) show that excitatory activity (temporal integration of nearby pulses) can push the gain above the threshold, releasing spikes. Depending on the input signal, the system can lead to repeatable pulse generation [panel (a)], or suppressed response due to the presence of either sub-threshold input energies [integrated power $\int |\theta(t)|^2 \mathrm{d}t$, panel (b)] or a refractory period during which the gain recovers to its resting value and the laser is unable to pulse (regardless of excitation strength) [panel (c)]. Panel (d) shows typical bursting behavior i.e., emission of doublets (two spikes) and triplets (three spikes) when a strong input drives the system over the threshold to fire repetitively. Panels (e) and (f) show restorative properties (repeatable pulse reshaping) of spike processing; inputs with either the same [panel (e)] or different [panel (f)] energies. Reproduced from Shastri *et al.*, Sci. Rep. **6**, 19126 (2016) [31]. Licensed under CC BY.

Inputting spike doublets (two identical perturbations separated by an interspike interval) to the laser reveals another key feature of an excitable system: the presence of a refractory period. The arrival of a second excitable pulse, close to the first perturbation that has triggered an excitable response, may result in a decreased response level [Fig. 15(b)] if the gain is still recovering to the steady state (relative refractory period) until being completely repressed for a sufficiently small interspike interval (absolute refractory period). The excitable regime ceases to exist with the disappearance of the discontinuous response to the second perturbation. If the second pulse arrives after the carrier recovery is complete, the intensity of the triggered pulse will be identical to the first response, and the system can be considered to have left the refractory period. The absolute and relative refractory periods are measured to be below 200 ps and in the 200–350 ps range, respectively.

The dynamical evolution of the excitable laser [Figs. 15(c) and 15(d)], i.e., the intensity $I(t)$, recovery of the gain $G(t)$ and SA $Q(t)$ carriers, and the net gain $\Gamma(t) = G(t) - Q(t) - 1$, as a result of a double delta perturbation before and after its refractory period, aids in revealing the underlying physical mechanism driving the system response. As explained by Selmi *et al.* [37], the response to the second perturbation is dependent on the intensity experiencing a positive net gain for a sufficiently long period of time, i.e., only if $\Gamma(t)$ reaches positive values is a pulse emitted, and its amplitude is dependent on recovery of the carrier densities relative to the steady state.

In conclusion, the two-section gain and SA-laser neuron model offers a rich repertoire of useful dynamical behaviors, including the excitable dynamics also found in the time-resolved spiking of neurons. These excitable lasers have been shown to be amenable to low-level spike-processing tasks, including temporal pattern detection and

Figure 15

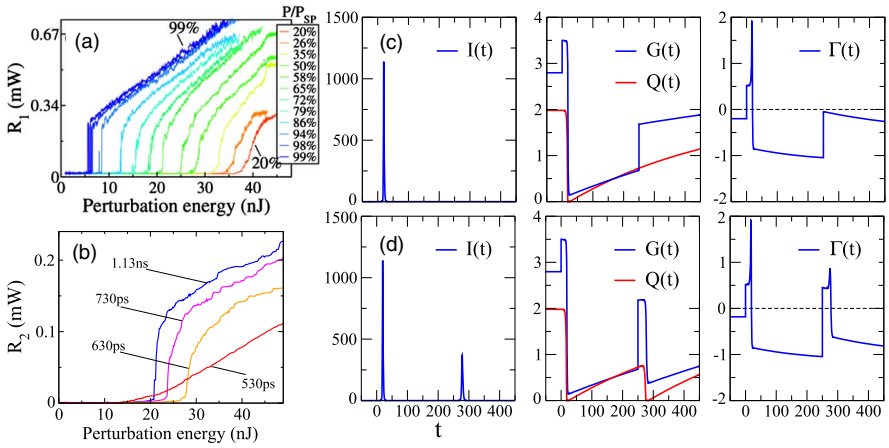

(a) Amplitude of the response R_1 to a single pulse perturbation versus perturbation energy E for varying bias pump P relative to the self-pulsing threshold $P_{SP} = 694$ mW. (b) Amplitude of the response to a second perturbation pulse after a first pulse has been sent at $t = 0$, whose amplitude is 20% above the excitable threshold and has triggered an excitable response, for different delays between the two pulses. Bias pumping is $0.71P_{SP}$. (c) and (d) Intensity $I(t)$, recovery dynamics of carriers $G(t)$, $Q(t)$, and net gain $\Gamma(t)$ for a double delta perturbation at $t_0 = 0$ and $t_1 = 250$. The second perturbation is (c) below and (d) above the excitable threshold. The initial state is the steady state. Reprinted with permission from Selmi *et al.*, Phys. Rev. Lett. **112**, 183902 (2014) [37]. Copyright 2014 by the American Physical Society. Figures 2, 4, and 5 from http://link.aps.org/abstract/PRL/v112/p183902.

stable recurrent memory [31], that are useful for higher level processing. As such, it has been argued in Ref. [31] that this platform can simultaneously exhibit logic-level restoration, cascadability, and input–output isolation, which are fundamental challenges in optical information processing. Both types of gain and SA-laser neurons require sufficient pump power ($I_g v_L = 88$ mW and $P_{SP} = 694$ mW, respectively) in order to be biased in an excitable regime, in addition to cooling power to prevent associated power dissipation from affecting temperature. In the case of the optically pumped nanopillar, heat generation and cooling take place in the external pump laser, whereas the electrically pumped DFB excitable laser requires that cooling be applied to the integrated laser neuron itself. As will be discussed in Section 4, it is possible to use an electrical injection approach to support a scalable, wavelength-based networking technique, as proposed in Ref. [28]. It may also be possible to support wavelength networking by using an optical injection technique, i.e., as proposed in Ref. [35], which would potentially operate at higher bandwidths, although the details of such an architecture have yet to receive significant investigation.

3.2. Semiconductor Ring and Microdisk Lasers

Circular-cavity lasers are a class of semiconductor lasers that have also been shown to exhibit dynamic excitability [92,128,129] and have been investigated for application as a computational primitive [33,36,94]. Their circular symmetry forms a resonator cavity with two equistable counterpropagating normal modes per frequency, leading to multistable behavior. Excitability can arise when this symmetry is broken, in which case one of the modes' basin of attraction is suppressed and the system allows for only transient excitation of this mode. Recently, two research groups used this phenomenon to characterize excitable lasers as optical neurons: Coomans *et al.* investigated an architecture based on semiconductor ring lasers (SRLs); and Van Vaerenbergh *et al.* investigated microdisk lasers (MLs) [33,36]. Notably, the effects of cascadability (i.e., one laser driving one or more others) have been considered in this type of laser, excitable pulses maintained by a chain of multiple of such lasers has been demonstrated. Cascadability is one of several requisite properties associated with creating larger systems of excitable laser elements, further discussed in Section 4.

3.2a. Semiconductor Ring Lasers

An SRL consists of an electrically pumped III–V ring resonator coupled to a waveguide. Demonstrations of alternate oscillations were observed experimentally [130]. In addition, excitable pulsations were observed experimentally in SRLs by Gelens *et al.* [92]. That group analyzed the dynamical system and found that the SRL falls into the Class 2 excitability [131] category. Recently, Coomans *et al.* theoretically investigated the engineering of one SRL for optical spike excitation [33] and the excitation of one SRL via another [93].

Principle of operation: A pulsating SRL was monolithically fabricated on an InP-based multi-quantum-well substrate with a "racetrack" geometry [131] (see Fig. 16). The device operates in a single-transverse, single-longitudinal mode at $\lambda = 1.56$ μm. The circular geometry makes this mode degenerate, resulting in two counterpropagating modes, which are coupled to each other in two ways: linearly by "intermodal coupling" and nonlinearly by cross-gain saturation [see Eqs. (5a)–(5d)].

Sorel *et al.* [130] had shown that, for a certain phase of the intermodal coupling coefficient (around $\phi_k \approx 1.5$), the SRL has three different regimes for different pump currents (see Fig. 17). In regime A, the ring laser operates bidirectionally and both modes have constant power. In regime B, however, alternate oscillations appear wherein both counterpropagating modes harmonically exchange energy over time. This behavioral change corresponds to a Hopf bifurcation. Most interestingly, in

regime C, the ring laser operates quasi-unidirectionally, without oscillations. However, injecting light into the cavity may cause the system to switch between modes. Imperfections during fabrication cause a break in the invariance symmetry along the ring, which explains why regimes A and B were not experimentally fully bidirectional in Fig. 17(a). This asymmetry depends on imperfections in the waveguide, output coupler, or scattering center. It can be, for example, tuned using a flat-face fiber with piezoelectric controller and a bias current in the bus waveguide (Fig. 16).

The dynamical behavior of the laser can be expressed with a set of coupled semiclassical Lamb equations. The counterpropagating modes are represented as E^+ and E^- [slow-varying complex amplitudes with an additional complex phase of $\exp(-j\omega t)$]; $|E^{\pm}|^2$ denotes the number of photons in each mode, "+" denotes counterclockwise (CCW), and "−" denotes clockwise (CW). The number of free carriers in the cavity is N. The following model was adapted from Refs. [94,130,131]:

$$\frac{\mathrm{d}E^+}{\mathrm{d}t} = \frac{1}{2}(1-j\alpha)(G^+ - \gamma_{\mathrm{ph}})E^+ + j\Delta\omega E^+ - j\eta_c\gamma_{\mathrm{in}}E_{\mathrm{in},1} + k(1-\delta)\exp[j(\phi_k - \Delta\phi_k/2)]E^-, \tag{5a}$$

$$\frac{\mathrm{d}E^-}{\mathrm{d}t} = \frac{1}{2}(1-j\alpha)(G^- - \gamma_{\mathrm{ph}})E^- + j\Delta\omega E^- - j\eta_c\gamma_{\mathrm{in}}E_{\mathrm{in},2} + k(1+\delta)\exp[j(\phi_k + \Delta\phi_k/2)]E^+, \tag{5b}$$

$$\frac{\mathrm{d}N}{\mathrm{d}t} = \mu I_0 - \gamma_c N - G^+|E^+|^2 - G^-|E^-|^2, \tag{5c}$$

$$G^{\pm} = \frac{\Gamma g_N(N-N_0)}{1+\Gamma\varepsilon_{\mathrm{NL}}(|E^{\pm}|^2 + 2|E^{\mp}|^2)}. \tag{5d}$$

Equations (5a) and (5b) describe the evolution of each counterpropagating mode amplitude. α is the linewidth broadening factor (also called Henry factor or alpha factor), γ_{ph} is the field decay rate, and $\Delta\omega = \omega - \omega_0$ is the detuning between the injected field

Figure 16

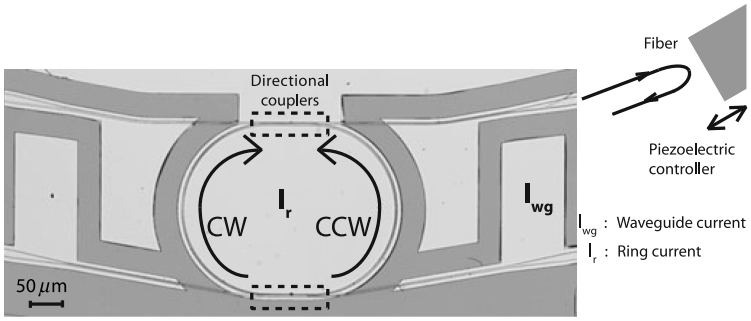

Experimental SRL setup. Two waveguides, referred to as bus waveguides, are positioned next to the ring so that light can be directly coupled between waveguide and ring. Metallic contacts are deposited on top of the ring and on all four pathways of the bus waveguides. The power emitted from the chip is collected with a multimode fiber. The cleaved facet of the fiber also serves as a controllable backscattering element. Four waveguide contacts are depicted, of which only the one denoted by I_{wg} is biased. I_r is the bias current of the SRL. Reprinted from Gelens *et al.*, Eur. Phys. J. D. **58**, 197–207 (2010) [131] with permission of Springer.

E_{in} and the resonance cavity frequency ω_0. Light is injected into the cavity via an external waveguide, represented by E_{in}, with a coupling efficiency η_c and rate γ_{in}. Localized reflections (dubbed backscattering) produce a linear coupling between the two fields, characterized by an amplitude k and a phase shift ϕ_k. Asymmetries in the backscattering strength and phase are represented as δ and $\Delta\phi_k$, respectively. Equation (5c) describes the evolution of free carriers in the semiconductor cavity. μ is the dimensionless, normalized injected current ($\mu = 1$ at laser threshold), $I_0 \approx (\gamma_{\text{ph}}/\Gamma g_N + N_0)$ the actual pump current at laser threshold, and $G^{\pm}$ is the gain coefficient of each mode. In Eq. (5d), g_N is the differential gain; Γ, the confinement factor of the mode in the cavity; N_0, the transparency free carrier number; and ϵ_{NL}, the nonlinear gain-suppression coefficient, reflecting *carrier heating* and *spectral hole burning* phenomena.

Equations (5a)–(5d) form a dynamical system and can be represented in a phase portrait. It has been shown that for time scales slower than typical oscillations of the system, the total number of photons in the cavity ($|E^+|^2 + |E^-|^2$) is approximately constant. Therefore, the relative magnitude of the amplitude and phase of the counterpropagating modes suffice to describe the laser state. To aid geometrical visualization, two auxiliary angular variables were introduced [131]: $\theta = 2\arctan(|E^+|/|E^-|) - \pi/2 \in [-\pi/2, \pi/2]$ and $\phi = \arg(|E^+|/|E^-|) \in [0, 2\pi]$. Here, θ measures the relative power distribution among the two fields (e.g., $\theta = \pi/2$ for the field concentrated in the E^+ mode) and ϕ the relative phase.

For a specific value of intermodal coupling and pump current, the basins of attraction of the stable points are separated by a manifold in the shape of a symmetric spiral [see Fig. 18(a)]. However, an asymmetry $\delta > 0$ causes the CW basin of attraction to shrink significantly to the point where its stable state becomes metastable [see Fig. 18(b)]. For δ large enough, in practice the laser will always operate in the CCW mode. By injecting a short optical pulse centered at the resonance frequency and with a

Figure 17

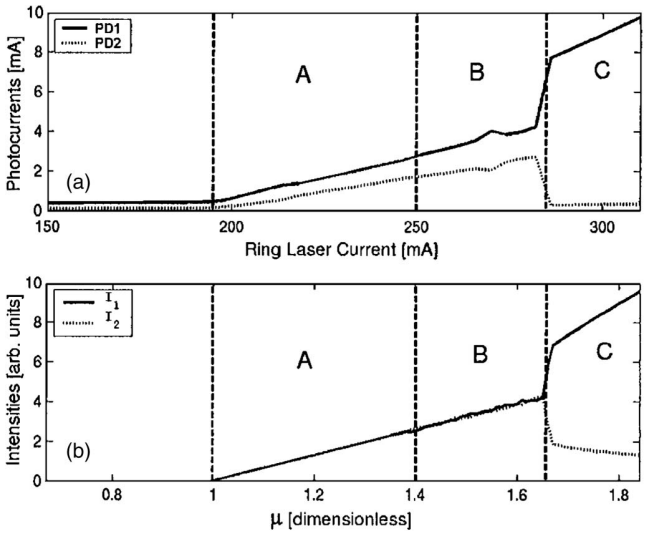

(a) Experimental (dc) L–I curves of a sample SRL device. (b) Theoretical time-averaged L–I curve obtained via optimization of Eqs. (8)–(11) in [130] with the Runge–Kutta algorithm. $\phi_k \approx 1.5$. The vertical lines at $\mu_H = 1.4$ and 1.65 indicate two Hopf bifurcations in the dynamical system. Reprinted with permission from [130]. Copyright 2002 Optical Society of America.

particular phase with respect to the CCW mode, one can deterministically force the system state to cross both branches of the CW stable manifold (gray area in Fig. 19). After that, the relaxation trajectory involves quickly going around the CW basin to return to the CCW point (see Fig. 19), producing a short pulse in the CW mode. Interestingly, the carrier density is not involved in the excitable excursion—it is a transient redistribution of energy between the two counterpropagating modes, unlike other excitable lasers.

Results: Exciting an SRL in a controllable way can practically prove to be a major hurdle. In Fig. 19, the initial direction of the perturbation is critically influenced by the phase of the short pulse with respect to the laser state, which imposes a difficult synchronization constraint. Moreover, the power of the injected pulse is 8 orders of magnitude weaker than the power of the CCW mode. Out-of-phase optical injection might cause the system to cross the CW basin twice, resulting in double pulses [see Fig. 19(b)]. Multipulse excitation can also be caused by noisy perturbations, due to the proximity of the excitation excursion to the CW stable manifold. Finally, due to the folded shape of the excitability threshold in the phase portrait, there is no concept of excitatory or inhibitory perturbation—which is characteristic of Class 2 excitability as discussed in Ref. [75] (see Fig. 8).

The high-speed excitable excursion are promising for neuro-inspired information processing applications in photonics. Coomans *et al.*, in a later work [93], investigated the coupling between two SRLs via a single waveguide bus and simulated cascadable, unidirectional excitations across the neighboring SRLs (Fig. 20). The CW mode of one SRL can couple to the CCW mode of the other SRL. However, coupling the two SRLs has an effect on the dynamics of the individual lasers. Nonetheless, this scheme may be amenable to a coherent phase-based approach to networking, as discussed in Section 4.1.

3.2b. Microdisk Laser

Microdisk lasers (MLs), similar to SRLs, consist of disk-shaped resonators coupled to a bus waveguide. Stable, unidirectional lasing operation of MLs was recently demonstrated experimentally [128,129]. However, by combining an electrical pump with optical injection, Alexander *et al.* theoretically and numerically showed that an ML can also exhibit Class 1 excitability [94]. Moreover, Van Vaerenbergh *et al.* numerically analyzed spike transfer and other dynamics between two MLs [36].

Principle of operation: MLs have been fabricated using the hybrid III–V on a SOI hybrid platform. An ML is a disk-shaped InP laser cavity with an electrically pumped

Figure 18

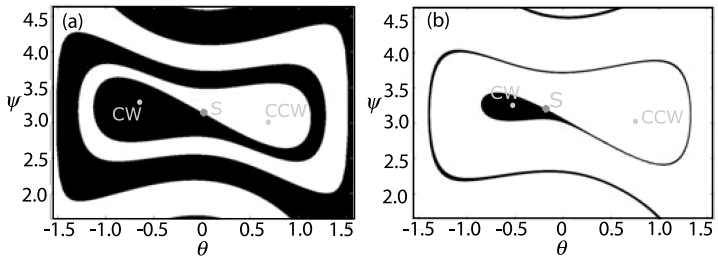

Phase portrait of Eqs. (5a)–(5d). Stable manifold separating the two basins of attraction (black and white) of both asymmetric stable states for $\mu > 1.65$, $\phi_k = 1.5$, and $\Delta\phi_k = 0$. $\delta = 0$ and 0.05 in (a) and (b), respectively. Reprinted from Gelens *et al.*, Eur. Phys. J. D **58**, 197–207 (2010) [131] with permission from Springer.

InAsP QW gain section, bonded on top of a SOI substrate [128,129] (see Figs. 21 and 22). A single-mode-sized disk supports two counterpropagating *whispering gallery* modes, which are evanescently coupled to a silicon waveguide in the SOI layer. Similar to SRLs, the lasers are electrically pumped and can be optically injected from both directions of the bus waveguide. MLs share the same phenomenology with SRLs, and thus can exhibit the same excitability behavior of SRLs via symmetry breaking. In their work, instead of using a flat-faced fiber coupled to the bus waveguide, Van Vaerenbergh *et al.* induced asymmetry in the system via CW optical injection in one of the two counterpropagating whispering-gallery modes, causing one mode to be dominant and the other to be suppressed.

In this operating point—the vicinity of *saddle-node on a limit circle bifurcation* (SN1 in Fig. 23)—the laser possesses Class 1 excitability (see Fig. 8), whereby small optically injected perturbations cause linear response, but for inputs greater than a certain threshold, the laser produces an optical pulse in the suppressed mode. This behavior resembles the previously discussed LIF model of a spiking neuron, as opposed to the resonate-and-fire proposed by Coomans *et al.* [33]. Similar to the proposed SRL, the carrier density is not involved in the excitable excursion, illustrated by the fact that every downward pulse in the dominant mode is accompanied by an approximately equal upward pulse in the suppressed mode, which are coupled to the bus waveguide in opposite directions and can be used to excite other disks (Fig. 22).

Results: The excitation mechanism is as follows (Fig. 23). The CW input locks the microdisk just above the SN1 bifurcation. Pulses at the other input of the splitter cause perturbation of the locking signal. Because of Class 1 excitability, a pulse can be categorized as inhibitory or excitatory according to a combination of its intensity, duration, and, most importantly, phase relative to the CW input (see Fig. 24). Consecutive pulses can be integrated to overcome the spiking threshold.

Figure 19

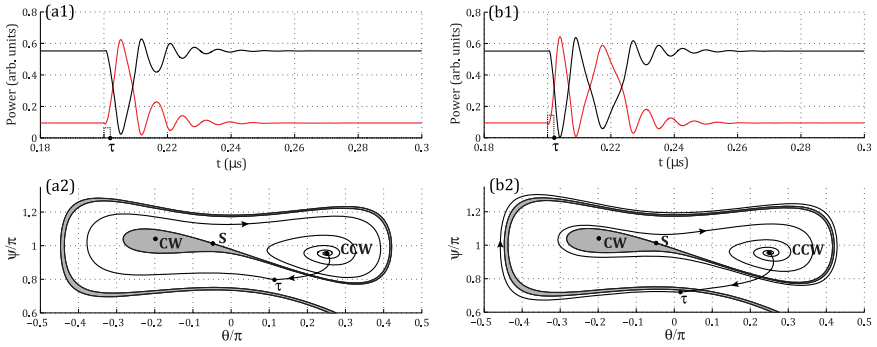

Simulation of Eqs. (5a)–(5d) when optically injecting a 2-ns-wide square pulse. (a1), (b1) Time traces of the modal intensities. The CW (CCW) modal power is depicted in red/gray (black). The injected pulse is shown by a dashed black line. Note that the optically injected pulse power is scaled up by a factor of 10^7 in this plot. τ indicates the time at which the injected pulse ends. (a2),(b2) Two-dimensional phase space trajectory corresponding to the time trace. The point τ also corresponds to the moment when the injected pulse ends. S indicates the location of the saddle. The basin of attraction of the CW (CCW) state is depicted in gray (white). Parameter values: (a1),(a2) $\delta = 0.045$ and $E_i = 8 \times 10^{-5}$, and (b1),(b2) $E_i = 1.2 \times 10^{-4}$, resonant detuning, phase difference $= 1.3\pi$. Reprinted with permission from Coomans *et al.*, Phys. Rev. E **84**, 036209 (2011) [33]. Copyright 2011 by the American Physical Society. Figures 1 and 2 from http://link.aps.org/abstract/PRE/v84/p036209.

One clear practical advantage of the system proposed by Alexander *et al.* is that the system is much more robust to phase noise. While SRLs without optical injection are sensitive to the phase difference between input and the laser state, which is uncontrollable in practical setup, the ML's phase sensitivity is respective to the locking CW signal, which can be more easily controlled externally [94]. Moreover, roughly

Figure 20

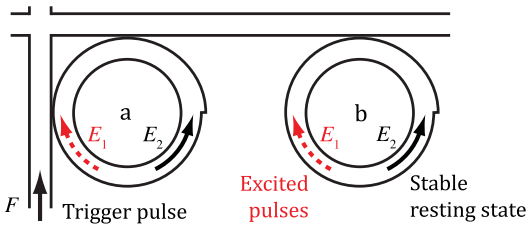

Schematic representation of the coupling scheme for excitable asymmetric SRLs considered in this paper. The CW (CCW) mode of SRL a (SRL b) is coupled in the CW (CCW) mode of SRL b (SRL a). The notch to the ring cavity is merely added as a visual indication of the asymmetry of the cavity. The curved black arrow indicates the stable resting state; the dashed red arrow indicates the propagation direction of excitable pulses. The injected trigger pulse F is shown by a straight black arrow. Reprinted with permission from Coomans *et al.*, Phys. Rev. E **84**, 036209 (2011) [33]. Copyright 2011 by the American Physical Society. Figure 4 from http://link.aps.org/abstract/PRE/v84/p036209.

Figure 21

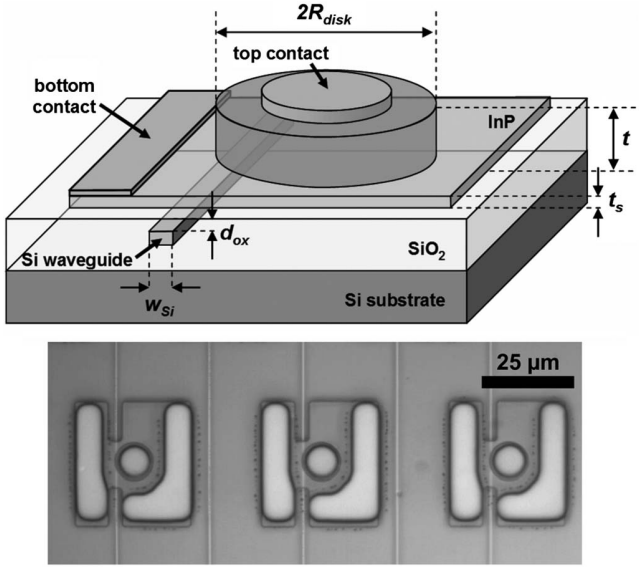

Top: schematic drawing of the heterogeneous microdisk laser structure, showing the metal contact position and the output SOI wire-waveguide. Bottom: optical microscope image of three fabricated microdisk lasers, just before the deposition of the metal contacts, showing the microdisk cavity, the InP bottom contact layer, the SOI wire, and the contact bias etched into the benzocyclobutene (BCB) planarization layer. Copyright 2008 IEEE. Reprinted, with permission, from Van Campenhout *et al.*, J. Lightwave Technol. **26**, 52–63 (2008) [129].

speaking, 25% of a random-phase input pulse with sufficient amplitude would result in excitation (Fig. 24), which allows for a large margin of error in phase. Phase shift accumulation in optical links can be counteracted by tunable phase shifters, e.g., heaters, removing a potential hurdle for interconnecting microdisks in an integrated platform.

Van Vaerenbergh *et al.* proposed a connection topology of two identical MLs as depicted in Fig. 25. The objective of this simulation was to demonstrate unidirectional excitation of Disk 2 via Disk 1. The time traces are presented in Figs. 26 and 27. Microdisks and waveguides are laid out in a way such that suppressed modes of each disk are sent to each other, allowing each ML to excite the other. Note that the calculated width of the pulse produced by the ML is of the order of 0.2 ns (Fig. 25), much shorter than ∼10 ns of SRLs (Fig. 19).

However, a perfectly symmetrical pair of coupled disks, with a relative phase corresponding to excitatory connection, produce recurrent excitations (Fig. 26) due to successive excitations of one laser by the other. Unidirectional excitation demands the symmetry of the pair to be broken by fine-tuning either the relative amplitude

Figure 22

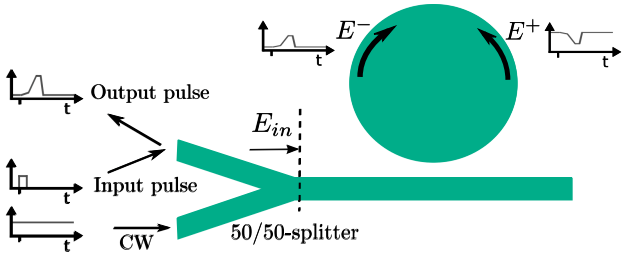

"Neuron" topology; using a constant locking signal (CW), the microdisk gets locked just above the SN1-bifurcation. Pulses at the other input of the splitter perturb the microdisk, possibly causing excitation. The energy peak in the E mode that comes with this excitation can be seen as the output pulse. Reprinted with permission from [94]. Copyright 2013 Optical Society of America.

Figure 23

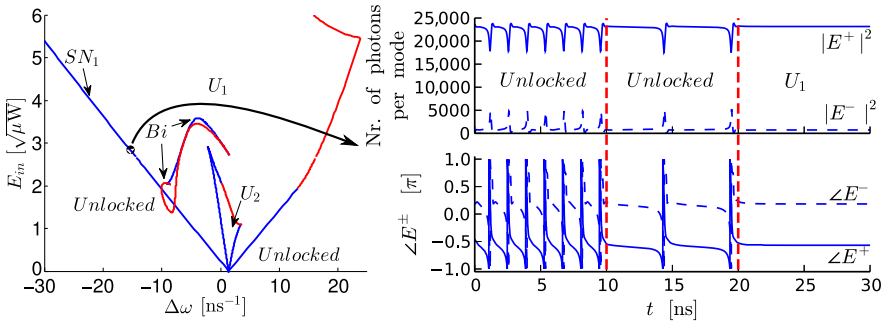

Left: bifurcation lines and locking regions for $I = 2.3$ mA; red lines represent Hopf bifurcations, blue lines are limit points. Time traces: crossing the SN1 bifurcation at $\Delta\omega = -15$ ns^{-1}, $|E_{\text{in}}| = 2.77$ μW$^{1/2}$. At $t = 10$ ns, the locking amplitude is raised from range 2.65 to 2.76 μW$^{1/2}$; at $t = 20$ ns, the bifurcation is crossed by again increasing $|E_{\text{in}}|$ to 2.78 μW$^{1/2}$. Reprinted with permission from [94]. Copyright 2013 Optical Society of America.

or phase of CW locking signals. Consequently, although the coupling of the two lasers does not physically affect the dynamics of individual lasers (like in Ref. [33]: SRLs), the direct "connection weight" from Disk 1 to Disk 2 cannot be set independently from the inverse weight.

In conclusion, these circular cavity laser systems very elegantly resulted in excitable behavior. Two elements can be interconnected via a passive waveguide and are, in general terms finely controlled by phase tuning. Interconnection and cascadability were proposed and numerically predicted for both SRLs and MLs. SRLs reviewed in Section 3.2a could present resonate-and-fire behavior near the Hopf bifurcation, allowing for the system to respond to precise interspike intervals. Injected lasers are usually very sensitive to the phase of the perturbing pulse; however, the ML

Figure 24

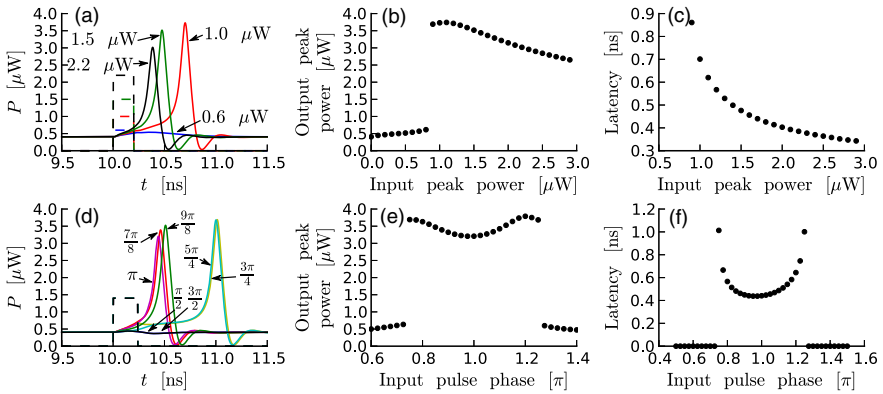

(a)–(c) Response to pulses of fixed length (0.2 ns), for different pulse powers, out of phase with the locking signal. (a) Time traces. (b) Output peak power as a function of input peak power. (c) Pulse latency as a function of input peak power. (d)–(f) Response to pulses of fixed peak power and length (1.4 μW, 24 ns), but varying phase. (d) Time traces. (e) Output peak power as a function of phase. (f) Pulse latency as a function of input pulse phase. Reprinted with permission from [94]. Copyright 2013 Optical Society of America.

Figure 25

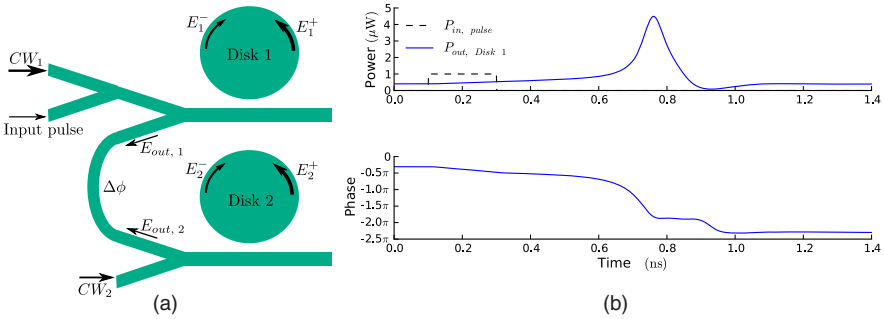

(a) Topology used to cascade two microdisks. The connection between the two lasers imposes a phase difference $\Delta\phi$. (b) Input and output power of the first disk when the second disk is "turned off" (current as well as locking signal are absent). The bottom graph shows the phase difference between the output pulse and the locking signal. Reprinted with permission from [36]. Copyright 2013 Optical Society of America.

reviewed in Section 3.2b shows good robustness to input pulse phase noise [Fig. 24(e)]. Networking for optically injected lasers will be further discussed in Section 4, and possible networking approaches in Section 4.1.

3.3. Two-Dimensional Photonic Crystal Nanocavities

There has been exciting research on exploring excitability in periodic nanostructures called *photonic crystals* (PCs). A PC is analogous to a semiconductor in that the propagation of photons is affected in the same way as the periodic potential in a semiconductor crystal influences the flow of electrons, by defining allowed and forbidden electronic energy bands [132,133]. PCs are composed of varying periodic dielectric constant materials (alternating low and high) in up to three dimensions. This results in a *photonic bandgap* (PBG) where some frequencies are not allowed to propagate. Light can be controlled and manipulated by introducing defects that alter the periodicity and break the completeness of the PBG. The localization of light in the PBG region leads to the design of PC-based optical devices.

Figure 26

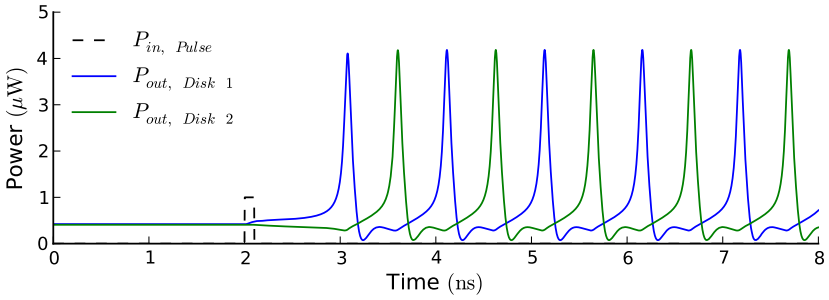

Input pulse power and output power of both disks. Both disks are pumped with a 2.3 mA current and $\Delta\phi = 2.8$ rad. The locking signals for both disks are 3.8 $\mu W^{1/2}$. The input pulse is 1 ns strong and 0.1 ns long. Reprinted with permission from [36]. Copyright 2013 Optical Society of America.

Figure 27

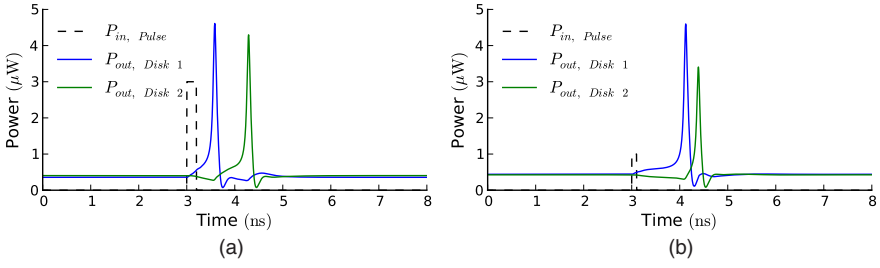

(a) Symmetry breaking by difference in locking amplitude. The locking signal for the first disk has an amplitude of 4 $\mu W^{1/2}$. For the second disk, the locking amplitude is 3.9 $\mu W^{1/2}$. Both disks are pumped with a 2.3 mA current; $\Delta = 2.8$ rad. The input pulse is 3 $\mu W^{1/2}$ strong and 0.2 ns long. (b) Symmetry breaking by difference in locking phase. The locking signals for both disks have an amplitude of 3.55 $\mu W^{1/2}$, while $\phi_{CW2} = \phi_{CW1} + \pi/2$. Both disks are pumped with a 2.3 mA current; $\Delta = 4.2$ rad. The input pulse is 1 $\mu W^{1/2}$ strong and 0.1 ns long. Reprinted with permission from [36]. Copyright 2013 Optical Society of America.

Soljačić *et al.* [134] proposed an analytical model along with numerical simulations for optical bistable switching in a nonlinear PC. Optical bistability in microcavities and nanocavities is of particular interest for potential applications in all-optical transistors, switches, logical gates, and memory [135,136]. Since then, there has been an active investigation of self-pulsing and excitability in two-dimensional (2D) PC resonators [39,95,137,138] and in PC nanocavities [34,139–142]. Both optical and electronic nonlinearities have been exploited to observe these phenomena. The latter is, however, difficult to achieve and observe due to the weak signals at play with fast time scales (picosecond to nanosecond). In the optical domain, third-order Kerr nonlinearity plays a key role in achieving bistability and excitability. The key is to enhance this nonlinearity and reduce operation thresholds with tight confinement of light. Reducing both the optical volume and optical losses leads to a decrease of the bistability threshold since the latter scales as V/Q^2 (where V is the optical mode volume and Q the cavity quality factor) [134,135]. Both Yacomotti *et al.* [39] and Brunstein *et al.* [34] demonstrated Class 2 excitability in a 2DPC. In Class 2 excitability there are two distinct time scales at play: the fast one is responsible for the firing of the excitable pulse, and the slow one determines the full recovery to the quiescent state [39,74]. In the 2DPCs, the fast and slow time scales are governed by the carrier recombination time and the thermal relaxation due to thermal diffusion, respectively.

The 2D PC band-edge resonator by Yacomotti *et al.* [39] [Fig. 28(a)] consists of a graphite lattice with cylindrical air holes patterned into a 20 μm × 20 μm, 240 nm thickness InP slab through a silica mask. The lattice constant is 775 nm and the hole diameter is 230 nm. The InP slab contain four QWs of InAsP whose luminescence is centered around 1500 nm. A Bragg mirror below the 2DPC ensures strong light confinement in the vertical direction in the PC slab. Brunstein *et al.* [34] have a similar structure (lattice constant of 450 nm and hole diameter of 240 nm) but with a suspended InP membrane (10 μm × 50 μm) and without the Bragg mirror [Fig. 28(a)]. The cavity mode is probed with a 120 fs width, 80 MHz repetition rate 30 nm broadband signal with a central wavelength of 1570 nm. A carrier-induced refractive index change results in a fast nonlinear response [144]. This blueshifts and narrows the resonance as a function of the injected (pump) power, which changes the intensity of the output (reflected signal) [139]. A range of wavelengths [Figs. 28(c) and 28(d)] contribute to the hysteresis cycles, as shown in Fig. 28(e) for different detunings $\Delta\lambda = \lambda_0 - \lambda_{\text{inj}}$, where λ_0 is the resonance wavelength and λ_{inj} is the injected wavelength. The hysteresis cycle corresponds to electronic bistable operation. For excitability, the system is biased above the bistability threshold so that both the bistable branches (lower and upper states) coexist. The system can be switched from the lower state to the upper states by introducing a short perturbation. In such conditions, heating is enhanced, which increases the refractive index and thus shifts the hysteresis cycle to higher injection powers. Consequently, self-induced switching to the low output state takes place, with a subsequent cooling, giving rise to a two-time-scale transient response [34]: firing of the pulse is controlled by the fast carrier dynamics, while the recovery and pulse duration are controlled by the slower thermal dynamics.

Principle of operation: A large repertoire of nonlinear dynamics, including excitability, result from strong coupling between a high-Q cavity mode, carrier concentration in a gain medium, and thermal dynamics. Typically, the time scales associated with thermal diffusion effects are on slow microsecond or millisecond scales, but they can contribute to subnanosecond dynamics in a 2DPC because of the very small cavity dimensions. The key physical effects can be understood in terms of the thermo-electro-optic model:

$$\frac{dE}{dt} = -E(1 + i\theta) + (1 - i\alpha)(N - N_t)E + E_I, \tag{6a}$$

$$\frac{dN}{dt} = -\gamma[N + (N - N_t)|E|^2], \tag{6b}$$

$$\frac{d\theta}{dt} = -\gamma_{th}\{\theta - \theta_0 + cE_I[\mathrm{Re}(E) - |E|^2]\}, \tag{6c}$$

where E is complex field amplitude, N is normalized carrier density, and θ is cavity resonance detuning as a result of temperature. While we refer the reader to Ref. [39] for a complete definition of all variables, we point out several features here.

Equation (6a) is a complex differential equation, the term $-E(1 + i\theta)$ describing cavity leakage (real part) and thermal contributions to the lasing frequency (imaginary part), which depend on θ. The second term describes electro-optic effects of absorption/gain as well as electronic carrier contributions to the lasing frequency. The third term, E_I, is also complex and represents the injected optical signal. Equation (6b) is the familiar differential model of a semiconductor carrier population with optical illumination. Equation (6c) describes dynamic changes in the lasing frequency relating to temperature shifts. θ_0 is the resonance frequency at linear equilibrium, relative to

Figure 28

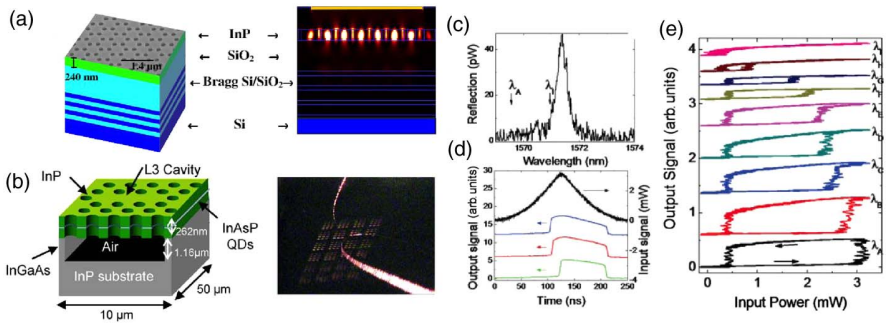

(a) Sketch of the 2DPC (scanning electron microscopy image of the graphite lattice on top) and cross-section distribution of the electromagnetic energy from a finite-difference time domain 3D numerical simulation of the real structure. The horizontal line on the top represents the extension of the injected CW resonant plane wave. Note the confinement in the InP slab. Reprinted with permission from Yacomotti *et al.* Phys. Rev. Lett. **97**, 143904 (2006) [39]. Copyright 2006 by the American Physical Society. Figure 1 from http://link.aps.org/abstract/PRL/v97/p143904. (b) Schematic of the PC sample showing the L3 cavity and image of the whole sample and the fibered taper. Copyright 2010 IEEE. Reprinted, with permission, from Brunstein *et al.*, IEEE Photon. J. **2**, 642–651 (2010) [143]. (c)–(e) Experimental data of the 2DPC reported in [34]. Reprinted with permission from Brunstein *et al.*, Phys. Rev. A **85**, 031803 (2012) [34]. Copyright 2012 by the American Physical Society. Figure 2 from http://link.aps.org/abstract/PRA/v85/p031803. (c) Reflected (output) signal for a probe power of 95 μW. Arrows λ_A to λ_I indicate the wavelength range for the bistability experiment. (d) Time traces of input [black (top) line (right vertical axis)] and reflected [blue, red, and green lines (left vertical axis)] signals for detunings of $\lambda = 1.5$, 1.7, and 1.9 nm, respectively. (e) Hysteresis cycles showing bistable behavior. Detuning values with respect to the cavity resonance are, from λ_A to λ_I, 1.9, 1.8, 1.7, 1.5, 1.3, 1.1, 0.9, 0.7, and 0.4 nm. The duration of the switch processes is ∼6 ns for the on and off switches.

the injected signal frequency. The c parameter describes the degree of heating that occurs through optical absorption. It can be seen that by setting c to zero, θ always settles to θ_0, and Eqs. (6a)–(6b) reduce to a simple electro-optic model of a laser. θ variables (normalized frequency detunings used in equations) are related to δ variables (normalized wavelength detunings, used in Fig. 29) as $\delta = (\theta - \alpha N_t)/(1 + N_t)$.

Figure 29 shows simulated behaviors that can be seen with this model. Figure 29(a) shows the nullclines of (N, δ) when $c = 0$ (i.e., when thermal effects are neglected). The solid line indicates parts of phase space where $N/t = 0$, and the dotted line indicates where $\theta/t = 0$. Since there are no thermal effects, the dotted line is vertical, meaning θ (i.e., δ) are static at their respectively normalized equilibrium values. The two nullclines have one intersection, resulting in a single stable state, wherein most incident power is reflected. When thermal effects are introduced in Fig. 29(b), the δ nullcline becomes a curve. Biased such that the only nullcline intersection occurs between the two turning points of the N nullcline, the system has no stable fixed point and therefore settles to a limit-cycle oscillation with relaxation frequency limited by the thermal time constant, γ_{th} [Fig. 29(c)].

Figures 29(d)–29(f) introduce the notion of input perturbations to illustrate fast and slow excitability. In Fig. 29(d), the system is biased very close to producing oscillations as in Fig. 29(b); however, the nullcline intersection now being below the lower turning point means the system is stable. A slow excitable response occurs when a small input perturbs the state to the unfilled circle. This results in a large excursion seen in Fig. 29(f) (dashed line), which understandably resembles one period of the oscillations seen in Fig. 29(c). In Fig. 29(e), δ_0 is set to be slightly above the N nullcline upper turning point, as opposed to slightly below the N nullcline lower turning point. The system is stable at the intersection. If a large perturbation kicks the system to a state above the middle branch, it will rapidly collapse to the upper branch (electronic time scale). Since the initial δ bias is set close to the lower turning point, relaxation along this branch (thermal time scale) will occur for a very short time before the upper branch of N nullcline solutions vanishes. The short time spent relaxing at

Figure 29

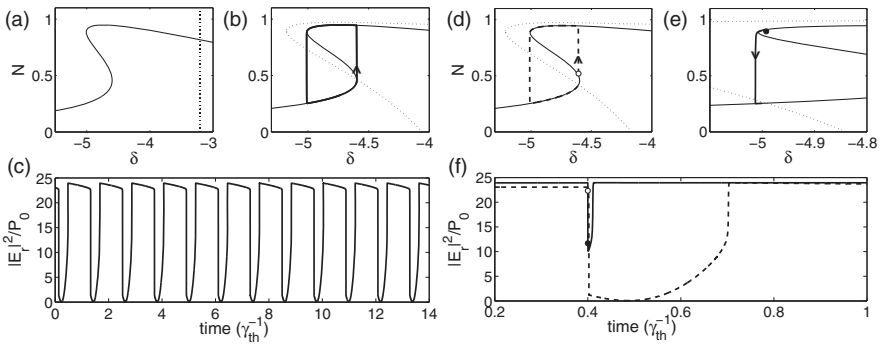

Phase portraits and time traces of the reflected (output) power ($E_r = E_I - E$) for (a) $\delta_0 = -3.2$ and $c = 0$ (no thermal effects); (b),(c) $c = 6$ (self-sustained oscillations); (d),(f) (dashed line) $\delta_0 = -3.35$, with perturbation $\Delta N = 0.1$ (slow excitability); (e),(f) (thick line) $\delta_0 = -4.225$, with perturbation $\Delta N = 0.65$ (fast excitability). Circles indicate the values of the variables $10 \times 2\tau_c$ after the perturbations. x-axis unit in time traces is $\tau_{\text{th}} = 0.84$ μs. Reprinted with permission from Yacomotti *et al.*, Phys. Rev. Lett. **97**, 143904 (2006) [39]. Copyright 2006 by the American Physical Society. Figure 3 from http://link.aps.org/abstract/PRL/v97/p143904.

the thermal time scale results in a fast excitable pulse response of the order of the electronic effect time scale, as seen in Fig. 29(f) (solid line).

Results: Brunstein *et al.* [34] tested the excitable regime of the PC nanocavity [Fig. 28(a)] by injecting perturbation pulses with varying amplitudes, as shown in Fig. 30(a). The system is tested with a pump (injection) power of 2.6 mW and detuning $\Delta\lambda = 1.6$ nm. No output (reflected) pulses are observed for perturbation powers lower than 1 μW. Increasing the perturbation power just above the threshold at 20 μW results in a 2 μs duration output response. The pulse shape is stereotypical for a further increase in input power. This is clear indication of excitable behavior. Furthermore, the confidence for Class 2 excitability is made possible by the observable presence of two distinct time scales: the fast one (nanosecond scale), driven by electronic effects, and the slow one (∼1 μs) due to thermal effects.

Further insight is also provided by Yacomotti *et al.* [39] by testing the band-edge PC resonator [Fig. 28(b)] under different (normalized) detunings δ and different perturbations [Figs. 30(b)–30(e)]. First, similar results are obtained with $\delta = -5.75$ and perturbations with 60 ps pulse widths (and period of 12.5 μs) around 800 nm [Fig. 30(b)]. These perturbations can be seen as a kick in the carrier density as the pulses are absorbed in the quantum barrier and their durations are much shorter than the electronic lifetime. Perturbation energies of less than $U_p = 1.9$ pJ result in no

Figure 30

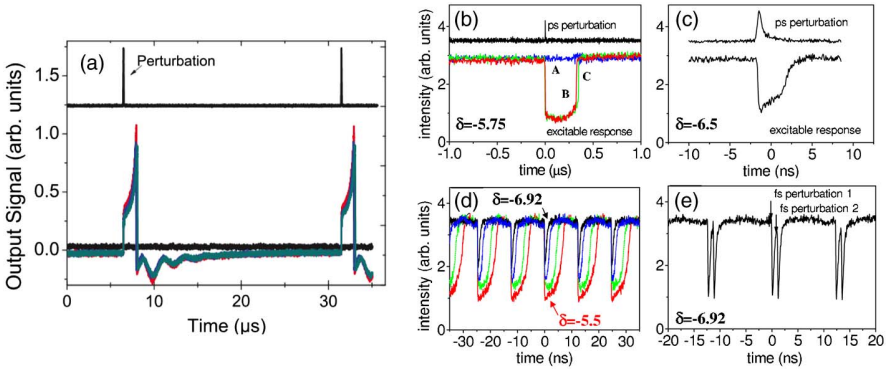

Response to input perturbations for excitable PCs in (a) Ref. [34] and in (b)–(e) Ref. [39]. (a) Excitable responses (bottom traces) to 130 ns width, 40 kHz repetition rate pulse perturbations (top trace) for different perturbation powers: 1 μW is below threshold (black line); 20, 35, and 46 μW are above threshold [red, blue, and green lines, respectively (gray lines)]. The injected signal power is set at 2.6 mW and the detuning is $\Delta\lambda = 1.5$ nm. Reprinted with permission from Brunstein *et al.*, Phys. Rev. A **85**, 031803 (2012) [34]. Copyright 2012 by the American Physical Society. Figure 4 from http://link.aps.org/abstract/PRA/v85/p031803. (b) Excitable responses (bottom traces) to 60-ps-width, 80-kHz-repetition rate pulse perturbations with perturbation energy $U_p = 1.6$ pJ (label A), 1.9 pJ (label B), and 2.5 pJ (label C) picosecond-pulse energies; normalized detuning $\delta = -5.75$. (c) Fast output pulses with $\delta = -6.5$ and $U_p = 7.4$ pJ. (d) Fast modulation test with 100-fs-width, 80-MHz-repetition rate pulses. From longest to shortest output pulse:$\delta = -5.5, -6, -6.5, -6.92$; $U_p = 6$ pJ. (e) Two pulse trains as in (d) delayed by 1 ns; $\delta = -6.92$; $U_{p,1} = 15$ pJ and $U_{p,2} = 6$ pJ. (b)–(e) Reprinted with permission from Yacomotti *et al.*, Phys. Rev. Lett. **97**, 143904 (2006) [39]. Copyright 2006 by the American Physical Society. Figure 2 from http://link.aps.org/abstract/PRL/v97/p143904.

output. However, for $U_p \geq 1.9$ pJ, the excited output is invariant with pulse width of 300 ns. Second, decreasing the detuning, $\delta = -6.5$, reduces the excitable pulse width dramatically (3 ns), while the threshold increases to $U_p = 7.4$ pJ [Fig. 30(c)]. Brunstein *et al.* [34] make similar observations [Fig. 31(a)]. Third, even though the refractory period (will be discussed shortly) is relatively long (microseconds), the system can be periodically perturbed at much higher repetition rates (80 MHz, 100 fs pulses) without significant loss of contrast [Figs. 30(d) and 30(e)] [39].

As explained in Section 2.3, excitable dynamics take place close to the onset of periodic spiking, a regime in which no stable state exists and the oscillation frequency is governed by thermal effects. Evidence of Class 2 excitability is further cemented by the demonstrated characteristic jump from rest state to self-sustained oscillations [Fig. 31(b)] by increasing the pump energy in the absence of any input perturbation. For example, for a detuning of $\Delta\lambda = 1.5$ nm, the system self-pulses for pump power above ~2.9 mW [see bias of hysteresis plot in Fig. 28(e)]. The output pulse period and width depend on both the pump power and the detuning [Fig. 31(b)].

As is characteristic of an excitable system, the PC exhibits the classic refractory period [Fig. 32(a)]; i.e., the time the PC takes to return to its rest state (be ready) for the next input perturbation after it has spiked for the first perturbation. As explained before (see Section 3.1), this dead time is approximated as the minimum delay (Δt) between two perturbations that result in two consecutive responses. In this particular case, the refractory period is ~2 μs (cf. with the picosecond time scales of those gain-SA lasers in Section 3.1). Also, another interesting observation is the linear relationship between the refractory time and the excitable pulse duration [Fig. 32(b)] for different detunings. As Brunstein *et al.* [34] comment, further theoretical work would be necessary to understand this scaling.

Figure 31

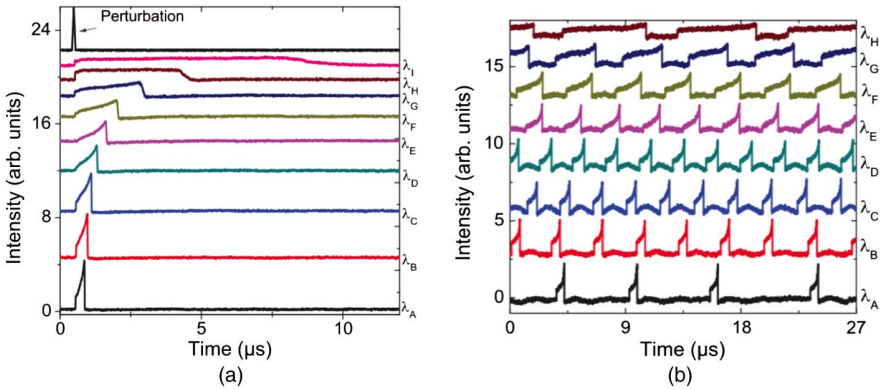

Transient responses (bottom traces) for different detunings. (a) The detunings (in nanometers) and the injected powers (in megawatts) are, from λ_A to λ_I, 1.8 and 2.9; 1.7 and 2.5; 1.6 and 2.2; 1.5 and 1.8; 1.4 and 1.6; 1.3 and 1.3; 1.2 and 1.2; 1.1 and 0.9; 1 and 0.8. The top trace corresponds to the perturbation signal (peak power = 80 μW). Figure 3 from http://link.aps.org/abstract/PRA/v85/p031803. (b) Self-sustained oscillations. Reflected signals as a function of time for different detunings, from λ_A to λ_H, 1.8, 1.7, 1.6, 1.5, 1.4, 1.3, 1.2, and 1.1 nm. The input power, measured at the tapered fiber input, is 3.2 mW. Reprinted with permission from Brunstein *et al.*, Phys. Rev. A **85**, 031803 (2012) [34]. Copyright 2012 by the American Physical Society. Figure 6 from http://link.aps.org/abstract/PRA/v85/p031803.

In summary, apart from the rich physics, the main motivation of exploring excitability within PCs is the fact that they could enable a system to be of a size of the order of the wavelength of light and consume only milliwatts of power [134], making them particularly attractive for large-scale all-optical integration. The nonlinear effects leading to bistable and excitable behavior can be either thermal or electronic. Yacomotti *et al.* [39] note that while optical bistability can be manifested by thermal effects that easily provide the nonlinear levels, its application to fast information processing is a bottleneck since the frequencies associated with thermal relaxation are typically in the megahertz range or even slower. However, electronic nonlinearities, limited by the carrier lifetime, allow faster switching, but the challenge is to isolate them from the thermal effects. Tanabe *et al.* [145] have demonstrated fast operation using a four-point-defect silicon 2DPC high-Q nanocavity in which the electrons are injected via two-photon absorption.

3.4. Resonant Tunneling Diode Photodetector and Laser Diode

An excitable optoelectronic device comprised of a double barrier quantum well (DBQW) resonant tunneling diode (RTD) photodetector driving a laser diode (LD) [Fig. 33(a)] ($\lambda = 1.55$ μm) has been demonstrated by Romeira *et al.* [45,46]. A DBQW-RTD consists of a low bandgap semiconductor layer (InGaAs; 6 nm wide QW) sandwiched between two thinner layers of higher bandgap material (AlAs; 2 nm wide barriers). This structure is inserted between low bandgap n-type material layers (typically the well material) to form Fermi seas of electrons. The fabricated RTDs [Fig. 33(a)] form a ridge waveguide of 4 μm width and 150 μm length [146]. The LD consists of an InGaAsP MQW active region operating in continuous-wave mode with 6 mA threshold current (>10 mW output optical power) and 0.8 V threshold voltage [Fig. 33(c)]. To form the neuromorphic primitive, the RTD photodetector and LD dies are connected in series through a 50 Ω microstrip transmission line on a printed circuit board.

Figure 32

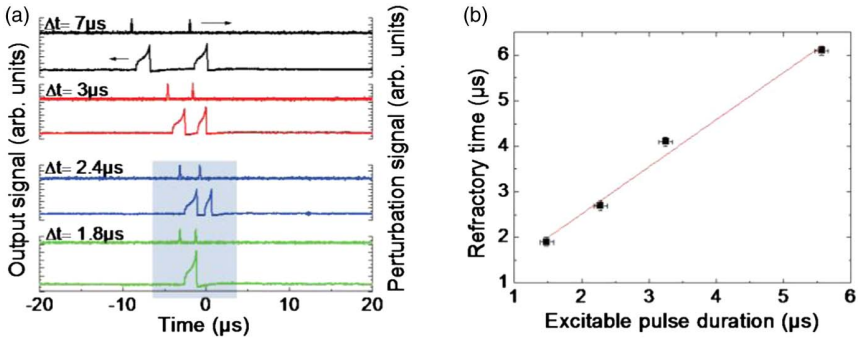

Refractory period test. (a) Output and perturbation signals (lower and upper traces) as a function of time for different delays (Δt) between 808 nm perturbation pulses; $\Delta\lambda = 1.2$ nm, injected power 2.8 mW, and perturbation power 255 μW. The refractory time is ∼2 μs, determined as Δt just before the two output pulses take place (in between the two highlighted situations). (b) Refractory time as a function of the excitable pulse duration ($\Delta\lambda = 1.2$, 1.1, 1, and 0.9 nm for increasing excitable pulse duration). Red line: linear fit. Reprinted with permission from Brunstein *et al.*, Phys. Rev. A **85**, 031803 (2012) [34]. Copyright 2012 by the American Physical Society. Figure 5 from http://link.aps.org/abstract/PRA/v85/p031803.

A unique feature of the RTD-LD is that it can be perturbed with an input signal (above threshold) either optically or electrically, emitting both optical and electrical pulses on a nanosecond time scale. For example, the RTD-LD can be electrically injected with signals V_{in}/V_{noise}, together with a bias control V_{dc}, and the electrical output V is measured across it. The DBQW-RTD typical room-temperature dc current–voltage (I–V) characteristic [Fig. 33(c)] has a pronounced negative differential resistance (NDR) region that arises due to nonlinear processes for transport of charges across the DBQW substructure.

For the study of neuron dynamics, interest in RTDs has been motivated by the observation of stochastic resonance in a noise-driven low-frequency bistable RTD [147]. RTDs have also been employed to implement compact cellular neural/nonlinear networks (CNNs) [148]. The RTD-LD can be operated in two separate regimes by exploiting its asymmetric nonlinear characteristics to emit either single pulses or a burst of pulses. When biased outside this region (I and III), RTDs can exhibit excitable characteristics [45,46] and also bistable behavior [147]; when biased in the NDR region (II), RTDs have been demonstrated as high-speed oscillators for terahertz generation [149].

Principle of operation: Classically, only particles that have sufficient kinetic energy can pass over a potential barrier, while particles with lower energy are reflected back. Quantum mechanics, on the other hand, allows a finite probability for particles with lower energy than the barrier height to tunnel through the barrier. Fundamentally, this concept is observed as resonant tunneling through double potential barriers [150]. Tunneling of charge carriers through the identical double barriers is strongly enhanced when their energy equals to one of the well energy levels, reaching much higher values

Figure 33

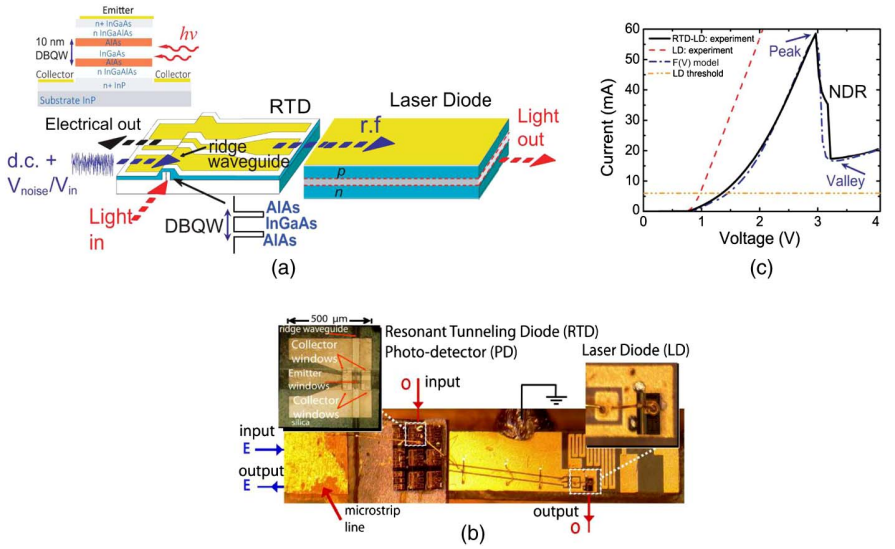

(a) Schematic of the RTD photodetector and LD semiconductor chips forming the RTD-LD excitable optoelectronic device. Inset is the cross section showing the epi-layer structure of the RTD. (b) Experimental I–V characteristics of LD, RTD-LD, and I–V model fit. (a) and (b) Reprinted with permission from [45]. Copyright 2013 Optical Society of America. (c) Photograph of the hybrid optoelectronic integrated circuit. Insets show the RTD and LD dies. Reprinted from Romeira *et al.*, Opt. Quantum Electron. **46**, 1391–1396 (2014) [46] with permission of Springer.

(complete tunneling transmission) than the product of the two individual barrier transmission coefficients at the energy values of the system resonant levels (Fig. 34) [151].

When a low voltage bias $V \ll V_p$ is applied to the device, a small current flows. The current comes from various mechanisms, such as nonresonant tunneling, thermionic emission over the barriers, a scattering-assisted tunneling process, and leakage current through the surface states, all of which contribute to the background current. Increasing the bias voltage raises the emitter relative to the resonant level in the well and gives a maximum current when the conduction band in the emitter region corresponds to the resonant level [Fig. 35(a)], resulting in the first positive differential resistance region (PDR). At this stage, more electrons are injected from the emitter region to the QW, and, therefore, a peak current I_p in the I–V characteristic is obtained [Fig. 35(b)]. Further increasing the voltage brings the resonant level below the emitter level and into the forbidden gap, where there are no longer carriers available to efficiently cross the DBQW. This results in significant reduction in current producing a NDR property in the I–V characteristic. At a given voltage $V_v \gg V_p$, the current reaches a local minimum I_v. An additional increase on the bias voltage will further lift up the emitter Fermi level, and tunneling through higher resonant levels or through the top regions of the barriers will lead to new current rise, similar to the classical diode I–V characteristic, resulting in a second PDR.

As detailed in Refs. [45,46], the dynamics of the system can be modeled with the single-mode laser rate equations describing the photon S and carrier numbers N of the LD coupled to the Liénard equation that dictates the current I and voltage V across the RTD-LD:

Figure 34

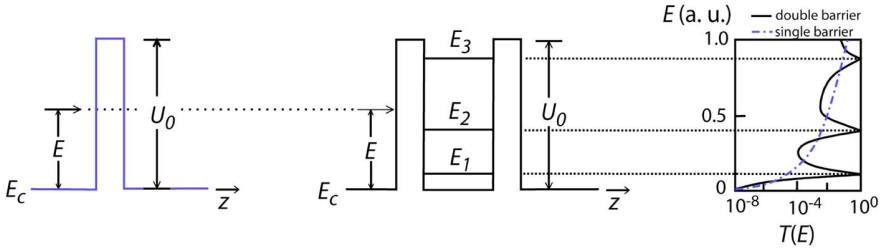

Transmission coefficients $T(E)$, of single (left) and double (center) barrier QW structures as a function of incident carrier energy E. Reprinted with permission from author [96].

Figure 35

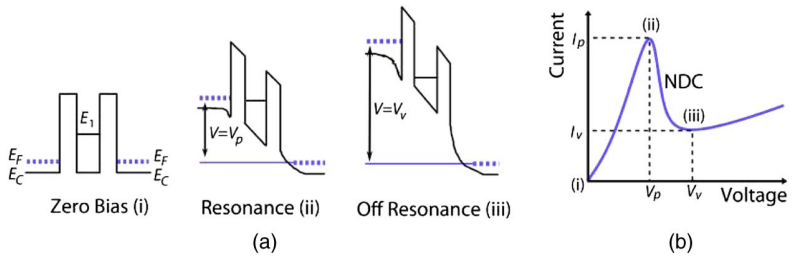

(a) Lowest conduction band profile under applied voltage. (b) Negative differential conductance current voltage characteristic. Reprinted with permission from author, [96].

$$\frac{dV}{dt} = \frac{1}{\mu}[I - f(V) - \chi\xi(t)], \tag{7a}$$

$$\frac{dI}{dt} = \mu[V_{dc} + V_{in}(t) - \gamma I - V], \tag{7b}$$

$$\frac{dN}{dt} = \frac{1}{\tau_n}\left[\frac{I}{I_{th}} - N - \left(\frac{N-\delta}{1-\delta}\right)(1-\varepsilon S)S\right], \tag{7c}$$

$$\frac{dS}{dt} = \frac{1}{\tau_p}\left[\left(\frac{N-\delta}{1-\delta}\right)(1-\varepsilon S)S - S + \beta N\right], \tag{7d}$$

where $V_{in}(t)$ is the electrical input, and V_{dc} is the bias voltage control. $\mu = V_0/I_0\sqrt{C/L}$ and $\gamma = R(I_0/V_0)$ are dimensionless parameters that describe the equivalent circuit parameters: capacitance C, inductance L, resistance R, and $V_0 = V_{dc} - V_{th}$, with V_{th} being the LD's voltage drop at threshold, I_{th} is the laser threshold current, $\delta = N_0/N_{th}$, where N_0 is the carrier density at transparency and N_{th} is the threshold carrier density, ε is the laser gain saturation term and β is the spontaneous emission contribution, τ_n and τ_p are the carrier and photon lifetimes, respectively, time is normalized to the resonant frequency of the LC tank as $\omega_0 = 1/\sqrt{LC}$ with $\tau = \omega_0 t$, ξ is delta-correlated Gaussian white noise with zero mean, and χ is the variance (strength) of the noise. The NDR region of the nonlinear I–V characteristic function $f(V)$ gives rise to the RTD-LD oscillations [152].

Excitability in a DBQW-RTD LD and spike-generating mechanism can be explained by viewing the I–V curve as an excitable orbit and decomposing it into four stages (Fig. 36). The first fast stage corresponds to a sudden rise of the voltage (black line) without variation of the current. The second stage consists of a slow decay of both V and I along the right part of the $f(V)$ nullcline (red line). Next, another fast stage corresponds to a voltage drop to the other side of the same nullcline (green dotted

Figure 36

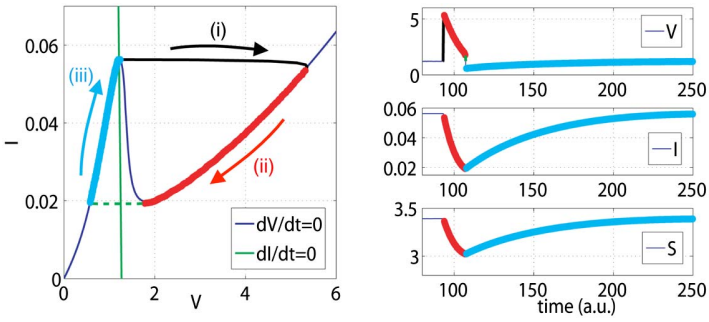

Decomposition of the excitable orbit into four stages. The first fast stage corresponds to a sudden rise of the voltage (black line) without variation of the current. The second stage consists of a slow decay of both V and I along the right part of the $f(V)$ nullcline (red line). Next, another fast stage corresponds to a voltage drop to the other side of the same nullcline (green dotted line) without variation of the current, finally followed by the last slow stage, where both V and I recover their initial values. Reprinted with permission [45]. Copyright 2013 Optical Society of America.

line) without variation of the current, followed by the last slow stage in which both V and I recover their initial values.

Results: The strongly asymmetric RTD-LD I–V characteristic leads to two very different excitable regimes. Spiking behavior is observed (Fig. 37) when the RTD is biased in the first PDR, slightly below the peak, as it responds to external perturbations by emitting excitable pulses when the perturbation exceeds a given threshold. The output pulses have identical intensity and shape with FWHM of ~200 ns, regardless of the input signals with varying profiles, amplitudes, and pulse widths, with V_{in} ranging from 100 to 450 mV, and pulse widths w from 100 to 200 ns.

When the system is driven by an electrical white Gaussian noise source, typical neuron-like pulse behavior is also observed [Fig. 38(a)]. Low noise strength results in pulse emissions as rare events [panels (i) and (ii)]; higher noise intensity results in pulses fired more easily [panels (iii) and (iv)]. The repetition time of these pulses approaches a refractory period of 500 ns, which is estimated from the histogram of the interspike interval (ISI) statistics [Fig. 38(c)] that depict the typical exponential behavior of a Kramer's escape process [153], displaced by the refractory time of the excitable orbits [45]; increasing the noise also results in a decrease in the tail of the distribution.

When the device is biased in the second PDR, the output temporal response consists of multi-spike bursts [(v) and (vi) in Fig. 38(a)]. The burst rate can be controlled by tuning the dc bias from the oscillation threshold. This is typical of the FitzHugh–Nagumo neuron model, a simplified version of the Hodgkin–Huxley model, where such a feature would be either absent or limited to a small parameter vicinity in the case of excitable systems with a symmetric nullcline. The experimental results are shown to be consistent with the simulation results [Figs. 38(b) and 38(d)].

In addition to the neural dynamics simulated above, this architecture may be amenable to a large-scale networking architecture, as described in Ref. [28]. The photodetector could allow for weighted addition of signals from LDs having unique wavelengths. This will be discussed in more detail in Section 4.

Figure 37

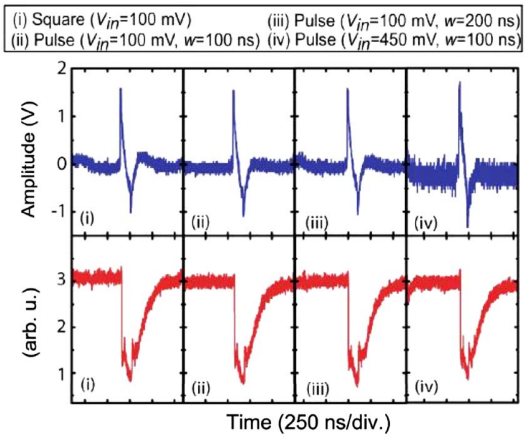

Excitable pulses in both the electrical (top; blue) and the optical (bottom; red) RTD-LD outputs triggered by either a square or a pulse input signal at $V_{\text{dc}} = 2.9$ V. Reprinted with permission from [45]. Copyright 2013 Optical Society of America.

In conclusion, RTD-LD-based excitable systems can be conducive to a wide range of low- or high-speed applications, as their excitable response can be easily tuned since the current–voltage N-shape of a RTD-LD is maintained almost from dc up to gigahertz frequencies. Potential applications for this device as pointed out by Romeira *et al.* [45] include reservoir computing, switching in optical networks, and neural emulation applications, such as associative memory or CNN-type computing architecture to perform complex information processing in neural inspired photonics networks.

3.5. Injection-Locked Semiconductor Lasers with Delayed Feedback

A free-running single-mode semiconductor laser outputs stationary, coherent, continuous-wave light at a current pump rate above the *lasing threshold*. Since semiconductor lasers are Class-B lasers—where the carrier lifetime is much larger than the photon cavity lifetime—perturbations to the current pump result in underdamped transient oscillations in the light intensity, ultimately settling to the new stable steady state. These oscillations can become self-sustained limit cycles under several kinds of external influences, such as pump modulation, optical injection, or external optical feedback. It has been suggested that such semiconductor lasers under coherent, single-mode optical injection from a so-called *master laser* are the ideal prototype for optical

Figure 38

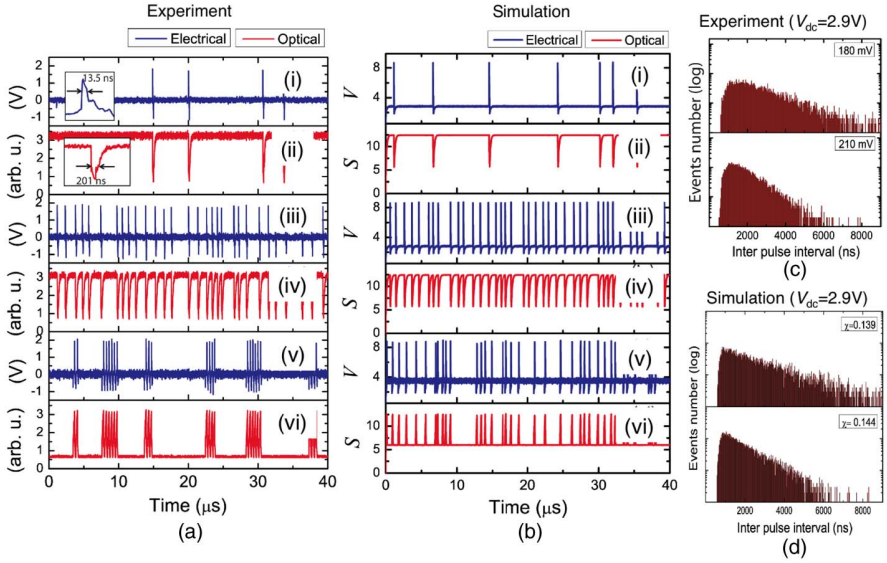

(a) Experimental and simulation time traces of electrical noise-induced neuron-like pulsing behavior in an RTD-LD excitable optoelectronic system in both the electrical and the optical domains. The RTD-LD is biased in the first PDR region ($V_{dc} = 2.9$ V) and modulated with noise strength of (i) and (ii) 100 mV; (iii) and (iv) 175 mV. Multipulsing bursts when the RTD-LD is biased in the second PDR region, $V_{dc} = 3.2$ V, and modulated with noise strength of 150 mV (v) and (vi). (b) Numerical simulation of voltage and photon density, (V, S) showing noise-induced pulsing dynamical regimes (i)–(iv) in the first PDR ($V_{dc} = 2.9$ V), and (v) and (vi) in the second PDR ($V_{dc} = 3.5$ V). The dimensionless noise strength employed in the simulations are: (i) and (ii) $\chi = 0.128$; (iii) and (iv) $\chi = 0.158$; and (v) and (vi) $\chi = 0.310$. Histogram of the ISI statistics of the laser output as a function of noise amplitude ($V_{dc} = 2.9$ V): (c) experiment; (d) simulation. Reprinted with permission from [45]. Copyright 2013 Optical Society of America.

excitability [154]. The idea is to perturb the phase of the injected beam, causing a 2π phase excursion in the cavity field of the *slave laser*. These phase kinks appear as discrete pulses in the circulating optical intensity. See Ref. [100] for a thorough report on the dynamical behavior of optically injected semiconductor lasers.

Barland *et al.* have shown one of the first experimental demonstrations of excitable behavior in a semiconductor optical amplifier (SOA) using optical injections [99]. They showed that the dynamics of the optical system could be mapped onto a generic FitzHugh–Nagumo model—a 2D simplification of the Hodgkin–Huxley model for spike dynamics in physiological neurons—yielding periodic pulsations of 10 s of kilohertz. Goulding *et al.* reported for the first time single and double excitable pulsations in a quantum-dot semiconductor laser under optical injection [40]. The dynamics of injection-locked lasers was thoroughly researched theoretically [43,91,100,155] and experimentally [92,102–104,156–159] (Sections 3.2 and 3.7).

Recently, Turconi *et al.* demonstrated controlled triggering of excitable pulses on an injection-locked VCSEL, an important milestone for processing applications with these systems [103]. We review numerical and experimental studies based on optically injected lasers in sections 3.2 and 3.7. In this section, we review recent work by Garbin *et al.* [29] that achieved control of excitability in optically injected lasers, which allowed them to feed output phase oscillations back into the slave laser after some delay, triggering a cascaded pulse response (Fig. 39). Hence, these oscillations were named addressable phase bits, and could be independently nucleated and annihilated at different points in the optical feedback loop.

Principle of operation: The experiment consists of a VCSEL (the *slave laser*) stably phase locked with a coherent light from an external master laser. The slave laser is pumped 6 times above threshold and the master laser frequency is set to 5 GHz lower than the slave laser frequency. The power of the injected beam is weak but sufficient to lock the phase of the cavity field to the external forcing. These parameters bring the

Figure 39

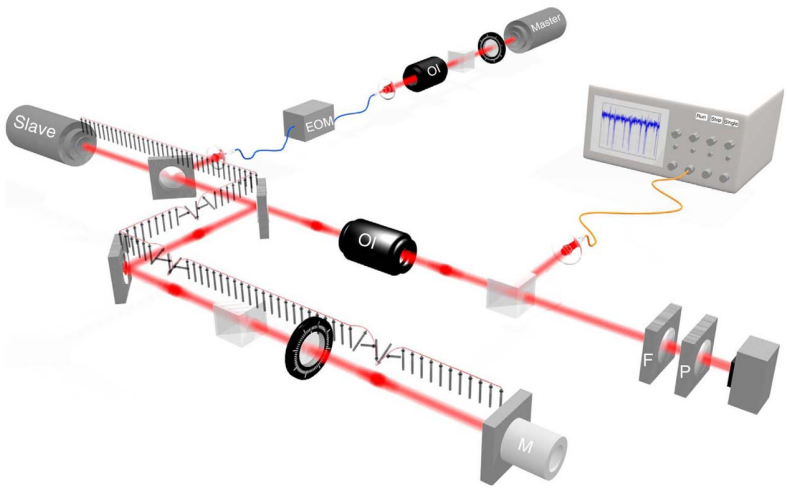

Experimental setup. The slave laser is submitted to optical injection by the master laser. Unidirectional coupling is ensured by an optical isolator (OI), and phase perturbations can be applied to the slave laser via the fiber-coupled electro-optic phase modulator (EOM). The arrows show a schematic view in the $\mathcal{R}(E)$, $\mathcal{I}(E)$ plane of several Φ-bits stored in the feedback loop. Reprinted by permission from Macmillan Publishers Ltd.: Garbin *et al.*, Nat. Commun. **6**, 5915 (2015) [29]. Copyright 2015.

system to the vicinity of a saddle node on a circle bifurcation. Physically, this means that the slave laser is locked but close to the unlocking transition [103]. Perturbations (<200 ps) applied to the injected beam via an electro-optic phase modulator cause the slave laser to emit an excitable pulse about 10%–25% of the dc value, depending on biasing.

Results: Garbin *et al.* reported that, in the presence of very weak optical feedback with adequate phase mismatch, the pulse fed back to the slave laser is regenerated after a very small delay time compared to the round-trip delay. Therefore, because the steady-state operation is periodic, they represent the output intensity as a *co-moving reference frame* in space-time (visualized in the transformations in Figs. 40(b) → 40(a) and 40(d) → 40(c)). The timing of the pulse slides to the right after each round trip, meaning that the pulse repetition rate is slightly less than the round-trip period. This is due to the regeneration delay in the dynamical response of the slave laser. It is said that a pulse is *nucleated* as a Φ-bit stored in the feedback path. Triggering a similar phase shift at other points within the 3 ns window can lead to multiple circulating pulses. Figure 40(c) illustrates the *creation* of a second Φ-bit within the period of the external cavity round-trip path.

In this setup, different Φ-bits can drift at different rates per round trip and reorganize (Fig. 41(a)); moreover, the Φ-bits tend to have a repelling force that spaces them out

Figure 40

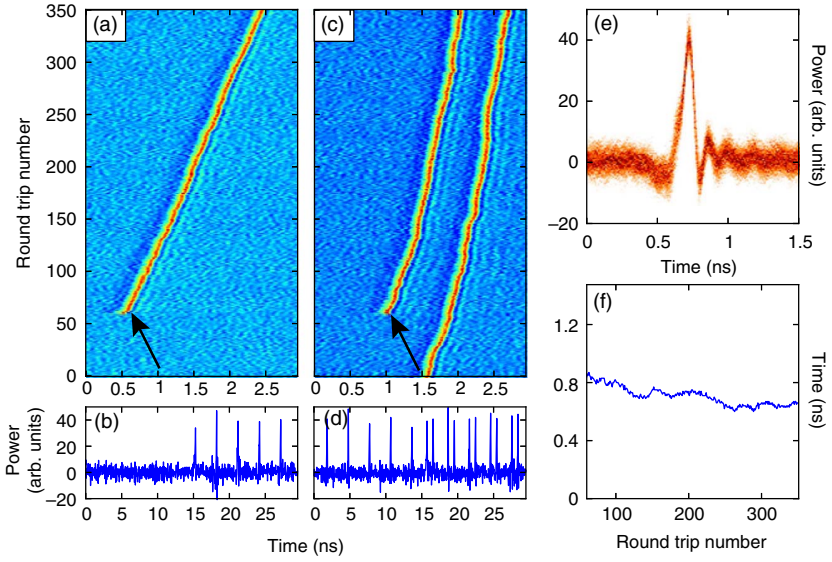

Nucleation of two Φ-bits in space–time representation. In panel a, a phase perturbation is applied (black arrow) while the system is in a stable stationary locked state. Following that perturbation, a pulse is nucleated and repeats with a periodicity close to the feedback delay time, as shown in panel b. The space–time representation is chosen such that the pulse is almost stationary (see text). After some time, a phase perturbation is applied again on the system (black arrow), with the first Φ-bit already stored. The two Φ-bits now propagate in the feedback loop, without perturbing each other (panels c and d). Panel e shows superposition of a single Φ-bit waveform over 350 round trips. The very well-defined shape indicates the attractor nature of the Φ-bit. The ringing following the pulse is attributed to the detection set-up. Panel f shows the evolution of the distance between the two pulses in the course of time. Reprinted by permission from Macmillan Publishers Ltd.: Garbin *et al.*, Nat. Commun. **6**, 5915 (2015) [29]. Copyright 2015.

evenly in time, ~790 ps (Fig. 41(b)). The opposite operation of nucleation, called *annihilation*, was also demonstrated (Fig. 41(c)). This was achieved by applying a phase perturbation precisely near the time of the desired Φ-bit. Figure 41(c) demonstrates storage of an 8-bit pattern in the feedback optical loop and addressable creation and annihilation of these bits. Although nucleation and annihilation were controlled by phase modulation, incoherently triggered nucleation has also been demonstrated with a different laser in Ref. [104].

Injection-locked lasers with long-delayed feedback possess a fascinating repertoire of spatially distributed dynamics, allowing them to access spatially localized nonlinear effects, such as solitons. Topological Φ-bits have attractive physical properties such as stability and addressability, and it is suggested that they are general to injection-locked lasers with delayed feedback. Applications could aim for information storage, pulse reshaping and phase discrimination in optical communication networks [29].

3.6. Semiconductor Lasers Subjected to Optical Feedback

Semiconductor lasers with a low facet reflectivity placed next to a reflecting surface outside the laser (active) cavity creates an external (passive) cavity where a fraction of the emitted light re-enters the laser cavity. The external feedback cavity has its own set

Figure 41

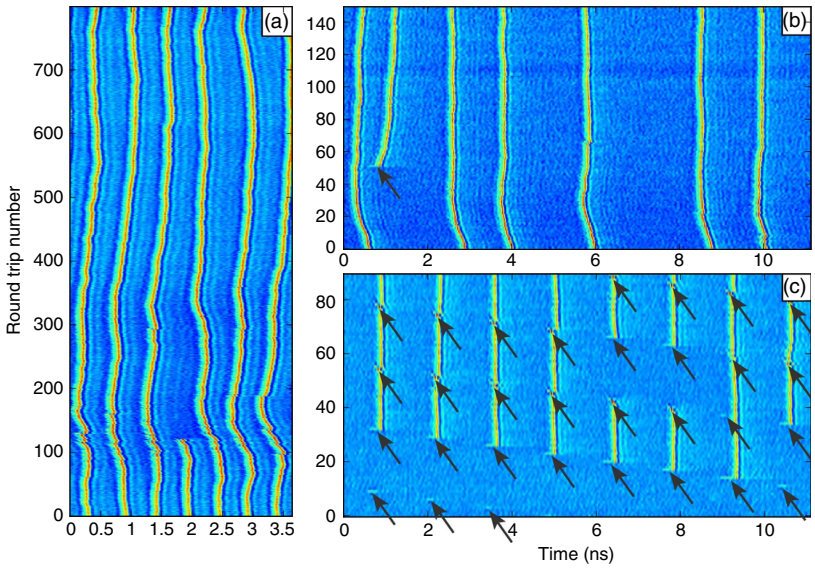

Control of Φ-bits. In panel (a), seven Φ-bits initially co-exist in the feedback loop. The six remaining bits reorganize in the course of time after cancellation of the central one. In panel (b), six Φ-bits are present in the feedback loop. A perturbation (black arrow) is applied and nucleates a seventh Φ-bit. The two nearest neighbors repel each other until they reach sufficient time separation (790 ps), but the other existing Φ-bits are not affected. In panel (c), many perturbations (black arrows) are applied successively in time and nucleate several Φ-bits starting from the homogeneous state. Existing Φ-bits can be canceled if they are hit by a phase perturbation, as shown at approximate coordinates (6; 40) and (8; 40). In this case, a nonmonotonic sequence of 13 different 8-bit integers has been stored. The same perturbation parameters are used for nucleation and cancellation. Note that the feedback loop is 3 times larger in panels (b) and (c) than in panel (a). Reprinted by permission from Macmillan Publishers Ltd.: Garbin *et al.*, Nat. Commun. **6**, 5915 (2015) [29]. Copyright 2015.

of longitudinal modes that compete with those of the laser cavity, each having its own resonances [160]. A whole set of external-cavity mode frequencies become available for lasing action (each with different stability properties [161]) as a consequence of changing the frequency of the semiconductor laser to accommodate external-cavity resonances by tuning the laser parameters (explained latter). Rich laser dynamics can be observed even with feedback levels of less than 0.01% or −40 dB [160]. Lasers based on optical feedback have been thoroughly investigated (numerically and experimentally) [105,160,162–164]. This has led to an interesting body of work on extremely short cavities (i.e., multisection devices with integrated cavity) that are excitable and Q-switched or *self-pulsing* [107–109,165,166]. The self-pulsing frequency of the laser can be locked to the round-trip frequency associated with the external cavity, resulting in the tunability of the repetition rate of the pulse train [160].

Principle of operation: Lang–Kobayashi equations [167] are typically used to model single-mode lasers that exhibit multistability and hysteresis phenomena when subjected to optical feedback from an external cavity. Wünsche *et al.* [109] fabricated a device similar to the one shown in Fig. 42, in which the feedback is strong and the external cavity belongs to the same waveguide ridge, thereby creating an integrated active–passive multisection cavity. The electric field inside this cavity therefore develops a spatiotemporal structure that has a sensitive phase dependence. Wünsche *et al.* [109] modeled this spatiotemporal structure with traveling-wave equations (TWEs) [Eq. (8a)]. The electric field is modeled by slowly varying amplitudes in counterpropagating directions: forward $\Psi_+(t,z)$ and backward $\Psi_-(t,z)$. These modes are coupled with each other by the coupling term $\kappa\Psi_{\mp}$, where κ is the real coupling coefficient of the DFB index grating. v_g is the photon group velocity, α_0 the waveguide loss, $\beta(t,z)$ is the instantaneous local propagation constant of the waveguide relative to the Bragg grating wavenumber $\beta_0 = \pi/\Lambda$, and $p_\pm(t,z)$ is a polarization contribution that corrects for gain dispersion (more details in Refs. [169,170]). In the passive section, which lacks gain dispersion, $p_\pm = 0$ and $\beta = \beta_p = 2\pi n_{\text{eff}} c/\lambda - \beta_0$. n_{eff} can be modulated by an injected current I_p via the plasma dispersion effect (a.k.a. carrier refraction effect). In the laser section, $p_\pm$ is modeled by Eq. (8b), the Fourier-transform of a Lorentzian frequency-dependent dielectric function with height

Figure 42

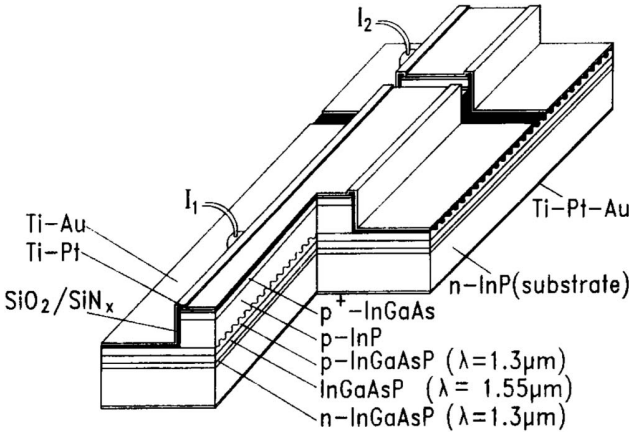

Schematic of a multisection ridge waveguide DFB laser with a phase tuning section. Note that this laser is a little different from the one presented in Ref. [109]. Copyright 1992 IEEE. Reprinted, with permission, from Mohrle *et al.*, IEEE Photon. Technol. Lett. **4**, 976–978 (1992) [168].

$2\gamma\tau_p$ and half-width $1/\tau_p$ centered at ω_g (see derivation in Ref. [169]). The nondispersive background propagation constant β is dynamically coupled to the average carrier density $N(t)$ [Eq. (8c)], which is, in turn, linked to the optical fields $\Psi_\pm$ via the rate equation [Eq. (8d)]. In the following equations, α_H, Henry factor; Γ, transverse confinement factor; g', differential gain; N_{tr}, transparency density; ϵ, gain saturation coefficient; I, injection current; V, volume of the active zone; τ, carrier lifetime; and $\langle\Psi,\Phi\rangle$, average of $\Psi_+^*\Phi_+ + \Psi_-^*\Phi_-$ over the laser section:

$$\left(-\frac{i}{v_g}\frac{\partial}{\partial t} \mp i\frac{\partial}{\partial z} + \beta - i\frac{\alpha_0}{2}\right)\Psi_\pm + \kappa\Psi_\mp = p_\pm, \tag{8a}$$

$$\frac{\partial}{\partial t}p_\pm = i\omega_g p_\pm - \frac{p_\pm}{\tau_p} - i\Gamma\gamma\Psi_\pm, \tag{8b}$$

$$\beta = \frac{1}{2}(\alpha_H + i)\frac{\Gamma g'[N - N_{\mathrm{tr}}]}{1 + \varepsilon\Gamma\langle\Psi,\Psi\rangle} - i\Gamma\gamma\tau_p, \tag{8c}$$

$$\frac{\partial N}{\partial t} = \frac{I}{eV} - \frac{N}{\tau} - 2v_g\,\mathrm{Im}[\langle\Psi,\beta\Psi\rangle - \langle\Psi,p\rangle]. \tag{8d}$$

These equations can be laid out using a compound cavity mode formalism, and with the *adiabatic* change approximation of the fields with respect to the carrier density, one can transform Eqs. (8a)–(8d) into a set of ordinary differential equations, which warrants a bifurcation analysis, which will now be discussed in detail.

Results: Shown in Fig. 42 is a typical two-section device—a single-mode laser with DFB supplemented by a passive phase section—in a Fabry–Perot resonator. Wünsche *et al.* [109] have investigated excitability in such a laser with a gain section that is 220 μm long emitting at 1536 nm, and a passive section of comparable length of 250 μm with a cleaved facet as an end mirror. The passive region bandgap (of 1300 nm) is at higher photon energies an thus avoids being pumped by the laser emission. The phase of the light fed back to the active region from the passive section can be tuned with carrier injection, i.e., the bias current I_p into the passive section. This allows for the study of interesting dynamics of the laser, i.e., the topology of the phase space. The optical phase shift $\varphi = 2\beta_p L_p$ is the bifurcation parameter (with $\beta_p = 2\pi n_{\mathrm{eff}} c/\lambda - \beta_o$), which is controlled by I_p via the effective refractive index n_{eff}.

Figure 43 depicts a steady-state solution for N as a function of φ for a particular set of laser parameters. Three distinct branches simultaneously exist over a span φ with three fixed points (solutions) between A and B: 1 (stable), 1′ (saddle), and 2 (stable). Branches 1 and 1′ belong to the same mode, whereas branch 2 belongs to a different mode, giving rise to hysteresis between points A and B. A stable limit cycle and a saddle-type limit cycle exist around A for some phase ranges. To the left of A ($\varphi < \pi$), these cycles annihilate in a fold bifurcation (see Section 2.3). Just right of A, at the point H ($\varphi = \pi$), the stable orbit vanishes in a homoclinic bifurcation with 1′. A projection of the phase space topology onto the density–intensity plane is shown as a phase space portrait in the inset of Fig. 43. As expected, the saddle-type periodic orbit encircles focus 2 and could either collapse onto 2 or 1′ depending on the direction of phase perturbation. The unstable manifold of saddle 1′ has two roots. One leads directly to focus 1 and the other leads to a large excursion around 2 before collapsing back to focus 1. The stable manifold of saddle of 1′ serves as a separatrix. Excitability

can occur if an external perturbation (dotted arrow) decreases N such that the system is brought to a phase loop (think solid line) going past the threshold, below the saddle, and the large excursion of its stable manifold on the way to focus 1 [109].

Wünsche *et al.* [109] tested their device by applying external perturbations with 35 ps pulses with a repetition rate of 15 MHz. Figure 44(a) shows the result for two levels of optical injection. Only smooth and rapidly damped relaxation oscillations are observed below a critical pulse energy of $P_0 \approx 3$ pJ. Just slightly increasing the optical input ($1.01P_0$) results in a dramatic change in the dynamic response of the laser, with the output being 1 order of magnitude higher than the average output. The inset illustrates this threshold or steplike behavior, which is the evidence of excitability. There is also weak dependence of the output response on the magnitude of the perturbation above threshold. These observations are corroborated with numerical simulations, as shown in Fig. 44(b). The significant amount of jitter at the output [Fig. 44(a)] is due to the phase space trajectory traversing on or close to the saddle point, resulting in a slowdown of the transient time of about 100 ps. There is also a noticeable excitation of a second pulse, which is possibly caused by the dip in the phase space trajectory [Fig. 44(b) inset]. The refractory period is measured to be

Figure 43

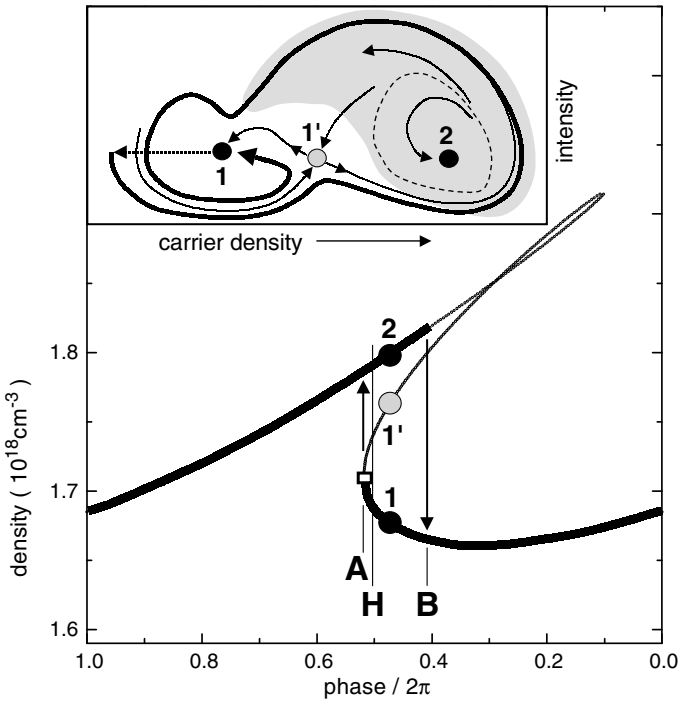

Plot of the carrier density of stationary states versus phase shift as calculated from Eqs. (8a)–(8d). Thick line: stable; thin line: unstable. Parameters: $v_g = c/3.8$, $\alpha_0 = 25\ \mathrm{cm}^{-1}$ (laser), $20\ \mathrm{cm}^{-1}$ (phase), $\kappa = 180\ \mathrm{cm}^{-1}$, $\Gamma = 0.3$, $g' = 5 \times 10^{-16}\ \mathrm{cm}^2$, $I = 50$ mA, $V = 9.9 \times 10^{-11}\ \mathrm{cm}^{-3}$, $\alpha_H = -5$, $\varepsilon = 0$, $N_{tr} = 1.3 \times 10^{18}\ \mathrm{cm}^{-3}$, $\tau = 1$ ns, 30% reflectivity of phase section, $\tau_p = 125$ fs, $\gamma = 2.6 \times 10^{15}\ \mathrm{cm}^{-1}\,\mathrm{s}^{-1}$, and ω_g at the long wave border of the stop band of the DFB section. Inset: phase space portrait; explanations are given in text. Reprinted with permission from Wunsche *et al.*, Phys. Rev. Lett. **88**, 023901 (2001) [109]. Copyright 2001 by the American Physical Society. Figure 1 from http://link.aps.org/abstract/PRL/v88/p023901.

around 0.3 ns, which is surprising as it is much smaller than the gain recovery time of 1 ns. Finally, the presence of a stable limit cycle is also confirmed by adjusting the phase current away from the excitability point where, the device switches to a self-pulsation mode.

In summary, the physics of semiconductor lasers with optical feedback can be of a highly complicated nature. However, from a dynamical system point of view, these lasers are of high interest. Optical feedback introduces a delay into the system which, in turn, induces a high dimensionality, resulting in rich behaviors, ranging from multi-stability, bursting, intermittency, low-frequency fluctuations, and fully developed chaos [171]. There are several applications that exploit the dynamics, including secure chaos communication and chaos key distribution, which are based on feedback-induced chaos [161,172,173]. Here, we limited the scope of this subsection to conventional QW lasers with feedback, but there is also an interesting body of work on quantum dot (QD) lasers subjected to feedback [22,40,102,174]. In general, QD lasers show a higher dynamical stability with respect to optical feedback than conventional QW lasers as a result of increased relaxation oscillation damping and a reduced phase–amplitude coupling [174]. In Section 4.1 we discuss a possible networking scheme to interconnect such lasers together.

3.7. Polarization Switching VCSELs

In this scheme, Hurtado *et al.* [41,44] employ a 1550 ns commercial VCSEL to emulate basic excitable functionalities by exploiting polarization switching and nonlinear dynamics [157–159] induced in the device under polarized optical injection. A wide range of dynamics can be observed, including bistability, limit oscillation [44], and

Figure 44

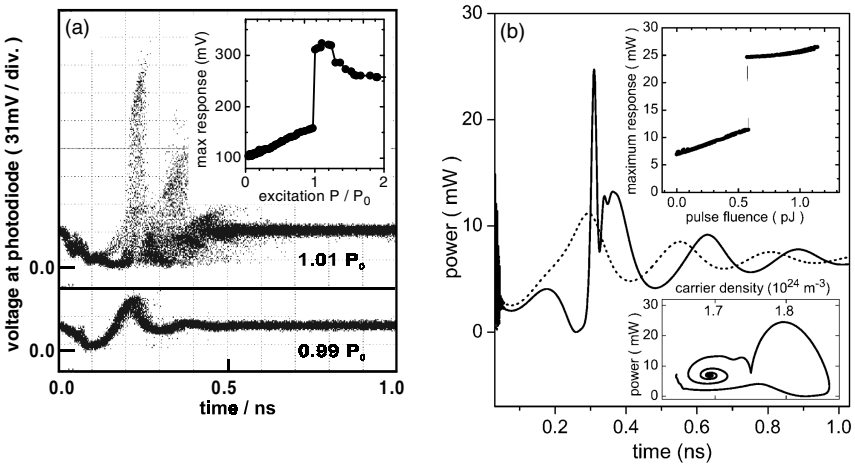

(a) Dynamic device response directly taken from the oscilloscope screen for two levels of optical injection. Inset: magnitude of the response peak versus strength of the optical excitation pulse. Figure 3 from http://link.aps.org/abstract/PRL/v88/p023901. (b) Dynamic response calculated for a situation corresponding to (a). Dotted line: $P = 0.54$ pJ; solid line: $P = 0.63$ pJ. Lower inset: phase space view of the solution after the end of the exciting impulse. Upper inset: spike intensity versus fluence P of optical input pulses. Parameter as in Fig. 43 except $\epsilon = 10^{-23}$ m^3. Reprinted with permission from Wunsche *et al.*, Phys. Rev. Lett. **88**, 023901 (2001) [109]. Copyright 2001 by the American Physical Society. Figure 4 from http://link.aps.org/abstract/PRL/v88/p023901.

excitability [175] by varying system parameters such as electric bias current, wavelength detuning between the externally injected signal and the resonant wavelengths of the VCSEL, and background input optical intensity. Note that a review of these neuro-computational properties of biological spiking neurons can be found in Ref. [71].

Principle of operation: The mathematical treatment of VCSEL dynamics must account for two competing modes' amplitude and phase (four variables), plus the carrier density and electron spin magnetization, which yield six coupled ODEs. Al-Seyab *et al.* [155] has mapped the different operational regimes of the VCSEL via the spin-flip model, giving insight into dynamics over the control parameter space: bias current, optical injection power, and optical injection frequency detuning. In one biasing condition, two orthogonal polarizations of the fundamental transverse mode (Fig. 45) of the emitted light is used to determine the VCSEL's state [41]. Without optical injection (rest state), only the parallel polarization contributes to the lasing mode, and the perpendicular polarized mode is suppressed. When increasing the external injection with the perpendicular polarized signal, the signal power of the parallel, lasing polarization decreases until hitting a threshold where the lasing polarization switches (Fig. 46). A subsequent input at the other polarization can switch the VCSEL back to its initial state. Biasing differently, one of these bistable states loses stability, resulting in limit-cycle behavior (Fig. 47). If input perturbations are then represented as dips in the holding beam intensity, then the VCSEL biased near this transition can respond in an excitable fashion (Fig. 48).

Results: The behavior of the mode competition in this laser is similar to the SRL discussed in Section 3.2a. With specific optical and electrical injection, the system can be placed in a regime where it exhibits either stability, bistability, or limit cycle dynamics, in which oscillation frequency changes with injected power [44]. The fast oscillations can be explained by beating between the VCSEL resonant mode and the injected signal: as the injection power is increased, the resonant wavelength is red-shifted, increasing the wavelength detuning and therefore increasing the beating frequency. In Ref. [175], the authors predicted excitability, obtaining a single spike in the laser output intensity after reducing the injected signal power by 1.4 dB for 0.5 ns. Figure 48(a) shows a single generated spike 4 dB above background output intensity, with a duration of ~0.1 ns. By varying the depth and width of the input perturbation, double and multiple spikes were also obtained [Figs. 48(b) and 48(c)]. Excitable behavior was then demonstrated in Ref. [38]. The rich dynamics presented by

Figure 45

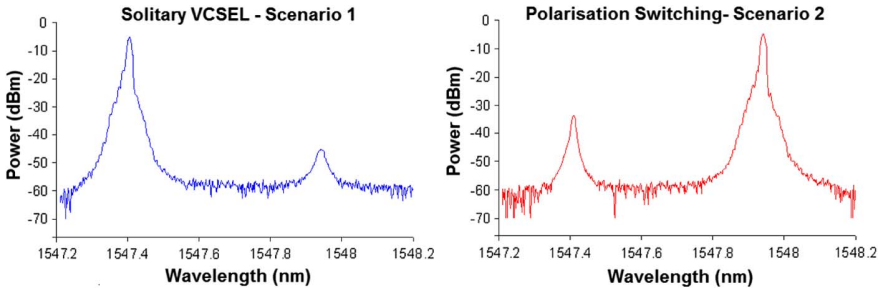

Optical spectrum of the 1550 nm VCSEL with and without orthogonally polarized optical injection producing polarization switching and injection locking. Reprinted with permission from Hurtado *et al.*, Appl. Phys. Lett. **100**, 103703 (2012) [44]. Copyright 2012 AIP Publishing LLC.

VCSELs at subnanosecond time scales are exciting for neuro-inspired photonic systems.

In conclusion, VCSEL technology is attractive owing to its many standard advantages [176], including low manufacturing cost, high-coupling efficiency to optical fibers,

Figure 46

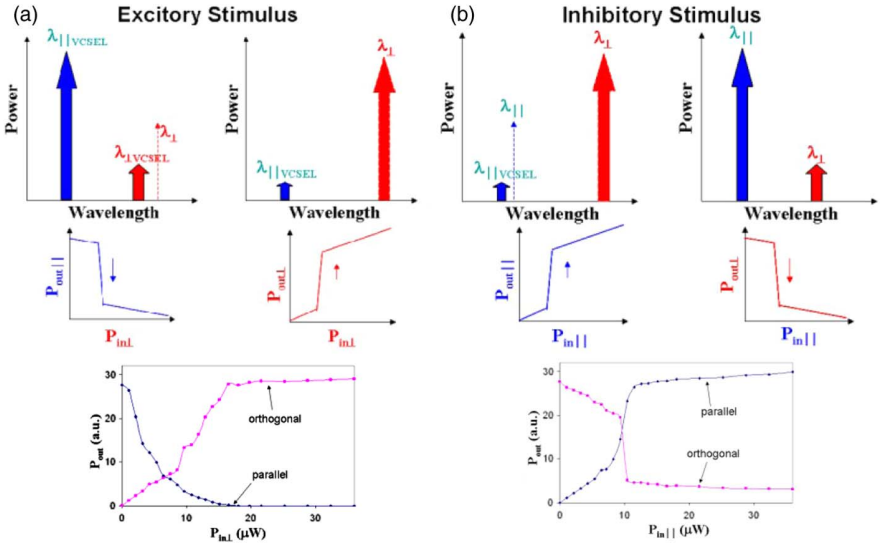

Operation principle of the VCSEL under (a) an excitatory and (b) an inhibitory stimulus. Bottom row: measured response of the VCSEL to (left) excitatory stimulus (orthogonally polarized signal; detuning $\lambda - \lambda_{\perp} = 0.02$ nm) and (right) inhibitory stimulus (parallel polarized signal; detuning $\lambda - \lambda_{||} = 0.02$ nm while the VCSEL is under the influence of an excitatory stimulus with power $P_{in\perp} = 15$ μW and detuning $\lambda - \lambda_{\perp} = 0$ nm). Reprinted with permission from [41]. Copyright 2010 Optical Society of America.

Figure 47

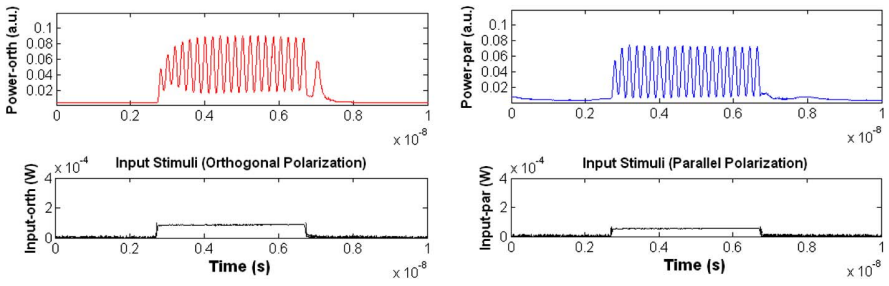

Response of the VCSEL to external stimuli (4 ns long), producing tonic spiking behavior. The lower row plots the time evolution and strength of the arriving stimuli. Left: orthogonally polarized time-varying injection into the solitary VCSEL ($I_{Bias} = 2.5I_{th}$, $\Delta\lambda_{\perp} = -0.04$ nm). Right: parallel-polarized time-varying injection into the VCSEL initially subject to CW orthogonally polarized injection into its orthogonal mode ($\Delta\lambda_{\perp} = 0$ nm) with a constant power of 20 μW ($I_{Bias} = 2.5I_{th}$, $\Delta\lambda_{||} = 0$ nm). Reprinted with permission from Hurtado *et al.*, Appl. Phys. Lett. **100**, 103703 (2012) [44]. Copyright 2012 AIP Publishing LLC.

single-mode operation, and low operating power. However, similar to the SRL proposal in Section 3.2a, this scheme results in a large base-level intensity on top of spikes. As argued in Ref. [35], a base-level intensity can potentially be debilitating by causing propagating system dependencies. Programming the synaptic weights w_{ij} to configure connection strength could interfere with attempts at parameter biasing. Although biological neurons also have a continuously varying state variable (voltage) during an action potential, the actual response is thresholded by voltage-gated reversal potentials that induce only neurotransmitter release between cells during a spike. It is unclear if the semispiking signals emitted by these other lasers could be processed effectively by subsequent units in a network. These lasers would probably require an optical thresholder or a nonlinear optical–electrical–optical (O/E/O) connection in addition to the units already proposed to work effectively. VCSELs offer an ease of compact integration into 2D and possibly 3D arrays; however, any approach based on optical injection faces other challenges in constructing a scalable interconnect platform. This will be discussed with more detail in Section 4.

4. TOWARD A PHOTONIC NEURAL NETWORK

Recent developments in CMOS-compatible photonic manufacturing could enable large-scale integrated photonic systems [177]. While the demand for this technology is primarily driven by communication needs in multicore CPU systems, it also opens a new door for unconventional photonic processing, including large networks of dynamical laser elements. As suggested in Section 2.2, a spiking neuron is a processing node only in the context of a spiking neural network; the synaptic connections are as important to the task of network processing as the dynamical neural behavior of individual nodes.

In a neural network model with N nodes, there are potentially N^2 possible connections between each node. This is called an *all-to-all* connected network, and is the limiting case for full network reconfigurability. Typically, the multiplicative strength of each connection—represented via a *weight*w_{ij} that determines the connection strength between nodes i to j—can be reconfigured to program the network to perform a desired task. Requiring an individual waveguide for each connection can limit network size since waveguide count scales quadratically with the number of nodes. Although fixed network topologies can be designed to avoid this [see Fig. 49(a)], a multiplexing

Figure 48

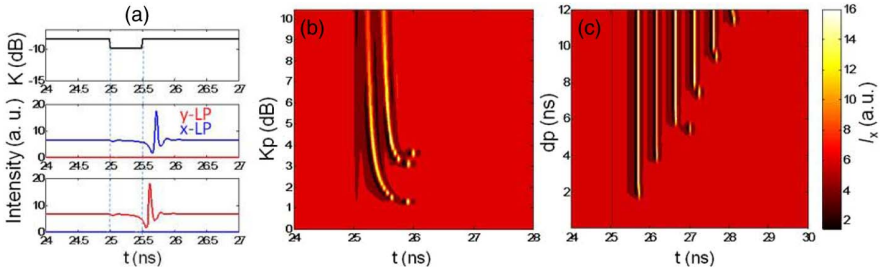

(a) Time traces of optical input with negative perturbation (top) and VCSEL output for the cases of orthogonal (middle) and parallel polarized injection (bottom). (b) Output intensity traces over a range of perturbation strengths, K_p, with duration, d_p, fixed at 0.5 ns. (c) Output intensity traces over a range of perturbation durations with K_p fixed at 1.4 dB. Copyright 2014 IEEE. Reprinted, with permission, from Al-Seyab *et al.*, in IEEE Proceedings of Semiconductor Laser Conference (ISLC) (2014), pp. 165–166 [175].

approach is necessary for a fully reconfigurable network. Time division multiplexing (TDM) has been exploited to form several types of optical reservoir computing systems [23,25,26]; however, the asynchronous timing of information in spiking approaches make this practically difficult for excitable lasers. Wavelength division multiplexing (WDM) represents a promising approach for on-chip network scalability and has been explored in an architecture by Tait *et al.* [28] called *broadcast-and-weight* (B&W) [Fig. 49(c)].

In this section, we propose two optical interconnect approaches that may be applied to different sets of excitable laser models and consider a networking approach proposed in Ref. [28]. Trade-offs are considered between various injection techniques, and the requirements of network nodes that perform both the excitable processing functions and signal conditioning properties necessary for interfacing with a network will be discussed.

4.1. Comparison of Injection Techniques

Excitability in some of the proposed devices (Sections 3.2 and 3.7) rely on direct optical injection to a laser cavity; others (Sections 3.1 and 3.4), on current injection. In a networking context, we will classify injection approaches into the following three categories as in Fig. 10: coherent optical injection models in which inputs directly interact with the cavity intensity [Fig. 10(a)], incoherent optical injection models in which inputs modulate an intracavity element or internal property of the cavity [Fig. 10(b)], and electrical injection models that use external O/E converters to electrically modulate a cavity section [Fig. 10(c)].

Coherent injection models are characterized by input signals directly interacting with cavity modes, such that outputs are at the same wavelength as inputs [34,91,94,104,105]. Coherent systems could potentially operate with bandwidths dictated by cavity Q factor, where $\tau = 2Q/\omega_0$. Cavity photon lifetimes can be brought down to several picoseconds or lower simply by decreasing cavity Q. These models typically include fewer electronic components; they may be all-optical devices that

Figure 49

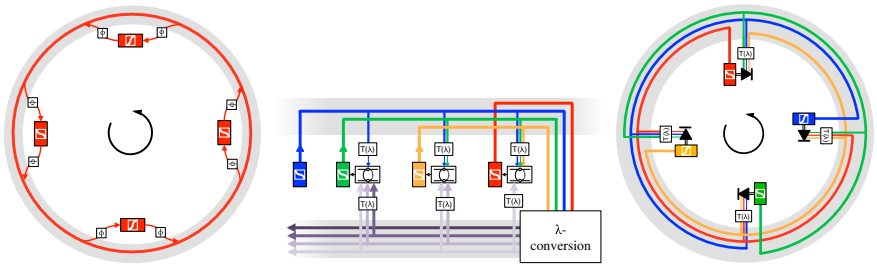

Concept diagrams of proposed interconnect architectures. Colored boxes represent laser devices with nonlinearities, with each color representing a different wavelength. Add–drop filters and couplers are omitted for simplicity. (a) Networking is possible in all-coherent models, but phase must be tightly controlled. A ring architecture with limited reconfigurability is shown here. (b) Noncoherent injection approaches can often accept a range of input signals at different wavelengths. Nonetheless, current models (i.e., with optically pumped inputs) require wavelength conversion for full, recurrent reconfigurability. (c) B&W network using electrical injection. Tunable filters $T(\lambda)$ allow for full N^2 degrees of tunability for N nodes, at the cost of electrical parasitics in the primary signal pathway.

rely strictly on all-optical nonlinear effects [101,142]. Since coherent optical systems typically operate at a single wavelength λ, output signals lack distinguishability from one another, which can limit reconfigurability. As suggested in Ref. [94] (Fig. 24), optical phase could be used to create additive or subtractive signals, although this means the optical phases in the network must be carefully controlled (i.e., all lasers synchronized). Nonetheless, this does not preclude the creation of globally coherent systems operating at a single wavelength. A highly coupled system for use in optical reservoir computing is shown in Fig. 49(a). A more reconfigurable interconnect may also be possible through a spatially multiplexed Mach–Zehnder grid architecture, similar in geometry to [178].

A second set of laser injection models use light in an input mode at λ_{in} to selectively modulate an intracavity property, which can trigger excitable output pulses in an output mode at λ_{out}. A number of approaches [35,37,38,89]—including those based on optical *pumping*—fall under this category. Output wavelength has a constrained relationship with input wavelengths, although it is not necessarily the same. The bandwidth of the approach is primarily limited by the speed of the intracavity property that is modulated. For example, the models in Refs. [35,37,89], which are based on carrier modulation, are limited by the carrier relaxation time. Selective intracavity modulation requires specialized resonator structures or injection techniques, which allow for inputs and outputs at different cavity modes. Although a variety of these models can accept inputs over a range of different wavelengths, they include many limitations in this regard. For example, in optical pumping approaches, since an optical pumping source must always be at a higher frequency (shorter wavelength) than the lasing frequency, the output wavelength of an optically pumped laser must always be longer than that of its input signals ($\lambda_{in} < \lambda_{out}$). At the same time, approaches with distinct optical pumping and injection can avoid this specific constraint. A full WDM-based networking approach would not be possible without the extensive use of wavelength conversion devices, which may limit system bandwidth, or may be difficult to fabricate easily [179,180]. Nonetheless, a future approach (i.e., based on the Kerr effect) may alleviate some of these limitations. A schematic of a noncoherent optical network is shown in Fig. 49(b).

Another group of models are based on electrical injection. Input signals at wavelength $\vec{\lambda}_{in} = \lambda_1, \lambda_2, \lambda_3 \ldots$ are incident on photodetector(s), which convert the optical signal into the electrical domain. This electrical signal, in turn, drives an intracavity element, which can result in the emission of an output optical pulse at λ_{out}. Several models rely on this optoelectronic technique, including those described in Refs. [47] and [45]. A demonstration of this approach is described in the next section. It is highly compatible with a WDM-based network scheme since there are no restrictions between the wavelengths of input(s) $\vec{\lambda}_{in}$ and output λ_{out} signals, as shown in Fig. 49(c). It is also the most straightforward to implement on planar photonic integrated circuit (PIC) platforms, requiring only a modification to the metallization layer for electrical injection. However, this approach could introduce bandwidth limitations: it is the only model described here limited by electrical device parasitics [47]. Device dimensions must therefore be carefully optimized to minimize RC parasitics, and signal bandwidths will be capped at ~20–40 GHz for even highly optimized device structures. Nonetheless, this class of devices maintains the highest compatibility with a wavelength-based networking scheme, and is the model analyzed in the B&W protocol [28].

4.2. Processing Network Node

Here, we will focus on a single network node that is compatible with the B&W protocol, an important step toward larger scale laser neural networks. As discussed in

Section 4.1, the available networking approaches depend largely on the injection properties of the laser device. B&W exhibits considerable reconfigurability and topological layout freedom, and to the authors' knowledge, is the only large-scale semiconductor laser networking scheme that has received considerable exploration and analysis [28,181,182,183].

A photodetector used to electrically drive an adjacent laser can also receive multiple WDM optical inputs, independent of the optical properties of a laser cavity. Because a broadcast waveguide provides full access at a single point, filters can be grouped together locally on the front end of each laser neuron. This is in contrast to grid or mesh networks [13,184] that are typically seen in other neuromorphic implementations, in which tunable connections are tied closely with network layout. This gives rise to the concept of a *processing network node* (PNN), which includes an excitable laser, detector, and spectral filter in a fully functional node, as shown in Fig. 50. This section will explore the definition of a PNN in a B&W context, and includes an experimental demonstration of the concept in a semiconductor laser platform.

A PNN is an interface that gives the ability for one laser neuron to communicate with others in a network. In a biological neural network, the complicated structure of physical wires (i.e., axons) connecting neurons largely determines the network interconnectivity pattern, so the role of neurons is predominantly computational. The contrasting all-to-all nature of optical broadcast in the B&W protocol saddles the photonic neuron primitive units with additional responsibilities of network control (routing, wavelength conversion, WDM signal generation, etc.). The PNN is the simplest set of photonic devices to perform the dual set of roles for spike processing and networking in a lumped subcircuit. Overall, a PNN can be created via an unconventional

Figure 50

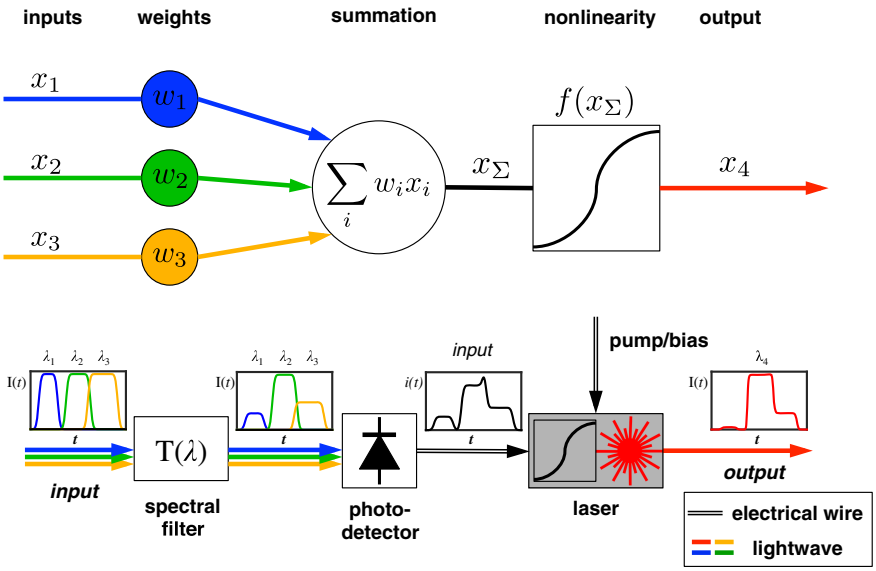

Top: depiction of a single unit neural network model. Inputs x_1, x_2, x_3 are weighted and summed. The result $x_\Sigma = \sum_i w_i x_i$ experiences a nonlinear function $y = f(x_\Sigma)$. Bottom: schematic of the laser neuron. A WDM signal is incident on a bank of filters, which apply a series of weights. The photodetector applies a summation operation, which drives an excitable laser with a current signal. The resulting laser outputs at a specified wavelength. Reprinted with permission from Nahmias *et al.*, Appl. Phys. Lett. **108**, 151106 (2016) [185]. Copyright 2016 AIP Publishing LLC.

repurposing of conventional optoelectronic devices, with potential to generalize to existing and prospective photonic platforms.

A processing network node is defined by the following criteria.

1. Weighting: the ability to configure and reconfigure the strength of influence that each spiking laser element has on other elements.
2. Fan-in: the ability to linearly combine weighted signals from many sources into a single physical variable, which can then modulate a spiking element.
3. Spiking dynamics: as listed in Section 2.2, integration, thresholding, reset/refractoriness, and clean pulse generation. Spiking dynamics observed in photonic devices have been reviewed in Section 3.
4. Cascadable output generation: the ability of one laser element to produce signals that are physically capable of modulating several other elements; this includes sufficient power and the correct wavelength.

Tunable weighting is an essential part of any conception of a neural-network-based system, through which a tremendous variety of different tasks can be performed. Tunability within individual processing elements (e.g., laser bias control) is also useful for some processing tasks; however, node tunability does not control the topology of the network. Therefore, the ability to tune the weights of many input signals and fan-in (i.e., many-to-one coupling) are both defining qualities of neural networks. Combining multiple signals from many sources within a processing network allows the overall distributed system to be radically more complex than its constituent elements.

An important issue to consider is cascadability, a property that must be exhibited by every node. Cascadable output generation encompasses some logical notions covered by spiking (e.g., logic-level restoration), but also includes physical requirements (e.g., wavelength and power). The output of a laser neuron must be more energetic than inputs in order to drive other stages. It also must be at a wavelength suitable to drive other elements, so, for example, a pump–probe-output-type device using four-wave mixing must incorporate additional wavelength conversion steps between the output wavelength and probe wavelength. The PNN model solves the wavelength cascadability issue by performing fan-in and modulation tasks in the electronic domain to curtail any propagation of noise in optical variables further than a single stage.

As mentioned in Section 4.1, cascadability and fan-in can be overcome by a B&W networking architecture [28] involving WDM and O/E/O conversion (see Fig. 50). Weighting is possible via passive spectral filters. The multiwavelength signal is summed via O/E conversion by photodetectors. The generated photocurrent directly modulates an excitable laser (E/O conversion), regenerating the output in the optical domain. Because all inputs and outputs are wavelength-multiplexed, all signals can coexist in a single broadcast waveguide, allowing for multiple virtual connections to exist. Nahmias *et al.* [47] proposed such a structure that met these conditions and also explored the physics of the O/E/O conversion.

An instantiation of a PNN has been proposed by Tait *et al.* [28]. It consists of spectral filter banks, a balanced photodetector, and an electrically driven excitable laser (Fig. 51). The two spectral filter banks are designated to be excitatory and inhibitory, depending on which of the photodetectors is activated in the balanced pair. Analog excitatory and inhibitory photocurrents are subtracted passively by a push–pull wire junction. The net photocurrent conducts over a short wire to modulate the laser gain section. This scheme is necessary to provide complementary weighting at the laser front end. Microring resonators are good candidates for the spectral filters due to their compactness, ease of tuning, and WDM compatibility. The use of microrings as

continuous-valued weights has recently been shown [181], and channel density limitations have recently been explored [183].

The PNN receiving principle has also recently been demonstrated in a III–V semiconductor platform [185], but with a continuous-wave laser. Two key functions are shown: WDM summation and an analog photodetector-to-laser O/E/O current link. For this demonstration, active devices were fabricated using a standard AlGaInAs MQW epitaxial structure on indium phosphide, designed to operate in the optical C-band. Samples were mounted on submounts with oxide and metallization layers, followed by an aluminum wire bond between the two devices, as shown in Fig. 52(b). Since the laser and PD shared the same top contact, proper biasing required that separate ground pads rest under each component. A positive bias ($V_b = 3$ V) on the photodetector pad ensured reverse-bias operation in the PD and counteraction of the forward pump current of the laser (85–95 mA) traveling across the wire bond junction. This biasing configuration, in addition to allowing the PD and laser to share the same top contact, ensured that the photocurrent signal traveled directly into the laser.

As shown in Figs. 53(i) and 53(ii), a hybrid electronic–laser device can receive signals from different wavelength channels simultaneously. The output of the laser is a simple bandwidth-limited sum of inputs. The laser nonlinear model is a simple threshold function (i.e., a perceptron), made possible through the laser's L-I curve. Pulse coincidence between the two channels (occurring around 43 ns) results in a larger amplitude, a demonstration of signal summation of multiple wavelength channels. Linear summation occurs as a result of the device being biased within the linear region of the L-I curve (Fig. 53, right). Since the L-I curve includes a saturation region at both small and large input amplitudes, a network of these units can in principle approximate any function [186] or simulate any dynamical system [187].

There are many aspects of the first PNN demonstration that can be improved. The bandwidth of the device (~250 MHz) is limited primarily by the photodetector in this demonstration. Although the metal bridge has an associated capacitance, simulations based on an equivalent circuit model suggest that the bandwidth is limited by device parasitics, which can be improved by shrinking the contact pads or size of

Figure 51

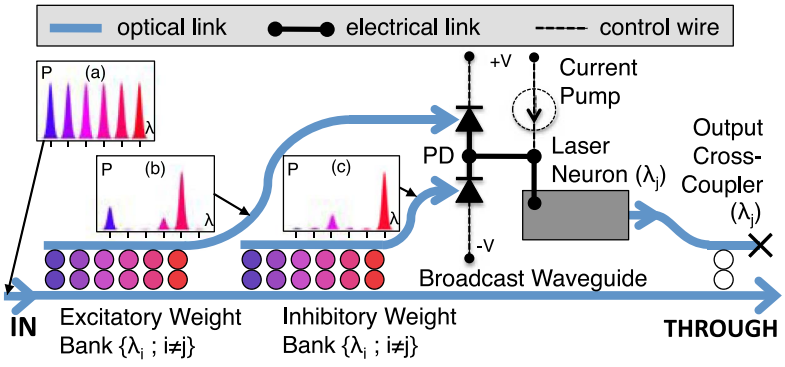

Possible physical implementation of a PNN. In this configuration, excitatory and inhibitory weight banks—which are created using a series of microring filters—directly interface with a broadcast waveguide. The resulting signal is incident on a balanced photodetector, which drives a laser to produce an output. The output is subsequently coupled back into the broadcast ring. Reprinted from [28]. Copyright 2014 Optical Society of America.

devices. The bandwidth can be >10 GHz with optimized device geometries for this structure, as explored in Ref. [47]. Top-side ground pads would allow the PD-laser system to be printed monolithically to avoid the need for a wire bond. Although the

Figure 52

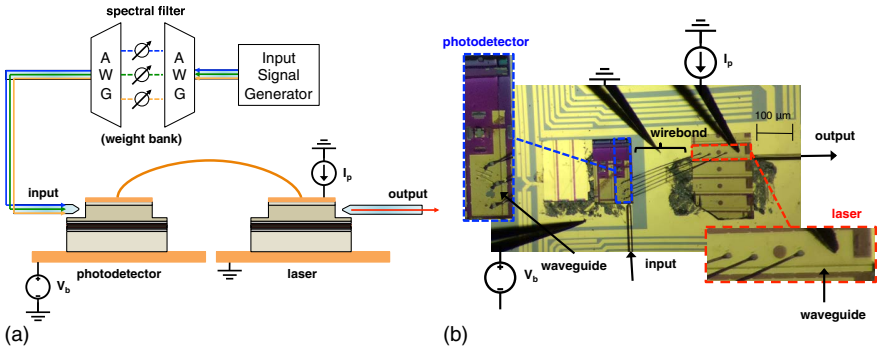

(a) Experimental setup, mirroring the basic processing node schematic (Fig. 50). Generated input signals experience different weights through a series of variable attenuators nested between two arrayed waveguide gratings (AWGs). The WDM signal travels into the PD, which current modulates an adjacent laser. The laser output is subsequently measured on a sampling scope. (b) Picture of a fabricated device, taken under a microscope. Active InGaAlAs devices are mounted on separate grounding pads, fabricated on a silicon submount. The top (P-side) of the PD is connected directly to the top (P-side) of the laser with aluminum wire bonds. With proper biasing ($V_b = 3$ V, $I_p = 85 - 95$ mA), optical inputs are converted to current signals, which a directly modulated laser converts back to an optical signal representing a thresholded version of the weighted sum. Reprinted with permission from Nahmias *et al.*, Appl. Phys. Lett. **108**, 151106 (2016) [185]. Copyright 2016 AIP Publishing LLC.

Figure 53

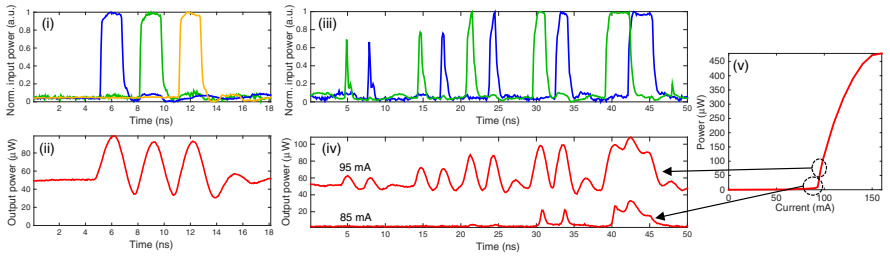

Left: demonstration of multichannel summation. (i) Normalized temporal pulse profiles of three independent wavelength channels (1538, 1543, and 1548 nm) traveling into the photodetector. (ii) The resulting output of the laser when biased at 95 mA. Right: demonstration of summation and thresholding. (iii) Inputs to the device, which includes two wavelength channels (1538 and 1543 nm). (iv) Output of laser biased below and above the lasing threshold. The laser can operate in both linear (95 mA) and nonlinear (85 mA) modes by using different regions of the L-I curve. If operated below threshold, the laser suppresses low-level signals, performing a key nonlinear operation necessary for processor cascadability. (v) The corresponding areas of the L-I curve used by the laser during operation. Reprinted with permission from Nahmias *et al.* App. Phys. Lett. **108**, 151106 (2016) [185]. Copyright 2016 AIP Publishing LLC.

laser acts with a simple feedforward nonlinearity in this demonstration, the PD-laser driving concept is compatible with the inclusion of more complex dynamics (i.e., spiking), which leads to better power cascadability, explored in Ref. [47]. Finally, the filter bank can be integrated together with the laser to form a full PNN.

The B&W protocol is one established method to create scalable networks of excitable lasers. In addition to allowing for dense connectivity, it permits hierarchical, feedforward, or recurrent network organization through the use of interfacial nodes that join one broadcast waveguide to another [28]. Nonetheless, as larger B&W systems are created, more practical challenges are faced. Creating a large circuit of laser devices, such as excitable lasers, would require both active and passive capabilities, yet co-integrating disparate optical materials (e.g., InGaAsP and Si) is a difficult challenge in photonic integration. Fabrication processes combining III–V and silicon represent an active area of research, expected to become more widespread as demand for integrated photonic systems grows [188,189]. Networking architectures compatible with excitable lasers could be a promising route to large-scale recurrent spiking neural networks in a photonic platform.

5. SUMMARY AND DISCUSSION

Over the past several years, there has been a deeply committed exploration of unconventional computing techniques—neuromorphic engineering. The idea is to build machines employing basic nervous system operations by bridging the physics of biology with engineering platforms enhancing performance for applications interacting with natural environments, such as vision and speech [4]. Neuromorphic engineering aims to alleviate the device level and system/architectural level challenges faced by conventional computing platforms. At the device level, digital CMOS is reaching physical limits [190]. Computational power efficiency for biological systems is around 1 aJ per multiply-accumulate (MAC) operation [4], which is 8 orders of magnitude higher (better) than the power efficiency wall for digital computation, which is 100 pJ/MAC [191]. There is a growing gap between the efficiency wall (supply) and the next generation application need (demand). Neuromorphic engineering is thus going through a very exciting period as it promises to make processors that use low energies while integrating massive amounts of information. At the architectural level, in von Neumann machines, memory and data interaction bandwidths greatly constrain the types of informatic systems that are feasible to simulate. In contrast, neuromorphic systems that allow communication, computation, and memory are co-located throughout the architecture. These neural-inspired systems are typified by a set of computational principles, including hybrid analog–digital signal representations, co-location of memory and processing, unsupervised statistical learning, and distributed representations of information.

Research in integrated photonic platforms (as an alternative to microelectronic approaches) has followed suit with the rapid development of CMOS-compatible photonic interconnect technologies. This has inadvertently opened a door for unconventional circuit and system opportunities in optics. In the past, the communication potential of optical interconnects (bandwidth, energy use, electrical isolation) have received attention for neural networking; however, attempts to realize holographic or matrix-vector multiplication systems have failed to outperform mainstream electronics at relevant problems in computing, which can largely be attributed to their incompatibility with integration and manufacturing. In contrast, techniques in silicon photonic PIC fabrication are driven by a tremendous demand for optical interconnects within conventional digital computing systems [177,192]. The first platforms for systems integration of active photonics are becoming commercial reality [188,189,193–195], and promise to bring the economies of integrated circuit manufacturing to optical systems.

Using a device set designed for data communication links (waveguides, filters, detectors, etc.), some have realized PICs for analog signal processing [196]. The potential of modern PIC platforms to enable large-scale all-optical systems for unconventional and/or analog computing has not yet been investigated.

Recent years have seen the emergence of a new class of optical devices that exploit a dynamical isomorphism between semiconductor photocarriers and neuron biophysics. Taking advantage of the ephemeral dynamics in photonic systems such as those in lasers allow these "photonic (laser) neurons" to exhibit spiking behavior on the picosecond or nanosecond (instead of millisecond) time scales observed in biological neurons [24,27,29–31,33,35–39,47]. Spiking is closely related to a dynamical system property called excitability, which is shared by certain kinds of laser devices. Excitable laser systems have been studied in the context of spike processing, with the tools of bifurcation theory, and experimentally, with some specifically designed for compatibility with silicon photonic PIC platforms [47]. These excitable lasers are amenable to a variety of different interconnection schemes. VCSELs occupy small footprints and can be fabricated in large arrays, allowing for massive scalability and low power use [176]. They can send signals upward to form 3D interconnects [197], can emit downward into an interconnection layer via grating couplers [198], or connect monolithically through intracavity holographic gratings [199]. DFB lasers, in contrast, can emit light in the planar direction. Although they occupy larger spatial footprints than their VCSEL counterparts (and have lower wall plug efficiencies, so use more power), their natural affinity for waveguide coupling and lithographically defined operating wavelengths post-growth them a strong candidate for integrating photonic neural networks on a single chip. DFB lasers can be coupled into passive waveguides in III–V materials, can butt-couple into waveguides on other materials such as silicon [200,201], or can be defined within a SOI substrate using techniques such as wafer bonding [122]. A network of photonic neurons could open computational domains that demand unprecedented temporal precision, power efficiency, and functional complexity, potentially including applications in wideband RF processing, adaptive control of multi-antenna systems, and high-performance scientific computing.

To enable a practical scalable information processing platform, the key criteria for a computational primitive include logic-level restoration, cascadability, and fan-out/input–output isolation [1]. It has been experimentally verified in [31,37] that the two-section gain-SA excitable laser can meet all these criteria, while the RTD-PD driving LD can, in principle, allow for cascadability and fan-in. Recent investigations 28,47]] have suggested that the primary barrier to exploiting the high bandwidth of photonic devices for computing lies not in the performance, integration, or fabrication of devices, but instead in the model of computation being used (digital logic and specialized analog function acceleration). Analog photonic processing has found widespread application in high bandwidth filtering of microwave signals [202], but the accumulation of phase noise, in addition to amplitude noise, makes cascaded operations particularly difficult. Digital logic gates that suppress amplitude noise accumulation have also been realized in photonics, but proposed optical logic devices have not yet met all the conditions of cascadability [1], let alone scalability, which includes high fabrication yield.

Any proposal for a computational primitive must address the issue of practical cascadability, especially if multiple wavelength channels are intended to be used. For example, the B&W networking architecture proposed in [28] relies on WDM for interconnecting many laser neurons together. In addition, as argued in Section 4, schemes that exhibit limitations with regards to wavelength channels may require

a large number of wavelength conversion steps, which can be costly, noisy, and inefficient. Photonic unconventional computing primitives address the traditional problem of noise accumulation by interleaving physical representations of information. Representational interleaving, in which a signal is repeatedly transformed between coding schemes (digital–analog) or physical variables (electronic–optical), can grant many advantages to computation and noise properties. As noted by Sarpeshkar [55], hybrid analog–digital systems—particularly those composed of moderately precise analog units coupled together—maximize processing while minimizing time, energy, and material costs.

There are a variety of schemes that could be used that are not necessarily spiking. The simplest hybrid analog–digital units are perceptrons, which perform analog computation and use a nonlinear transfer function to suppress analog noise. However, perceptrons lack time-dependent properties and are thus better suited for function approximation rather than the exploration of nonlinear dynamical systems. The spiking model found in biology naturally interleaves robust, discrete representations for communication with precise, continuous representations for computation in order to reap the benefits of both digital and analog. Specifically, spiking has two primary advantages over synchronous analog: (1) its analog variable (time) is much less noisy than its digital variable (amplitude) so the digital–analog assignment is much more sensible, and (2) it is asynchronous, which allows for far more autonomy for system design without a global clock, at the minor cost of preventing techniques such as TDM. Spiking exhibits a large number of advantages for analog–digital processing, which may account for its ubiquity in natural processing systems [56]. It is natural to deepen this distinction to include physical representational aspects, with the important result that optical noise does not accumulate. When a pulse is generated, it is transmitted and routed through a linear optical network with the help of its wavelength identifier.

6. CONCLUSION

Photonic spike processing is poised to usher in a promising and exciting field motivated by bringing computation closer to its underlying physics. The field is currently reaching a critical juncture where there is a shift from studying the dynamical properties of individual lasers to interconnected networks. This review paper attempts to provide a thorough treatment of the field spanning from its theoretical considerations to experimental explorations, from fundamental carrier and photon dynamics at the device level to networking and fan-in on a systems level.

Moving forward, we envision tremendous interest in the field for designing, building, and understanding a photonic network of excitable elements for ultrafast information processing, inspired in part by the latest computational models of the brain. Successful implementation of a small-scale *photonic spike processor*, could, in principle, provide the fundamental technology to build and study larger scale brain-inspired networks that operate on principles of laser excitability.

Finally, while this review will be of general interest to the photonics and optics community, we hope that it will also contribute to stimulating dialogue in the cross-disciplinary areas of photonics and optics, neuromorphic engineering, and signal processing, from fundamental principles to practical applications. As a whole, the field of photonic spike processing has received a significant amount of interest and continues to receive further developments as integrated PICs increase in performance and scale. As novel applications requiring real-time, ultrafast processing—such as the exploitation of the RF spectrum—become more critical, we expect that these systems will find use in a variety of high-performance, time-critical environments.

FUNDING

Defense Advanced Research Projects Agency (DARPA) DARPA-BAA-12-64; Natural Sciences and Engineering Research Council of Canada (NSERC); National Science Foundation (NSF) Graduate Research Fellowship Program (GRFP).

ACKNOWLEDGMENT

B. J. S. acknowledges the support of the Banting Postdoctoral Fellowship administered by the Government of Canada through the Natural Sciences and Engineering Research Council of Canada (NSERC). M. A. N. and A. N. T. acknowledge the support of the National Science Foundation Graduate Research Fellowship Program (NSF GRFP).

[†]These authors contributed equally to this paper.

REFERENCES AND NOTES

1. D. A. B. Miller, "Are optical transistors the logical next step?" Nat. Photonics **4**, 3–5 (2010).
2. D. A. B. Miller, "Joining optics and electronics for information processing and communication," in *The 20th Annual Meeting of the IEEE Lasers and Electro-Optics Society* (2007), pp. 547–548.
3. H. Jaeger and H. Haas, "Harnessing nonlinearity: predicting chaotic systems and saving energy in wireless communication," Science **304**, 78–80 (2004).
4. J. Hasler and B. Marr, "Finding a roadmap to achieve large neuromorphic hardware systems," Front. Neurosci. **7**, 118 (2013).
5. P. A. Merolla, J. V. Arthur, R. Alvarez-Icaza, A. S. Cassidy, J. Sawada, F. Akopyan, B. L. Jackson, N. Imam, C. Guo, Y. Nakamura, B. Brezzo, I. Vo, S. K. Esser, R. Appuswamy, B. Taba, A. Amir, M. D. Flickner, W. P. Risk, R. Manohar, and D. S. Modha, "A million spiking-neuron integrated circuit with a scalable communication network and interface," Science **345**, 668–673 (2014).
6. D. S. Modha, R. Ananthanarayanan, S. K. Esser, A. Ndirango, A. J. Sherbondy, and R. Singh, "Cognitive computing," Commun. ACM **54**, 62–71 (2011).
7. R. S. Tucker, "The role of optics in computing," Nat. Photonics **4**, 405 (2010).
8. H. J. Caulfield and S. Dolev, "Why future supercomputing requires optics," Nat. Photonics **4**, 261–263 (2010).
9. D. Woods and T. J. Naughton, "Optical computing: photonic neural networks," Nat. Phys. **8**, 257–259 (2012).
10. B. Benjamin, P. Gao, E. McQuinn, S. Choudhary, A. Chandrasekaran, J.-M. Bussat, R. Alvarez-Icaza, J. Arthur, P. Merolla, and K. Boahen, "Neurogrid: a mixed-analog-digital multichip system for large-scale neural simulations," Proc. IEEE **102**, 699–716 (2014).
11. T. Pfeil, A. Grübl, S. Jeltsch, E. Müller, P. Müller, M. A. Petrovici, M. Schmuker, D. Brüderle, J. Schemmel, and K. Meier, "Six networks on a universal neuromorphic computing substrate," Front. Neurosci. **7** (2013), doi: 10.3389/fnins.2013.00011.
12. S. Furber, F. Galluppi, S. Temple, and L. Plana, "The spinnaker project," Proc. IEEE **102**, 652–665 (2014).
13. G. S. Snider, "Self-organized computation with unreliable, memristive nanodevices," Nanotechnology **18**, 365202 (2007).

14. C. Eliasmith, T. C. Stewart, X. Choo, T. Bekolay, T. DeWolf, Y. Tang, and D. Rasmussen, "A large-scale model of the functioning brain," Science **338**, 1202–1205 (2012).
15. G. Indiveri, B. Linares-Barranco, T. J. Hamilton, A. van Schaik, R. Etienne-Cummings, T. Delbruck, S.-C. Liu, P. Dudek, P. Hafliger, S. Renaud, J. Schemmel, G. Cauwenberghs, J. Arthur, K. Hynna, F. Folowosele, S. Saighi, T. Serrano-Gotarredona, J. Wijekoon, Y. Wang, and K. Boahen, "Neuromorphic silicon neuron circuits," Front. Neurosci. **5** (2011), doi: 10.3389/fnins.2011.00073.
16. A. N. Tait, M. A. Nahmias, Y. Tian, B. J. Shastri, and P. R. Prucnal, "Photonic neuromorphic signal processing and computing," in *Nanophotonic Information Physics*, M. Naruse, ed. (Springer, 2014), pp. 183–222.
17. B. J. Shastri, A. N. Tait, M. A. Nahmias, and P. R. Prucnal, "Photonic spike processing: ultrafast laser neurons and an integrated photonic network," IEEE Photon. Soc. Newslett. **28**(3), 4–11 (2014).
18. H. Paugam-Moisy and S. Bohte, "Computing with spiking neuron networks," in *Handbook of Natural Computing* (Springer, 2012), pp. 335–376.
19. E. Izhikevich, "Simple model of spiking neurons," IEEE Trans. Neural Netw. **14**, 1569–1572 (2003).
20. S. Ostojic, "Two types of asynchronous activity in networks of excitatory and inhibitory spiking neurons," Nat. Neurosci. **17**, 594–600 (2014).
21. D. Rosenbluth, K. Kravtsov, M. P. Fok, and P. R. Prucnal, "A high performance photonic pulse processing device," Opt. Express **17**, 22767–22772 (2009).
22. B. Kelleher, C. Bonatto, P. Skoda, S. P. Hegarty, and G. Huyet, "Excitation regeneration in delay-coupled oscillators," Phys. Rev. E **81**, 036204 (2010).
23. L. Appeltant, M. C. Soriano, G. Van der Sande, J. Danckaert, S. Massar, J. Dambre, B. Schrauwen, C. R. Mirasso, and I. Fischer, "Information processing using a single dynamical node as complex system," Nat. Commun. **2**, 468 (2011).
24. K. S. Kravtsov, M. P. Fok, P. R. Prucnal, and D. Rosenbluth, "Ultrafast all-optical implementation of a leaky integrate-and-fire neuron," Opt. Express **19**, 2133–2147 (2011).
25. D. Brunner, M. C. Soriano, C. R. Mirasso, and I. Fischer, "Parallel photonic information processing at gigabyte per second data rates using transient states," Nat. Commun. **4**, 1364 (2013).
26. K. Vandoorne, P. Mechet, T. Van Vaerenbergh, M. Fiers, G. Morthier, D. Verstraeten, B. Schrauwen, J. Dambre, and P. Bienstman, "Experimental demonstration of reservoir computing on a silicon photonics chip," Nat. Commun. **5**, 3451 (2014).
27. A. Aragoneses, S. Perrone, T. Sorrentino, M. C. Torrent, and C. Masoller, "Unveiling the complex organization of recurrent patterns in spiking dynamical systems," Sci. Rep. **4**, 4696 (2014).
28. A. Tait, M. Nahmias, B. Shastri, and P. Prucnal, "Broadcast and weight: an integrated network for scalable photonic spike processing," J. Lightwave Technol. **32**, 4029–4041 (2014).
29. B. Garbin, J. Javaloyes, G. Tissoni, and S. Barland, "Topological solitons as addressable phase bits in a driven laser," Nat. Commun. **6**, 5915 (2015).
30. B. Romeira, R. Avó, J. L. Figueiredo, S. Barland, and J. Javaloyes, "Regenerative memory in time-delayed neuromorphic photonic resonators," Sci. Rep. **6**, 19510 (2016).
31. B. J. Shastri, M. A. Nahmias, A. N. Tait, A. W. Rodriguez, B. Wu, and P. R. Prucnal, "Spike processing with a graphene excitable laser," Sci. Rep. **6**, 19126 (2016).

32. M. P. Fok, H. Deming, M. Nahmias, N. Rafidi, D. Rosenbluth, A. Tait, Y. Tian, and P. R. Prucnal, "Signal feature recognition based on lightwave neuromorphic signal processing," Opt. Lett. **36**, 19–21 (2011).
33. W. Coomans, L. Gelens, S. Beri, J. Danckaert, and G. Van der Sande, "Solitary and coupled semiconductor ring lasers as optical spiking neurons," Phys. Rev. E **84**, 036209 (2011).
34. M. Brunstein, A. M. Yacomotti, I. Sagnes, F. Raineri, L. Bigot, and A. Levenson, "Excitability and self-pulsing in a photonic crystal nanocavity," Phys. Rev. A **85**, 031803 (2012).
35. M. A. Nahmias, B. J. Shastri, A. N. Tait, and P. R. Prucnal, "A leaky integrate-and-fire laser neuron for ultrafast cognitive computing," IEEE J. Sel. Top. Quantum Electron. **19**, 1800212 (2013).
36. T. Van Vaerenbergh, K. Alexander, J. Dambre, and P. Bienstman, "Excitation transfer between optically injected microdisk lasers," Opt. Express **21**, 28922–28932 (2013).
37. F. Selmi, R. Braive, G. Beaudoin, I. Sagnes, R. Kuszelewicz, and S. Barbay, "Relative refractory period in an excitable semiconductor laser," Phys. Rev. Lett. **112**, 183902 (2014).
38. A. Hurtado and J. Javaloyes, "Controllable spiking patterns in long-wavelength vertical cavity surface emitting lasers for neuromorphic photonics systems," Appl. Phys. Lett. **107**, 241103 (2015).
39. A. M. Yacomotti, P. Monnier, F. Raineri, B. B. Bakir, C. Seassal, R. Raj, and J. A. Levenson, "Fast thermo-optical excitability in a two-dimensional photonic crystal," Phys. Rev. Lett. **97**, 143904 (2006).
40. D. Goulding, S. P. Hegarty, O. Rasskazov, S. Melnik, M. Hartnett, G. Greene, J. G. McInerney, D. Rachinskii, and G. Huyet, "Excitability in a quantum dot semiconductor laser with optical injection," Phys. Rev. Lett. **98**, 4–7 (2007).
41. A. Hurtado, I. D. Henning, and M. J. Adams, "Optical neuron using polarization switching in a 1550 nm-VCSEL," Opt. Express **18**, 25170–25176 (2010).
42. W. Coomans, "Nonlinear dynamics in semiconductor ring lasers towards an integrated optical neuron," Ph.D. thesis (Vrije Universiteit Brussel, 2012).
43. T. Van Vaerenbergh, M. Fiers, P. Mechet, T. Spuesens, R. Kumar, G. Morthier, B. Schrauwen, J. Dambre, and P. Bienstman, "Cascadable excitability in microrings," Opt. Express **20**, 20292 (2012).
44. A. Hurtado, K. Schires, I. D. Henning, and M. J. Adams, "Investigation of vertical cavity surface emitting laser dynamics for neuromorphic photonic systems," Appl. Phys. Lett. **100**, 103703 (2012).
45. B. Romeira, J. Javaloyes, C. N. Ironside, J. M. L. Figueiredo, S. Balle, and O. Piro, "Excitability and optical pulse generation in semiconductor lasers driven by resonant tunneling diode photo-detectors," Opt. Express **21**, 20931–20940 (2013).
46. B. Romeira, R. Avó, J. Javaloyes, S. Balle, C. Ironside, and J. Figueiredo, "Stochastic induced dynamics in neuromorphic optoelectronic oscillators," Opt. Quantum Electron. **46**, 1391–1396 (2014).
47. M. A. Nahmias, A. N. Tait, B. J. Shastri, T. F. de Lima, and P. R. Prucnal, "Excitable laser processing network node in hybrid silicon: analysis and simulation," Opt. Express **23**, 26800–26813 (2015).
48. T. Sorrentino, C. Quintero-Quiroz, A. Aragoneses, M. C. Torrent, and C. Masoller, "Effects of periodic forcing on the temporally correlated spikes of a semiconductor laser with feedback," Opt. Express **23**, 5571–5581 (2015).
49. A. L. Hodgkin and A. F. Huxley, "A quantitative description of membrane current and its application to conduction and excitation in nerve," J. Physiol. **117**, 500–544 (1952).

50. B. Krauskopf, K. Schneider, J. Sieber, S. Wieczorek, and M. Wolfrum, "Excitability and self-pulsations near homoclinic bifurcations in semiconductor laser systems," Opt. Commun. **215**, 367–379 (2003).
51. D. Gomila, M. A. Matías, and P. Colet, "Excitability mediated by localized structures in a dissipative nonlinear optical cavity," Phys. Rev. Lett. **94**, 063905 (2005).
52. A. Kumar, S. Rotter, and A. Aertsen, "Spiking activity propagation in neuronal networks: reconciling different perspectives on neural coding," Nat. Rev. Neurosci. **11**, 615–627 (2010).
53. M. Diesmann, M.-O. Gewaltig, and A. Aertsen, "Stable propagation of synchronous spiking in cortical neural networks," Nature **402**, 529–533 (1999).
54. A. Borst and F. E. Theunissen, "Information theory and neural coding," Nat. Neurosci. **2**, 947–957 (1999).
55. R. Sarpeshkar, "Analog versus digital: extrapolating from electronics to neurobiology," Neural Comput. **10**, 1601–1638 (1998).
56. S. Thorpe, A. Delorme, and R. V. Rullen, "Spike-based strategies for rapid processing," Neural Netw. **14**, 715–725 (2001).
57. W. Maass, T. Natschläger, and H. Markram, "Real-time computing without stable states: a new framework for neural computation based on perturbations," Neural Comput. **14**, 2531–2560 (2002).
58. W. Maass, "Networks of spiking neurons: the third generation of neural network models," Neural Netw. **10**, 1659–1671 (1997).
59. E. M. Izhikevich, "Polychronization: computation with spikes," Neural Comput. **18**, 245–282 (2006).
60. J. Schemmel, D. Briiderle, A. Griibl, M. Hock, K. Meier, and S. Millner, "A wafer-scale neuromorphic hardware system for large-scale neural modeling," in *Proceedings of IEEE International Symposium on Circuits and Systems* (IEEE, 2010), pp. 1947–1950.
61. The HBP Report, "The Human Brain Project," Technical Report (2012).
62. D. A. B. Miller, "Rationale and challenges for optical interconnects to electronic chips," Proc. IEEE **88**, 728–749 (2000).
63. K. Boahen, "Point-to-point connectivity between neuromorphic chips using address events," IEEE Trans. Circuits Syst. II **47**, 416–434 (2000).
64. E. D. Adrian, *The Basis of Sensation* (Norton, 1928).
65. F. Rieke, *Spikes: Exploring the Neural Code* (MIT, 1999).
66. C. Mead, "Neuromorphic electronic systems," Proc. IEEE **78**, 1629–1636 (1990).
67. S. Haykin, *Neural Networks and Learning Machines*, 3rd ed. (Prentice Hall, 2009), Vol. **5**.
68. Y. Bengio, A. Courville, and P. Vincent, "Representation learning: a review and new perspectives," IEEE Trans. Pattern Anal. Mach. Intell. **35**, 1798–1828 (2013).
69. D. I. Perrett, E. T. Rolls, and W. Caan, "Visual neurones responsive to faces in the monkey temporal cortex," Exp. Brain Res. **47**, 329–342 (1982).
70. W. Maass and C. M. Bishop, *Pulsed Neural Networks* (MIT, 2001).
71. E. M. Izhikevich, "Which model to use for cortical spiking neurons?" IEEE Trans. Neural Netw. **15**, 1063–1070 (2004).
72. C. Eliasmith and C. H. Anderson, *Neural Engineering: Computation, Representation, and Dynamics in Neurobiological Systems* (MIT, 2004).
73. J. C. Tapson, G. K. Cohen, S. Afshar, K. M. Stiefel, Y. Buskila, R. M. Wang, T. J. Hamilton, and A. van Schaik, "Synthesis of neural networks for spatio-temporal spike pattern recognition and processing," Front. Neurosci. **7**, 153 (2013).
74. F. C. Hoppensteadt and E. M. Izhikevich, *Weakly Connected Neural Networks* (Springer-Verlag, 1997).

75. E. M. Izhikevich, "Neural excitability, spiking and bursting," Int. J. Bifur. Chaos **10**, 1171–1266 (2000).
76. This is the most usual definition in the literature of dynamical systems. In mathematics literature, these points are actually called *stationary*, or *critical*, and *fixed points* stand for the solution of $f(x) = x$.
77. E. M. Izhikivich, *Dynamical Systems in Neuroscience: The Geometry of Excitability and Bursting* (MIT, 2006), Vol. **25**.
78. A. L. Hodgkin, "The local electric changes associated with repetitive action in a non-medullated axon," J. Physiol. **107**, 165–181 (1948).
79. In simple words, this happens when a limit cycle collides with a node, annihilating each other. It is called supercritical when the limit cycle is stable and subcritical otherwise.
80. More mathematically, the codimension of the subset of A_Ω over which the bifurcation occurs. For example, a point and a line in 2D have codimensions two and one, respectively.
81. G. J. Spühler, R. Paschotta, R. Fluck, B. Braun, M. Moser, G. Zhang, E. Gini, and U. Keller, "Experimentally confirmed design guidelines for passively Q-switched microchip lasers using semiconductor saturable absorbers," J. Opt. Soc. Am. B **16**, 376–388 (1999).
82. J. L. A. Dubbeldam and B. Krauskopf, "Self-pulsations of lasers with saturable absorber: dynamics and bifurcations," Opt. Commun. **159**, 325–338 (1999).
83. J. L. A. Dubbeldam, B. Krauskopf, and D. Lenstra, "Excitability and coherence resonance in lasers with saturable absorber," Phys. Rev. E **60**, 6580–6588 (1999).
84. S. Barbay, R. Kuszelewicz, and A. M. Yacomotti, "Excitability in a semiconductor laser with saturable absorber," Opt. Lett. **36**, 4476–4478 (2011).
85. E. M. Izhikevich, "Resonate-and-fire neurons," Neural Netw. **14**, 883–894 (2001).
86. M. A. Larotonda, A. Hnilo, J. M. Mendez, and A. M. Yacomotti, "Experimental investigation on excitability in a laser with a saturable absorber," Phys. Rev. A **65**, 033812 (2002).
87. T. Elsass, K. Gauthron, G. Beaudoin, I. Sagnes, R. Kuszelewicz, and S. Barbay, "Control of cavity solitons and dynamical states in a monolithic vertical cavity laser with saturable absorber," Eur. Phys. J. D **59**, 91–96 (2010).
88. B. J. Shastri, M. A. Nahmias, A. N. Tait, and P. R. Prucnal, "Simulations of a graphene excitable laser for spike processing," Opt. Quantum Electron. **46**, 1353–1358 (2014).
89. F. Selmi, R. Braive, G. Beaudoin, I. Sagnes, R. Kuszelewicz, and S. Barbay, "Temporal summation in a neuromimetic micropillar laser," Opt. Lett. **40**, 5690–5693 (2015).
90. B. J. Shastri, M. A. Nahmias, A. N. Tait, B. Wu, and P. R. Prucnal, "SIMPEL: circuit model for photonic spike processing laser neurons," Opt. Express **23**, 8029–8044 (2015).
91. W. Coomans, S. Beri, G. V. D. Sande, L. Gelens, and J. Danckaert, "Optical injection in semiconductor ring lasers," Phys. Rev. A **81**, 033802 (2010).
92. L. Gelens, L. Mashal, S. Beri, W. Coomans, G. Van der Sande, J. Danckaert, and G. Verschaffelt, "Excitability in semiconductor microring lasers: experimental and theoretical pulse characterization," Phys. Rev. A **82**, 063841 (2010).
93. W. Coomans, G. Van der Sande, and L. Gelens, "Oscillations and multistability in two semiconductor ring lasers coupled by a single waveguide," Phys. Rev. A **88**, 033813 (2013).
94. K. Alexander, T. Van Vaerenbergh, M. Fiers, P. Mechet, J. Dambre, and P. Bienstman, "Excitability in optically injected microdisk lasers with phase controlled excitatory and inhibitory response," Opt. Express **21**, 26182 (2013).

95. A. M. Yacomotti, F. Raineri, G. Vecchi, P. Monnier, R. Raj, A. Levenson, B. Ben Bakir, C. Seassal, X. Letartre, P. Viktorovitch, L. Di Cioccio, and J. M. Fedeli, "All-optical bistable band-edge Bloch modes in a two-dimensional photonic crystal," Appl. Phys. Lett. **88**, 231107 (2006).
96. B. Romeira, "Dynamics of resonant tunneling diode optoelectronic oscillators," Ph.D. thesis (Universidade do Algarve, 2012).
97. S. Wieczorek, B. Krauskopf, and D. Lenstra, "Unifying view of bifurcations in a semiconductor laser subject to optical injection," Opt. Commun. **172**, 279–295 (1999).
98. S. Wieczorek, B. Krauskopf, and D. Lenstra, "Multipulse excitability in a semiconductor laser with optical injection," Phys. Rev. Lett. **88**, 063901 (2002).
99. S. Barland, O. Piro, M. Giudici, J. R. Tredicce, and S. Balle, "Experimental evidence of van der Pol-Fitzhugh–Nagumo dynamics in semiconductor optical amplifiers," Phys. Rev. E **68**, 036209 (2003).
100. S. Wieczorek, B. Krauskopf, T. B. Simpson, and D. Lenstra, "The dynamical complexity of optically injected semiconductor lasers," Phys. Rep. **416**, 1–128 (2005).
101. F. Marino and S. Balle, "Excitable optical waves in semiconductor microcavities," Phys. Rev. Lett. **94**, 094101 (2005).
102. B. Kelleher, C. Bonatto, G. Huyet, and S. P. Hegarty, "Excitability in optically injected semiconductor lasers: Contrasting quantum-well- and quantum-dot-based devices," Phys. Rev. E **83**, 026207 (2011).
103. M. Turconi, B. Garbin, M. Feyereisen, M. Giudici, and S. Barland, "Control of excitable pulses in an injection-locked semiconductor laser," Phys. Rev. E **88**, 022923 (2013).
104. B. Garbin, D. Goulding, S. P. Hegarty, G. Huyet, B. Kelleher, and S. Barland, "Incoherent optical triggering of excitable pulses in an injection-locked semiconductor laser," Opt. Lett. **39**, 1254–1257 (2014).
105. M. Giudici, C. Green, G. Giacomelli, U. Nespolo, and J. R. Tredicce, "Andronov bifurcation and excitability in semiconductor lasers with optical feedback," Phys. Rev. E **55**, 6414–6418 (1997).
106. A. M. Yacomotti, M. C. Eguia, J. Aliaga, O. E. Martinez, G. B. Mindlin, and A. Lipsich, "Interspike time distribution in noise driven excitable systems," Phys. Rev. Lett. **83**, 292–295 (1999).
107. G. Giacomelli, M. Giudici, S. Balle, and J. R. Tredicce, "Experimental evidence of coherence resonance in an optical system," Phys. Rev. Lett. **84**, 3298–3301 (2000).
108. T. Heil, I. Fischer, W. Elsäßer, and A. Gavrielides, "Dynamics of semiconductor lasers subject to delayed optical feedback: the short cavity regime," Phys. Rev. Lett. **87**, 243901 (2001).
109. H. J. Wünsche, O. Brox, M. Radziunas, and F. Henneberger, "Excitability of a semiconductor laser by a two-mode homoclinic bifurcation," Phys. Rev. Lett. **88**, 023901 (2001).
110. R. C. Froemke and Y. Dan, "Spike-timing-dependent synaptic modification induced by natural spike trains," Nature **416**, 433–438 (2002).
111. L. F. Abbott and S. B. Nelson, "Synaptic plasticity: taming the beast," Nat. Neurosci. **3**, 1178–1183 (2000).
112. S. P. Strong, R. Koberle, R. R. D. R. van Steveninck, and W. Bialek, "Entropy and information in neural spike trains," Phys. Rev. Lett. **80**, 197–200 (1998).
113. M. Yamada, "A theoretical analysis of self-sustained pulsation phenomena in narrow-stripe semiconductor lasers," IEEE J. Quantum Electron. **29**, 1330–1336 (1993).

114. C. Zhang, S. Srinivasan, Y. Tang, M. J. Heck, M. L. Davenport, and J. E. Bowers, "Low threshold and high speed short cavity distributed feedback hybrid silicon lasers," Opt. Express **22**, 10202–10209 (2014).
115. H. Boudinov, H. H. Tan, and C. Jagadish, "Electrical isolation of n-type and p-type InP layers by proton bombardment," J. Appl. Phys. **89**, 5343 (2001).
116. A. Martinez and Z. Sun, "Nanotube and graphene saturable absorbers for fibre lasers," Nat. Photonics **7**, 842–845 (2013).
117. Q. Bao, H. Zhang, Y. Wang, Z. Ni, Y. Yan, Z. X. Shen, K. P. Loh, and D. Y. Tang, "Atomic-layer graphene as a saturable absorber for ultrafast pulsed lasers," Adv. Funct. Mater. **19**, 3077–3083 (2009).
118. Z. Sun, T. Hasan, F. Torrisi, D. Popa, G. Privitera, F. Wang, F. Bonaccorso, D. M. Basko, and A. C. Ferrari, "Graphene mode-locked ultrafast laser," ACS Nano **4**, 803–810 (2010).
119. G. Xing, H. Guo, X. Zhang, T. C. Sum, and C. H. A. Huan, "The physics of ultrafast saturable absorption in graphene," Opt. Express **18**, 4564–4573 (2010).
120. U. Keller, K. Weingarten, F. Kartner, D. Kopf, B. Braun, I. Jung, R. Fluck, C. Honninger, N. Matuschek, and J. Aus der Au, "Semiconductor saturable absorber mirrors (SESAM's) for femtosecond to nanosecond pulse generation in solid-state lasers," IEEE J. Sel. Top. Quantum Electron. **2**, 435–453 (1996).
121. K. S. Novoselov, V. I. Fal'ko, L. Colombo, P. R. Gellert, M. G. Schwab, and K. Kim, "A roadmap for graphene," Nature **490**, 192–200 (2012).
122. A. W. Fang, E. Lively, Y.-H. Kuo, D. Liang, and J. E. Bowers, "A distributed feedback silicon evanescent laser," Opt. Express **16**, 4413–4419 (2008).
123. A. W. Fang, H. Park, Y.-H. Kuo, R. Jones, O. Cohen, D. Liang, O. Raday, M. N. Sysak, M. J. Paniccia, and J. E. Bowers, "Hybrid silicon evanescent devices," Mater. Today **10**(7–8), 28–35 (2007).
124. A. W. Fang, H. Park, O. Cohen, R. Jones, M. J. Paniccia, and J. E. Bowers, "Electrically pumped hybrid AlGaInAs-silicon evanescent laser," Opt. Express **14**, 9203–9210 (2006).
125. H. Markram, J. Lübke, M. Frotscher, and B. Sakmann, "Regulation of synaptic efficacy by coincidence of postsynaptic APs and EPSPs," Science **275**, 213–215 (1997).
126. E. M. Izhikevich, N. S. Desai, E. C. Walcott, and F. C. Hoppensteadt, "Bursts as a unit of neural information: selective communication via resonance," Trends Neurosci. **26**, 161–167 (2003).
127. S. Reitzenstein and A. Forchel, "Quantum dot micropillars," J. Phys. D **43**, 033001 (2010).
128. P. Mechet, S. Verstuyft, T. D. Vries, T. Spuesens, P. Regreny, D. V. Thourhout, G. Roelkens, and G. Morthier, "Unidirectional III-V microdisk lasers heterogeneously integrated on SOI," Opt. Express **21**, 1988–1990 (2013).
129. J. Van Campenhout, P. Romeo, D. Van Thourhout, C. Seassal, P. Regreny, L. Di Cioccio, J.-M. Fedeli, and R. Baets, "Design and optimization of electrically injected InP-based microdisk lasers integrated on and coupled to a SOI waveguide circuit," J. Lightwave Technol. **26**, 52–63 (2008).
130. M. Sorel, P. J. R. Laybourn, A. Scirè, S. Balle, G. Giuliani, R. Miglierina, and S. Donati, "Alternate oscillations in semiconductor ring lasers," Opt. Lett. **27**, 1992–1994 (2002).
131. L. Gelens, S. Beri, G. Van Der Sande, G. Verschaffelt, and J. Danckaert, "Multistable and excitable behavior in semiconductor ring lasers with broken Z_2-symmetry," Eur. Phys. J. D **58**, 197–207 (2010).
132. E. Yablonovitch, "Inhibited spontaneous emission in solid-state physics and electronics," Phys. Rev. Lett. **58**, 2059–2062 (1987).

133. S. John, "Strong localization of photons in certain disordered dielectric superlattices," Phys. Rev. Lett. **58**, 2486–2489 (1987).
134. M. Soljačić, M. Ibanescu, S. G. Johnson, Y. Fink, and J. D. Joannopoulos, "Optimal bistable switching in nonlinear photonic crystals," Phys. Rev. E **66**, 055601 (2002).
135. T. Tanabe, M. Notomi, S. Mitsugi, A. Shinya, and E. Kuramochi, "All-optical switches on a silicon chip realized using photonic crystal nanocavities," Appl. Phys. Lett. **87**, 151112 (2005).
136. C.-H. Chen, S. Matsuo, K. Nozaki, A. Shinya, T. Sato, Y. Kawaguchi, H. Sumikura, and M. Notomi, "All-optical memory based on injection-locking bistability in photonic crystal lasers," Opt. Express **19**, 3387–3395 (2011).
137. M.-K. Kim, I.-K. Hwang, S.-H. Kim, H.-J. Chang, and Y.-H. Lee, "All-optical bistable switching in curved microfiber-coupled photonic crystal resonators," Appl. Phys. Lett. **90**, 161118 (2007).
138. M. Notomi, T. Tanabe, A. Shinya, E. Kuramochi, H. Taniyama, S. Mitsugi, and M. Morita, "Nonlinear and adiabatic control of high-Q photonic crystal nanocavities," Opt. Express **15**, 17458–17481 (2007).
139. M. Brunstein, R. Braive, R. Hostein, A. Beveratos, I. Robert-Philip, I. Sagnes, T. J. Karle, A. M. Yacomotti, J. A. Levenson, V. Moreau, G. Tessier, and Y. D. Wilde, "Thermo-optical dynamics in an optically pumped photonic crystal nanocavity," Opt. Express **17**, 17118–17129 (2009).
140. B. Maes, M. Fiers, and P. Bienstman, "Self-pulsing and chaos in short chains of coupled nonlinear microcavities," Phys. Rev. A **80**, 033805 (2009).
141. S. Malaguti, G. Bellanca, A. de Rossi, S. Combrié, and S. Trillo, "Self-pulsing driven by two-photon absorption in semiconductor nanocavities," Phys. Rev. A **83**, 051802 (2011).
142. V. Grigoriev and F. Biancalana, "Resonant self-pulsations in coupled nonlinear microcavities," Phys. Rev. A **83**, 043816 (2011).
143. M. Brunstein, A. M. Yacomotti, R. Braive, S. Barbay, I. Sagnes, L. Bigot, L. Le-Gratiet, and J. A. Levenson, "All-optical, all-fibered ultrafast switching in 2-D InP-based photonic crystal nanocavity," IEEE Photon. J. **2**, 642–651 (2010).
144. F. Raineri, C. Cojocaru, P. Monnier, A. Levenson, R. Raj, C. Seassal, X. Letartre, and P. Viktorovitch, "Ultrafast dynamics of the third-order nonlinear response in a two-dimensional InP-based photonic crystal," Appl. Phys. Lett. **85**, 1880–1882 (2004).
145. T. Tanabe, M. Notomi, E. Kuramochi, A. Shinya, and H. Taniyama, "Trapping and delaying photons for one nanosecond in an ultrasmall high-Q photonic-crystal nanocavity," Nat. Photonics **1**, 49–52 (2007).
146. B. Romeira, J. Javaloyes, J. Figueiredo, C. Ironside, H. Cantu, and A. Kelly, "Delayed feedback dynamics of Liénard-type resonant tunneling-photo-detector optoelectronic oscillators," IEEE J. Quantum Electron. **49**, 31–42 (2013).
147. F. Hartmann, L. Gammaitoni, S. Höfling, A. Forchel, and L. Worschech, "Light-induced stochastic resonance in a nanoscale resonant-tunneling diode," Appl. Phys. Lett. **98**, 242109 (2011).
148. P. Mazumder, S.-R. Li, and I. Ebong, "Tunneling-based cellular nonlinear network architectures for image processing," IEEE Trans. Very Large Scale Integr. Syst. **17**, 487–495 (2009).
149. S. Suzuki, M. Shiraishi, H. Shibayama, and M. Asada, "High-power operation of terahertz oscillators with resonant tunneling diodes using impedance-matched antennas and array configuration," IEEE J. Sel. Top. Quantum Electron. **19**, 8500108 (2013).
150. D. Bohm, *Quantum Theory* (Courier, 2012).
151. H. Mizuta and T. Tanoue, *The Physics and Applications of Resonant Tunnelling Diodes* (Cambridge University, 2006), Vol. **2**.

152. J. Schulman, H. De Los Santos, and D. Chow, "Physics-based RTD current-voltage equation," IEEE Electron Device Lett. **17**, 220–222 (1996).
153. B. Lindner, J. Garcia-Ojalvo, A. Neiman, and L. Schimansky-Geier, "Effects of noise in excitable systems," Phys. Rep. **392**, 321–424 (2004).
154. P. Coullet, D. Daboussy, and J. R. Tredicce, "Optical excitable waves," Phys. Rev. E **58**, 5347–5350 (1998).
155. R. Al-Seyab, K. Schires, N. Ali Khan, A. Hurtado, I. D. Henning, and M. J. Adams, "Dynamics of polarized optical injection in 1550-nm VCSELs: theory and experiments," IEEE J. Sel. Top. Quantum Electron. **17**, 1242–1249 (2011).
156. A. Hurtado, A. Quirce, A. Valle, L. Pesquera, and M. J. Adams, "Nonlinear dynamics induced by parallel and orthogonal optical injection in 1550 nm vertical-cavity surface-emitting lasers (VCSELs)," Opt. Express **18**, 9423–9428 (2010).
157. I. Gatare, M. Sciamanna, J. Buesa, H. Thienpont, and K. Panajotov, "Nonlinear dynamics accompanying polarization switching in vertical-cavity surface-emitting lasers with orthogonal optical injection," Appl. Phys. Lett. **88**, 101106 (2006).
158. Z. G. Pan, S. Jiang, M. Dagenais, R. A. Morgan, K. Kojima, M. T. Asom, R. E. Leibenguth, G. D. Guth, and M. W. Focht, "Optical injection induced polarization bistability in vertical-cavity surface-emitting lasers," Appl. Phys. Lett. **63**, 2999–3001 (1993).
159. K. H. Jeong, K. H. Kim, S. H. Lee, M. H. Lee, B.-S. Yoo, and K. Shore, "Optical injection-induced polarization switching dynamics in 1.5-μm wavelength single-mode vertical-cavity surface-emitting lasers," IEEE Photon. Technol. Lett. **20**, 779–781 (2008).
160. G. H. van Tartwijk and G. P. Agrawal, "Laser instabilities: a modern perspective," Prog. Quantum Electron. **22**, 43–122 (1998).
161. G. Van Tartwijk and D. Lenstra, "Semiconductor lasers with optical injection and feedback," J. Eur. Opt. Soc. Part B **7**, 89–143 (1995).
162. D. Pieroux, T. Erneux, T. Luzyanina, and K. Engelborghs, "Interacting pairs of periodic solutions lead to tori in lasers subject to delayed feedback," Phys. Rev. E **63**, 036211 (2001).
163. R. L. Davidchack, Y.-C. Lai, A. Gavrielides, and V. Kovanis, "Chaotic transitions and low-frequency fluctuations in semiconductor lasers with optical feedback," Physica D **145**, 130–143 (2000).
164. I. Fischer, G. H. M. van Tartwijk, A. M. Levine, W. Elsässer, E. Göbel, and D. Lenstra, "Fast pulsing and chaotic itinerancy with a drift in the coherence collapse of semiconductor lasers," Phys. Rev. Lett. **76**, 220–223 (1996).
165. H. Wenzel, U. Bandelow, H.-J. Wunsche, and J. Rehberg, "Mechanisms of fast self pulsations in two-section DFB lasers," IEEE J. Quantum Electron. **32**, 69–78 (1996).
166. M. Mohrle, B. Sartorius, R. Steingruber, and P. Wolfram, "Electrically switchable self-pulsations in integratable multisection DFB-lasers," IEEE Photon. Technol. Lett. **8**, 28–30 (1996).
167. R. Lang and K. Kobayashi, "External optical feedback effects on semiconductor injection laser properties," IEEE J. Quantum Electron. **16**, 347–355 (1980).
168. W. Mohrle, U. Feiste, J. Horer, R. Molt, and B. Sartorius, "Gigahertz self-pulsation in 1.5 μm wavelength multisection DFB lasers," IEEE Photon. Technol. Lett. **4**, 976–978 (1992).
169. J. Sieber, U. Bandelow, and H. Wenzel, "Travelling wave equations for semiconductor laser with gain dispersion," WIAS preprint (1998).
170. U. Bendelow, M. Radziunas, J. Sieber, and M. Wolfrum, "Impact of gain dispersion on the spatio-temporal dynamics of multisection lasers," IEEE J. Quantum Electron. **37**, 183–188 (2001).
171. C. Otto, *Dynamics of Quantum Dot Lasers: Effects of Optical Feedback and External Optical Injection* (Springer, 2014).

172. I. Fischer, Y. Liu, and P. Davis, "Synchronization of chaotic semiconductor laser dynamics on subnanosecond time scales and its potential for chaos communication," Phys. Rev. A **62**, 011801 (2000).
173. A. Argyris, D. Syvridis, L. Larger, V. Annovazzi-Lodi, P. Colet, I. Fischer, J. Garcia-Ojalvo, C. R. Mirasso, L. Pesquera, and K. A. Shore, "Chaos-based communications at high bit rates using commercial fibre-optic links," Nature **438**, 343–346 (2005).
174. D. O'Brien, S. P. Hegarty, G. Huyet, and A. V. Uskov, "Sensitivity of quantum-dot semiconductor lasers to optical feedback," Opt. Lett. **29**, 1072–1074 (2004).
175. R. Al-Seyab, I. D. Henning, M. J. Adams, and A. Hurtado, "Controlled single- and multiple-pulse excitability in VCSELs for novel spiking photonic neurons," in *International Semiconductor Laser Conference (ISLC)* (2014), pp. 165–166.
176. F. Koyama, "Recent advances of VCSEL photonics," J. Lightwave Technol. **24**, 4502–4513 (2006).
177. B. Jalali and S. Fathpour, "Silicon photonics," J. Lightwave Technol. **24**, 4600–4615 (2006).
178. L. Zhuang, C. G. H. Roeloffzen, M. Hoekman, K.-J. Boller, and A. J. Lowery, "Programmable photonic signal processor chip for radiofrequency applications," Optica **2**, 854–859 (2015).
179. T. Durhuus, B. Mikkelsen, C. Joergensen, S. Danielsen, and K. Stubkjaer, "All-optical wavelength conversion by semiconductor optical amplifiers," J. Lightwave Technol. **14**, 942–954 (1996).
180. J. T. Hill, A. H. Safavi-Naeini, J. Chan, and O. Painter, "Coherent optical wavelength conversion via cavity optomechanics," Nat. Commun. **3**, 1196 (2012).
181. A. N. Tait, T. F. de Lima, M. A. Nahmias, B. J. Shastri, and P. R. Prucnal, "Continuous calibration of microring weights for analog optical networks," IEEE Photon. Technol. Lett. **28**, 887–890 (2016).
182. A. N. Tait, T. Ferreira de Lima, M. A. Nahmias, B. J. Shastri, and P. R. Prucnal, "Multi-channel control for microring weight banks," Opt. Express **24**, 8895–8906 (2016).
183. A. N. Tait, A. Wu, T. Ferreira de Lima, E. Zhou, M. A. Nahmias, B. J. Shastri, and P. Prucnal, "Microring weight banks," IEEE J. Sel. Top. Quantum Electron. (to be published).
184. K. Likharev, A. Mayr, I. Muckra, and Ö. Türel, "Crossnets: high-performance neuromorphic architectures for CMOL circuits," Ann. N.Y. Acad. Sci. **1006**, 146–163 (2003).
185. M. A. Nahmias, A. N. Tait, L. Tolias, M. P. Chang, T. F. de Lima, B. J. Shastri, and P. R. Prucnal, "An integrated analog o/e/o link for multi-channel laser neurons," Appl. Phys. Lett. **108**, 151106 (2016).
186. K. Hornik, M. Stinchcombe, and H. White, "Multilayer feedforward networks are universal approximators," Neural Netw. **2**, 359–366 (1989).
187. K.-I. Funahashi and Y. Nakamura, "Approximation of dynamical systems by continuous time recurrent neural networks," Neural Netw. **6**, 801–806 (1993).
188. M. Heck, J. Bauters, M. Davenport, J. Doylend, S. Jain, G. Kurczveil, S. Srinivasan, Y. Tang, and J. Bowers, "Hybrid silicon photonic integrated circuit technology," IEEE J. Sel. Top. Quantum Electron. **19**, 6100117 (2013).
189. G. Roelkens, L. Liu, D. Liang, R. Jones, A. Fang, B. Koch, and J. Bowers, "III-V/silicon photonics for on-chip and intra-chip optical interconnects," Laser Photon. Rev. **4**, 751–779 (2010).
190. N. Mathur, "Nanotechnology: beyond the silicon roadmap," Nature **419**, 573–575 (2002).
191. B. Marr, B. Degnan, P. Hasler, and D. Anderson, "Scaling energy per operation via an asynchronous pipeline," IEEE Trans. Very Large Scale Integr. Syst. **21**, 147–151 (2013).

192. M. Smit, J. Van der Tol, and M. Hill, "Moore's law in photonics," Laser Photon. Rev. **6**, 1–13 (2012).
193. D. Liang, G. Roelkens, R. Baets, and J. E. Bowers, "Hybrid integrated platforms for silicon photonics," Materials **3**, 1782–1802 (2010).
194. D. Liang and J. E. Bowers, "Recent progress in lasers on silicon," Nat. Photonics **4**, 511–517 (2010).
195. D. Marpaung, C. Roeloffzen, R. Heideman, A. Leinse, S. Sales, and J. Capmany, "Integrated microwave photonics," Laser Photon. Rev. **7**, 506–538 (2013).
196. H.-W. Chen, A. Fang, J. Peters, Z. Wang, J. Bovington, D. Liang, and J. Bowers, "Integrated microwave photonic filter on a hybrid silicon platform," IEEE Trans. Microwave Theory Tech. **58**, 3213–3219 (2010).
197. Y. Li, T. Wang, and R. A. Linke, "VCSEL-array-based angle-multiplexed optoelectronic crossbar interconnects," Appl. Opt. **35**, 1282–1295 (1996).
198. D. Louderback, G. Pickrell, H. C. Lin, M. A. Fish, J. J. Hindi, and P. Guilfoyle, "VCSELs with monolithic coupling to internal horizontal waveguides using integrated diffraction gratings," Electron. Lett. **40**, 1064–1065 (2004).
199. D. Taillaert, W. Bogaerts, P. Bienstman, T. Krauss, P. van Daele, I. Moerman, S. Verstuyft, K. De Mesel, and R. Baets, "An out-of-plane grating coupler for efficient butt-coupling between compact planar waveguides and single-mode fibers," IEEE J. Sel. Top. Quantum Electron. **38**, 949–955 (2002).
200. N. Lindenmann, G. Balthasar, D. Hillerkuss, R. Schmogrow, M. Jordan, J. Leuthold, W. Freude, and C. Koos, "Photonic wire bonding: a novel concept for chip-scale interconnects," Opt. Express **20**, 17667–17677 (2012).
201. N. Lindenmann, S. Dottermusch, M. L. Goedecke, T. Hoose, M. R. Billah, T. P. Onanuga, A. Hofmann, W. Freude, and C. Koos, "Connecting silicon photonic circuits to multicore fibers by photonic wire bonding," J. Lightwave Technol. **33**, 755–760 (2015).
202. J. Capmany, B. Ortega, and D. Pastor, "A tutorial on microwave photonic filters," J. Lightwave Technol. **24**, 201–229 (2006).

Paul R. Prucnal received the A.B. degree from Bowdoin College (summa cum laude), with Highest Honors in Math and Physics, where he was elected to Phi Beta Kappa. He then received M.S., M.Phil., and Ph.D. degrees from Columbia University, where he was elected to the Sigma Xi honor society.

He was an Assistant and then tenured Associate Professor at Columbia from 1979 until 1988, when he joined Princeton University, Princeton, New Jersey, as a Professor of Electrical Engineering. He has held visiting faculty positions at the University of Tokyo and University of Parma. From 1990 to 1992, he served as the Founding Director of Princeton's Center for Photonics and Optoelectronic Materials, and he is currently the Director of the Center for Network Science and Applications. He is widely recognized as the inventor of the "Terahertz Optical Asymmetric Demultiplexer," an ultrafast all-optical switch, and has done seminal research in the areas of all-optical networks and photonic switching. His pioneering research on optical code division multiple access (CDMA) in the mid-1980s initiated a new research field in which more than 1000 papers have now been published worldwide. With support from the Defense Advanced Research Projects Agency in the 1990s, his group was the first to demonstrate an all-optical 100 Gb/s photonic packet switching node and optical multiprocessor interconnect. His recent work includes the investigation of linear and nonlinear optical signal processing techniques to provide high-speed data

confidentiality in communications networks. He has published over 250 archival journal papers and holds 17 patents.

Prof. Prucnal is an Area Editor of the IEEE Transactions on Communications for optical networks and was Technical Chair and General Chair of the IEEE Topical Meeting on Photonics in Switching in 1997 and 1999, respectively. He is a Fellow of IEEE with reference to his work on optical networks and photonic switching, a Fellow of The Optical Society (OSA), and a recipient of the Rudolf Kingslake Medal from the SPIE, cited for his seminal paper on photonic switching. In 2006, he was awarded the Gold Medal from the Faculty of Physics, Mathematics and Optics from Comenius University in Slovakia, for his contributions to research in photonics. In 2004, 2006, and 2008, he received Princeton Engineering Council Awards for Excellence in Teaching, in 2006 he received the University Graduate Mentoring Award, and in 2009 the Walter Curtis Johnson Prize for Teaching Excellence in Electrical Engineering, as well as the Distinguished Teacher Award from Princeton's School of Engineering and Applied Science. He is editor of the book *Optical Code Division Multiple Access: Fundamentals and Applications*, published by Taylor and Francis in 2006.

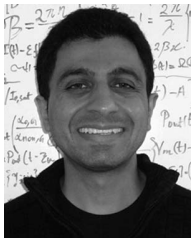

Bhavin J. Shastri received Honours B.Eng. (with distinction), M.Eng., and Ph.D. degrees in electrical engineering from McGill University, Montreal, Quebec, Canada, in 2005, 2007, and 2011, respectively.

He is currently a Banting Postdoctoral Fellow at Princeton University, Princeton, New Jersey. His research interests include dynamical light–matter (beyond-CMOS, beyond-Moore) devices, excitable lasers with low-dimensional materials, reconfigurable photonic network-on-chip, photonic spike processing, computer vision and machine learning, and high-speed RF circuits.

Dr. Shastri has garnered the following research awards: Banting Postdoctoral Fellowship from the Government of Canada through the Natural Sciences and Engineering Research Council of Canada (NSERC), 2012 D. W. Ambridge Prize for the top graduating Ph.D. student, nomination for the 2012 Canadian Governor General's Gold Medal, IEEE Photonics Society 2011 Graduate Student Fellowship, 2011 NSERC Postdoctoral Fellowship, 2011 SPIE Scholarship in Optics and Photonics, a Lorne Trottier Engineering Graduate Fellow, and a 2008 Alexander Graham Bell Canada Graduate Scholarship from NSERC. He was the recipient of the Best Student Paper Awards at the 2010 IEEE Midwest Symposium on Circuits and Systems (MWSCAS), the co-recipient of the Silver Leaf Certificate at the 2008 IEEE Microsystems and Nanoelectronics Conference (MNRC), the 2004 IEEE Computer Society Lance Stafford Larson Outstanding Student Award, and the 2003 IEEE Canada Life Member Award. Dr. Shastri was the President/Co-Founder of the McGill OSA Student Chapter.

Thomas Ferreira de Lima received a bachelor's degree from Ecole Polytechnique, Palaiseau, France. He is currently pursuing the Ingénieur Polytechnicien master's degree from the same school, with a focus on Physics for Optics and Nanosciences. In conjunction with that, he is working toward the Ph.D. degree in Electrical Engineering in the Lightwave Communications Group, Department of Electrical Engineering, Princeton University, Princeton, New Jersey.

His research interests include integrated photonic systems, nonlinear signal processing with photonic devices, spike-timing-based processing, ultrafast cognitive computing, and dynamical light–matter neuro-inspired learning and computing.

Mitchell A. Nahmias received a B. S. (Honors) in Electrical Engineering with a Certificate in Engineering Physics in 2012, and an M.A. in Electrical Engineering 2014, both from Princeton University. He is currently working toward a Ph.D. degree as a member of the Princeton Lightwave Communications Laboratory. He was a research intern at the MIRTHE Center in Princeton, NJ during the summers of 2011–2012 and L-3 Photonics during the summer of 2014 in Carlsbad, CA. His research interests include ultrafast processing, laser excitability, photonic interconnects, photonic integrated circuits, nonlinear optics, and neuromorphic photonics.

Mr. Nahmias is a Student Member of the IEEE Photonics Society and the Optical Society of America (OSA) and has authored or co-authored more than 30 journal or conference papers. He was awarded the John Ogden Bigelow Jr. Prize in Electrical Engineering and was co-winner of the Best Engineering Physics Independent Work Award for his senior thesis. He is also the recipient of the National Science Foundation Graduate Research Fellowship (NSF GRFP), the Best Paper Award at IEEE Photonics Conference 2014 (third place), and the Best Poster award at the 2015 IEEE Photonics Society Summer Topicals Meeting Series (first place).

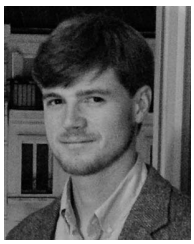

Alexander N. Tait received the B.Sci. Eng. (Honors) in Electrical Engineering in 2012 from Princeton University, Princeton, New Jersey, where he is currently working toward the Ph.D. degree in Electrical Engineering in the Lightwave Communications Group, Department of Electrical Engineering.

He was a research intern for the summers of 2008–2010 at the Laboratory for Laser Energetics, University of Rochester, Rochester, New York, and an undergraduate researcher for the summers of 2011–2012 at the MIRTHE Center, Princeton University, Princeton, New Jersey. His research interests include photonic devices for nonlinear signal processing, integrated systems, neuromorphic engineering, and hybrid analog–digital signal processing and computing.

Mr. Tait is a Student Member of the IEEE Photonics Society and The Optical Society (OSA). He is a recipient of the National Science Foundation Graduate Research Fellowship. He is a co-recipient of the Optical Engineering Award of Excellence from the Department of Electrical Engineering at Princeton. He has authored four papers and a book chapter and co-authored eight journal papers appearing in *Optics Letters*, the *Journal of Applied Physics*, and others.